RAPID PRODUCTION OF POLYMER MICROSTRUCTURES

A Thesis
Presented to
The Academic Faculty

by

Pratapkumar Nagarajan

In Partial Fulfillment
of the Requirements for the Degree
Ph.D. in the
School of POLYMER,TEXTILE & FIBER ENGINEERING

Georgia Institute of Technology
DECEMBER 2008

RAPID PRODUCTION OF POLYMER MICROSTRUCTURES

Approved by:

Dr. Donggang Yao, Advisor
School of School of Polymer,Textile & Fiber Engineering
Georgia Institute of Technology

Dr. Youjiang Wang
School of School of Polymer,Textile & Fiber Engineering
Georgia Institute of Technology

Dr. Wallace W. Carr
School of School of Polymer,Textile & Fiber Engineering
Georgia Institute of Technology

Dr. John D. Muzzy
School of Polymer,Textile & Fiber Engineering
Georgia Institute of Technology

Dr. Karl Jacob
School of School of Polymer,Textile & Fiber Engineering
Georgia Institute of Technology

Date Approved: 6/27/2008

To those who blazed the trail before me, forging my path.
To Sundari, Priya, Mala, and Nagarajan, who joined me on my journey and held the lantern to light the way.

ACKNOWLEDGEMENTS

The author is highly indebted to his advisor, Dr. Donggang Yao, for his guidance, constructive criticism and support throughout this research and for introducing him to polymer microfabrication.

The author would like to especially thank Dr. Wallace W. Carr, Dr. Karl Jacob, Dr. Youjiang Wang and Dr. John D. Muzzy for serving in the dissertation committee and providing valuable comments and advices.

The author wishes to acknowledge Ram K.R.T for his help during theoretical studies and Ruihua Li and Jun Jia for their help during experimental studies.

The author would like to thank Dr. Meisha L. Shofner, Mr. Mihir Oka and Mr. Sudhakar Jagannathan for their help during Dynamic Mechanical Analysis and Mr. Dennis Denney for helping with mold machining.

Dr. Ken Gall and Mr. Matthew Di Prima are acknowledged for their help during hot chamber tensile tests.

Kathryn Abbott, Wei Zhang, Sarang Deodhar, Jasmeet Kaur, Shamal Mhetre, Vibor Jain and Murari Gupta are acknowledged for their help and encouraging discussions during the Ph.D. study.

The author also wishes to thank Ms. Angie Abbott, Ms. Hope Holly, Ms. Linda Roberson, Mr. Michael Boyett and Mr. Joseph Brooks for their administrative assistance during the Ph.D. study.

Mr. James Gallman is particularly acknowledged for his continuous help with software installation and network support throughout the study.

The author would like to especially thank his parents, Mala Nagarajan and Nagarajan Venkatesan, for providing the foundation for the success which he has had in the past or he will have in the future. The author also deeply thank other family members

and friends, in particular, Sundaralakshmi Gunasekaran, Visswapriya Prabakar, Chitra Rajasekaran, Rajasekaran Palaniandi ,Akila Rajasekaran ,Deepali Palta and Wanting Ren for their tolerance, trust, support and dedication over these years.

Last but not the least, the author is grateful to National Science Foundation and Delphi Research Labs for financial support of this research.

TABLE OF CONTENTS

LIST OF TABLES

LIST OF FIGURES

LIST OF SYMBOLS

T_1	Embossing temperature
T_0	Ambient temperature
p_0	Embossing pressure
t_0	Zero embossing Time
t_1	End of embossing time
t_2	Mold opening time
M (t-t')	Memory function
t	Processing time
t'	Dwell time
S_{DE}	Doi-Edwards strain tensor
$\underline{\underline{C}}^{-1}{}_t(t)$	Finger strain tensor
$\underline{\underline{C}}^{-1}{}_t(t')$	Cauchy strain tensor
$Ø_1, Ø_2$	Damping function
I_1, I_2, I_3	Invariants
η	Viscosity
η^*	Complex viscosity
$\dot{\gamma}$	Shear rate
P	Pressure
ρ	Density
α	Thermal diffusivity
$\underline{\underline{\tau}}$	Stress tensor
k	Thermal conductivity
h	Interfacial thermal conductance

t	Thickness
$\tilde{T}$	Normalized temperature
$\tilde{t}$	Normalized thickness
$\tilde{h}$	Normalized interfacial thermal conductance
m, n, h	Node indices
i	Step index
c_p	Specific heat
v	Velocity
f_n	Normal stress
f_s	Tangential stress
C_1 & C_2	WLF constants
λ	Stretch ratio
C_{ij}	Cauchy-Green strain tensor
S_{ij}	Piola-Kirchhoff stress tensor
W	Strain energy function
E_{ij}	Lagrangian strain tensor

LIST OF ABBREVIATIONS

Tg	Glass transition temperature
Tm	Melting temperature
IR	Infrared
UV	Ultraviolet
HDPE	High density polyethylene
PS	Polystyrene
PC	Polycarbonate
ABS	Acrylonitrile butadiene styrene copolymer
PCL	Polycaprolactone
PVC	Polyvinyl chloride
MPa	Mega Pascal
KPa	Kilo Pascal
MHz	Mega Hertz
KHz	Kilo Hertz
PET	Polyethylene terephthalate
Fig	Figure
nm	Nanometer
PP	Polypropylene
s	Second
C	Centigrade
min	Minute
mm	Millimeter
COC	Cyclo olefin copolymer

SUMMARY

The goal of this research is to develop an integrated polymer embossing module, with which difficult-to-emboss polymer microstructures and microparts can be fabricated in a cost-effective manner. In particular, the research addresses three major limitations of the hot embossing process, namely, long cycle time, difficulty in producing shell patterns, and difficulty in building up a high embossing pressure on thick substrates. To overcome these limitations, three new technical approaches – two-station embossing, rubber-assisted embossing, and through-thickness embossing – were developed and investigated. Fundamental understanding of these new embossing techniques were achieved through extensive experimental and theoretical studies involving parametric experiments, rheological characterization, surface investigation, mathematical modeling, and computer simulation.

A two-station embossing process was developed to reduce the hot embossing cycle time, accomplished by decoupling the heating and cooling stations. For this purpose, the standard hot embossing mold was replaced by a shell type mold, and separate hot and cold stations were used to selectively heat and cool the shell mold during the process. With this method, microlens arrays and micro channels were fabricated onto ABS and HDPE substrates with a cycle time of approximately 10 s. Numerical simulations were performed to study the effect of different design parameters, including thermal contact resistance, shell material and shell thickness, on the thermal response at the mold surface. Furthermore, the polymer flow during the two-station embossing process for the microlens was numerically studied. The simulated filling behavior agreed

with the experimental observation, and the predicted thermal and deformation history of the polymer offers a good explanation on the experimentally observed process characteristics.

The second technique, rubber-assisted embossing, involving a rubber pad as a soft counter tool, was developed for precision embossing of shell structures. The rubber pad acted as a temporary negative during embossing and recovered to its original geometry after mold opening. With rubber-assisted embossing, a micro shell pattern with a characteristic size of 50 μm was successfully patterned on 25-μm thick polystyrene films. A focused study was undertaken on rubber-assisted isothermal embossing to establish the relationship between process parameters and pattern replication. It was found that the pattern replication and film uniformity were affected by the embossing temperature and the hardness of rubber. It was also found that adequate plasticity and higher stiffness of the deforming film were essential in achieving excellent pattern replication and uniformity in film thickness.

The through-thickness embossing process was developed for embossing pressure buildup and fabrication of 3-D parts. The embossing tool includes a punching head and to-be- replicated features in the socket behind the punching head. The built-in punching head facilitates a through-thickness action and provides a close-die environment for embossing pressure buildup. The method was used to emboss multichannel millimeter waveguides which requires crispy edges and accurate dimensions. With a tool temperature of 140°C, an embossing time of 3 min and a total cycle time of 7 min, discrete 4-channel waveguides were successfully embossed from a room-temperature ABS substrate. A computer model was established to study the flow behavior during

through-thickness embossing. It was found that nonisothermal embossing conditions helped to confine the polymer in the cavity and reduce the outflow into the surrounding region, thus achieving complete fill of the cavity.

CHAPTER 1

INTRODUCTION

Microfabrication deals with manufacture of miniature devices and systems in the micrometer or even nanometer regimes. The microfabrication technology, originally developed for the microelectronic industry, has later been adapted to the biomedical, telecommunication and automotive industries. Although silicon and glass are widely used in microfabrication, polymeric materials with its versatile properties and mass production capabilities are replacing these conventional materials in numerous miniature applications. Particularly, with polymers, opposite material properties, e.g., insulative versus conductive, hydrophilic versus hydrophobic, and opaque versus transparent, may be easily achieved with appropriate design and selection of polymers. Recent developments in dopable semiconductive polymers, piezoelectric polymers, and other functional polymers, not only allow polymers to be used as a substitute for silicon in electronics, sensors and actuators, but also open up new applications that cannot be realized before.

In the past two decades, much research has been done worldwide on adaptation of standard polymer processing techniques into microfabrication, resulting in a new subset of technology in polymer processing: polymer microfabrication [1-5]. Polymer microfabrication techniques can be classified into two distinct groups [6]: direct techniques, where each device is manufactured separately, and replication techniques, where a large number of parts are produced by replicating a single master. While the direct methods such as lithography, laser ablation and micro milling have mainly been used for prototyping purposes, the replicating techniques such as injection molding and hot embossing have been successfully employed for mass production of polymeric

microstructures and devices. These replication techniques are often referred to as micromolding processes [5].

Among all micromolding processes, hot embossing has emerged as one of the most promising processes for mass production. It has several advantages over other techniques such as injection molding and soft molding/casting. The advantages include but are not limited to:

- *Simple tool design*. Hot embossing allows a simple setup of the plant, which is advantageous if tool or plant reconstruction or modifications are necessary.
- *Lower residual stresses*. The flow length of the polymer is relatively short compared with that in injection molding, and hence hot embossing is well-suited for precision and optical parts.
- *Cost-effectiveness in production*. The process is particularly economical for small or medium scale production.

1.1 Hot Embossing Process

The standard hot embossing process is designed for imprinting surface features onto polymer substrates [4-5]. The process involves several sequential stages: a mold preheating stage, an embossing stage, a cooling stage and a mold opening stage, as illustrated in Fig.1.

1.1.1 Mold Preheating Stage

The mold is preheated above the softening temperature of the polymer. In case of an amorphous polymer, it would be above the polymer's glass transition temperature (Tg) and for a semicrystalline polymer, it would be close to the polymer's melting temperature (Tm). Failure to preheat the mold often results in premature freezing of the polymer inside the mold cavity during the embossing stage. In this stage, the most important process parameter is the heating temperature.

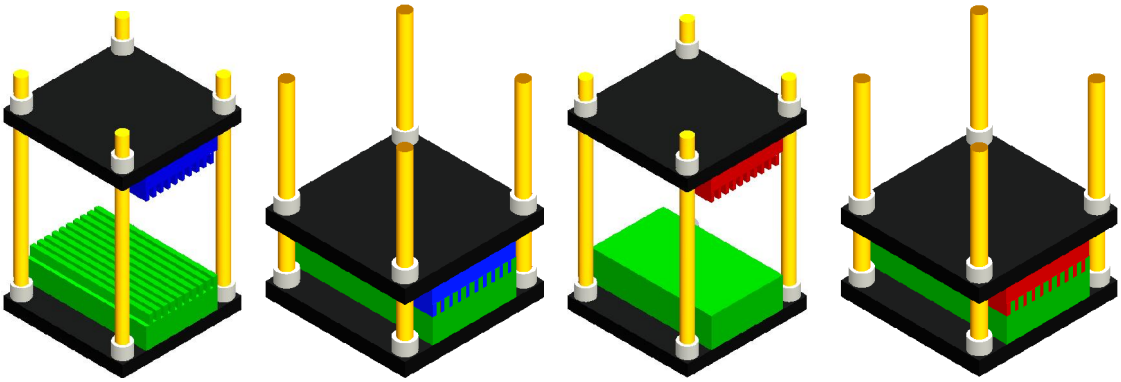

a) b) c) d)

Figure 1: Hot embossing process: a) mold preheating, b) embossing, c) cooling, and d) mold opening.

1.1.2 Embossing Stage

During the embossing stage, pressure is transferred from the mold to the polymer substrate. A constant embossing pressure p_0 is applied over a period of time, from t_0 to t_1, as shown in Fig.2. The polymer deforms and fills up the mold cavity. The polymer above the polymer softening temperature undergoes a significant amount of creep flow during embossing. Insufficient embossing time could result in incomplete fill of the mold.

1.1.3 Cooling Stage and Mold Opening Stage

The embossing stage is followed by the cooling stage. The constant pressure p_0 is maintained to compensate for any shrinkage during the cooling process. The polymer is allowed to cool to a temperature significantly below its Tg or Tm. The time associated with the cooling stage is the cooling time t_2–t_1. Insufficient cooling time results in distortion of the embossed part during ejection. At the end of the cooling stage, the mold is opened and the part is ejected out of the mold.

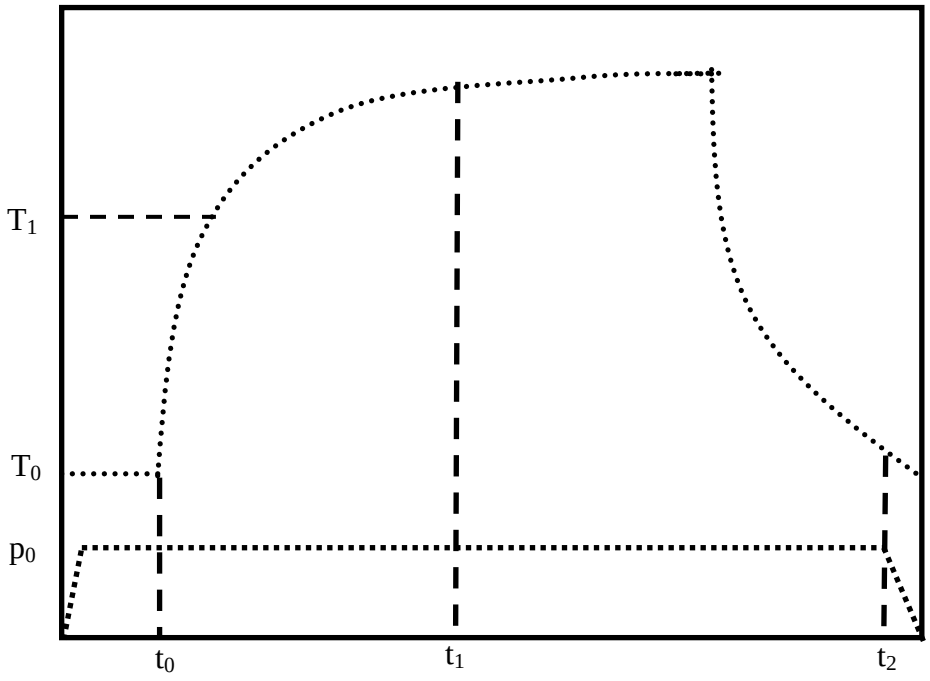

Figure 2: Pressure-Temperature Response of hot embossing process. T_0 and T_1 are the ambient temperature and the polymer softening temperature, respectively. p_0 is the constant embossing pressure.t_0 and t_1 signify the beginning and end of the embossing stage, respectively. At time t_2, the cooling stage ends and the mold opens.

1.2 Limitations of Hot Embossing

The major limitations of the hot embossing process include: long cycle time, inadequate pressure buildup and difficulty in patterning shell geometries.

1.2.1 Long Cycle Time

The total cycle time involved in hot embossing is the summation of the embossing time and the cooling time. During hot embossing, the mold and the polymer are preheated to a temperature above the polymer softening temperature. Since the mold undergoes a preheating stage and a cooling stage during the entire cycle, thermal cycling of the mold is needed during hot embossing. Typically, an embossing tool consists of a stamp and a mounting plate on its back or a bulk plate with microcavities or microstructures on one side. The relatively large thermal mass of this embossing tool results in a low rate of thermal cycling and consequently a long cycle time on the order of several minutes or

longer. The long dwell time at elevated temperatures could further cause polymer degradation, especially for thermally sensitive polymers such as thermoplastic polyesters. The problem exacerbates when thick polymer substrates are embossed. To address this problem, rapid thermal cycling of the embossing tool is needed. To reduce the cycle time, mold rapid heating techniques, often referred to as variothermal mold heating, such as ultrasonic heating, IR heating and gas heating, have been introduced to hot embossing and microinjection molding processes. These methods, however, require significant modifications and complex designs of the molding tool for achieving a low thermal mass. Hence, a more efficient and simpler approach for thermal cycling of the mold is highly desired.

1.2.3 Difficulty in Patterning Shell Geometries

Microstructures on a polymer film/substrate may be classified into surface and shell microstructures, based on the relative size of the microstructure. For surface microstructures, the characteristic size of the microstructure is much smaller than the film thickness. During patterning, surface microstructures undergo localized deformation at the film surface, and as the feature size increases, significant change in the film thickness may occur. In contrast, shell microstructures experience deformation over dimension larger than the film thickness, and the patterned film is marked by shell-type geometry with little change in the film thickness during the patterning process [3-4]. Examples of surface and shell microstructures are shown in Fig.3. Micro-patterned films designed for electrostatic sensors and actuators and capillary electrophoresis systems involve shell geometry, while microchannels and microlens arrays for microfluidics and optical devices involve surface patterns. Mature processes do not exist for precision fabrication of shell patterns on thermoplastic films. Thermoplastic structuring of shell patterns on continuous films using a roller embossing process has been available industrially for several decades for fabrication of products in various applications, such as diapers,

packaging and raincoats [7-10]. This process, however, is designed towards the improvement of the surface appearance and property of the product rather than the accuracy of the patterned structures. Efforts have been made to scale down conventional polymer forming techniques such as thermoforming and modify micromolding techniques such as hot embossing for precision structuring of polymeric film [5,7,11]. However, the present techniques are complicated and often results in poor fidelity of the patterned geometry.

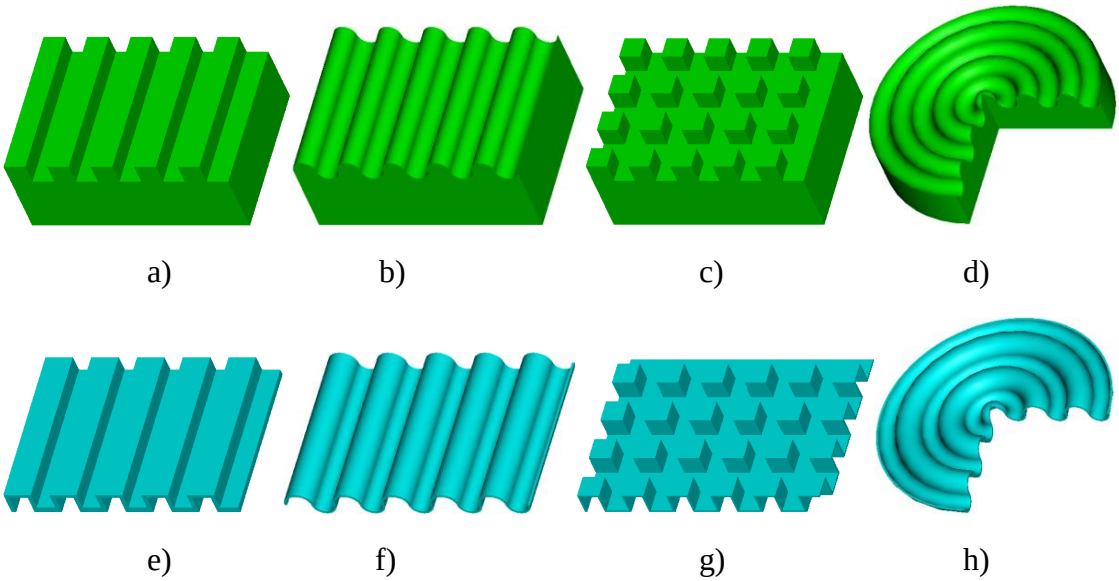

Figure 3: Examples of surface and shell microstructures: a), b), c) and d) are surface microstructures, and e), f), g), and h) are shell microstructures.

1.2.4 Inadequate Pressure Buildup

The hot embossing process has been successfully used for the fabrication of low aspect ratio surface microstructures. However, processing difficulties are present when high aspect ratio microstructures, particularly on thick substrates, are embossed. Significant lateral polymer squeeze-out flow occurs in hot embossing due to the open-die nature of the process, as shown in Fig.4b. This is generally considered to be acceptable in replication of low aspect ratio surface features. It, however, may result in incomplete

replication when a high embossing pressure is needed (e.g., when high aspect ratio features are embossed). Furthermore, due to the open-die nature, separable or discrete features, e.g., microgears, waveguides, micro thorough holes, among others, are difficult to fabricate. If one defines surface features as 2.5-D features, these above-mentioned discrete features/parts are indeed more three-dimensional. To emboss these precision 3-D features, an appropriate through-thickness action is needed.

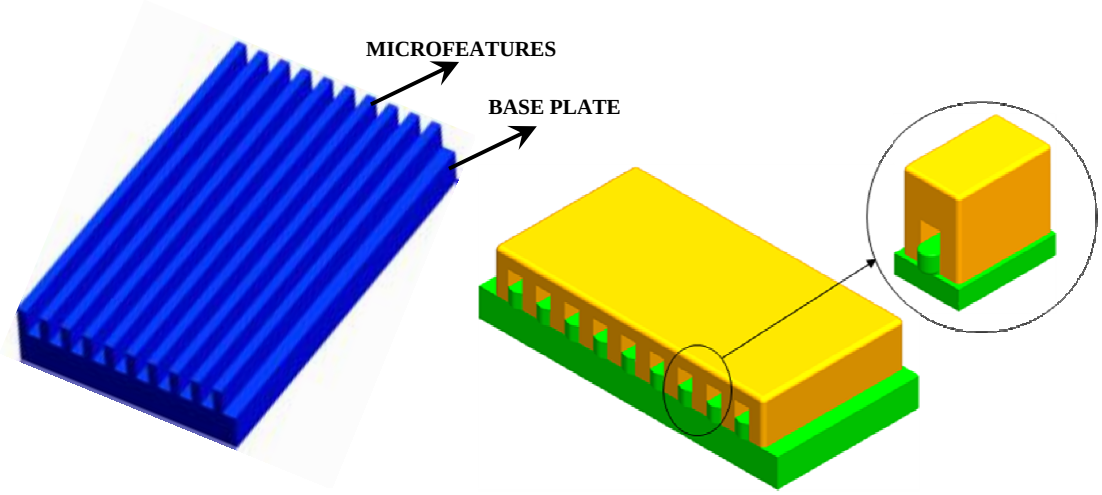

a) b)

Figure 4: a) Hot-embossing mold and b) open-mold design resulting in lateral squeeze-out flow.

1.3 Research Objectives and Approaches

The primary research objective is to develop new processes addressing the current limitations of the hot embossing process, particularly, long cycle times, difficulty in replicating shell-type patterns and inadequate pressure buildup. The emphasis is placed on developing processes that are simplistic in design but highly cost-effective in production. Another objective is to establish a fundamental understanding of these new processes through extensive experimental and theoretical studies.

To reduce the cycle time, a two-station embossing process was developed, by decoupling the heating and cooling processes during embossing through the use of shell-type molds. Two separate heating and cooling stations are used to reduce the large thermal mass associated with the mold. Experimental studies showed that aluminum stamps with a thickness of 1.4 mm can be rapidly heated from room temperature to 200°C in 3 s using contact heating against a hot station at 250°C. Microchannels and microlenses were successfully embossed onto high-density polyethylene substrates and acrylonitrile-butadiene-styrene copolymer substrates, respectively, using a heating time less than 3 s and a total cycle time around 10 s. The two-station embossing process for the microlens was also numerically studied. The simulated filling behavior agreed with the experimental observation and the predicted thermal and deformation history of the polymer offered a good explanation on the experimentally observed process characteristics.

A rubber-assisted embossing approach was developed to pattern shell geometries. The rubber acts as a soft counter tool during embossing. The use of the rubber pad eliminates the alignment and ejection issues encountered in standard hot embossing. A series of experiments were carried out to understand the parameters affecting the patterned geometry. The rubber-assisted embossing process was modeled using a hyperelastic material model and the effects of processing parameters on the pattern replication were numerically studied. The results from the numerical simulation were in reasonable agreement with the experimental observation and provided improved understanding on the effects of the major processing parameters on the pattern replicability and uniformity.

A through-thickness embossing process was developed to overcome the difficulty in pressure buildup. A mold design incorporating a punching/cutting head was designed and fabricated. The use of the puncher/cutter facilitated high pressure buildup during embossing of 3-D geometries. Experimental parametric studies were conducted to

understand the effects of processing parameters on the embossed quality. A computer model was formulated to simulate the flow behavior during the embossing process.

The focus of this research was placed not only on the development of these new processes but also on achieving a fundamental understanding of these processes through detailed experimentation, rheological studies, surface characterization, mathematical modeling and computer simulation.

CHAPTER 2

LITERATURE REVIEW

As discussed in Chapter 1, hot embossing is subjected to some serious process drawbacks, greatly limiting its capabilities. Specifically, the major limitations include considerably long cycle time due to slow thermal cycling of the mold, inadequate pressure buildup caused by an open mold design, and difficulty in embossing shell or film patterns. In this chapter, we undertake a detailed literature review on some process enhancements suggested by previous researchers. In the later half of the chapter, we also review the mathematical models for hot embossing.

2.1 Literature Review on Rapid Thermal Cycling of Molds

During the last decade, efforts have been made in developing/adapting rapid thermal cycling techniques for hot embossing applications. Various heating techniques using fluid medium, infrared (IR) and ultrasound have been employed to rapidly heat the mold [12-23].

Chang et al. [12-13] developed a fluid-based thermal cycling system for rapid mold heating and cooling during hot embossing. High-temperature steam, hot oil and IR radiation were used for mold rapid heating. Water was used as a cooling medium. Fig.5 shows the setup using steam heating. A nickel stamp was used as an embossing master, and the substrate used was a polyvinyl chloride (PVC) film of a 0.2 mm thickness. Heated steam with a pressure of 500 KPa was blown into the chamber to heat the substrate-mold stack directly. After steam heating, highly pressurized nitrogen gas at 3000 KPa was blown into the chamber to emboss the substrate. After the gas-pressurized embossing, cooling water was circulated inside the bottom plate to cool the substrate and mold. Chang et al. achieved a cycle time of 2 min using this steam heating and water

cooling process. Fig.6 shows the typical thermal response of the mold during steam heating. Although they were able to achieve a significant reduction in cycle time, the use of steam as a heating medium limits the control of the embossing temperature and pressure. Moreover, polymer membrane covering the back of the mold may be permeable to gasses at high temperature, resulting in a pressure drop during the embossing process.

In another work, Chang et al. [14] used oil as the heating and embossing medium to rapidly heat the mold, as shown in Fig.7. Water was used as the cooling medium and was circulated beneath the mold and also inside the chamber. During the mold heating stage, the silicone oil at 150°C was circulated inside the chamber and simultaneously pressurized to emboss the polymeric substrate. At the end of the embossing stage, the cooling water was circulated to cool the mold. Fig.8a shows the thermal response of the mold due to oil heating. The mold was heated from 30°C to 130°C in 3.5 min. Fig.8b shows the embossed PVC substrate using this fluid-based hot embossing system. Chang et al. also used IR radiation for rapid mold heating. Fig.9 shows the experimental setup. IR radiation was directly used to preheat the mold and the polymer prior to embossing. Nitrogen at 3000 KPa was used to pressurize the mold against the polymer substrate. With IR heating, the mold was heated from 30°C to 130°C in 25 s. Water was used as a cooling medium. Chang et al. achieved a total cycle time of 2 min using combined IR heating and water cooling. Fig.10 shows the thermal response of their mold.

Lee et al. [15] also used radiation heating for rapid thermal cycling during hot embossing of polymethyl methacrylate (PMMA) optical lenses. The resulting reduction in cycle time was limited to low embossing temperatures. Optical parts require lower birefringence and hence a higher embossing temperature, resulting in a longer cycle time.

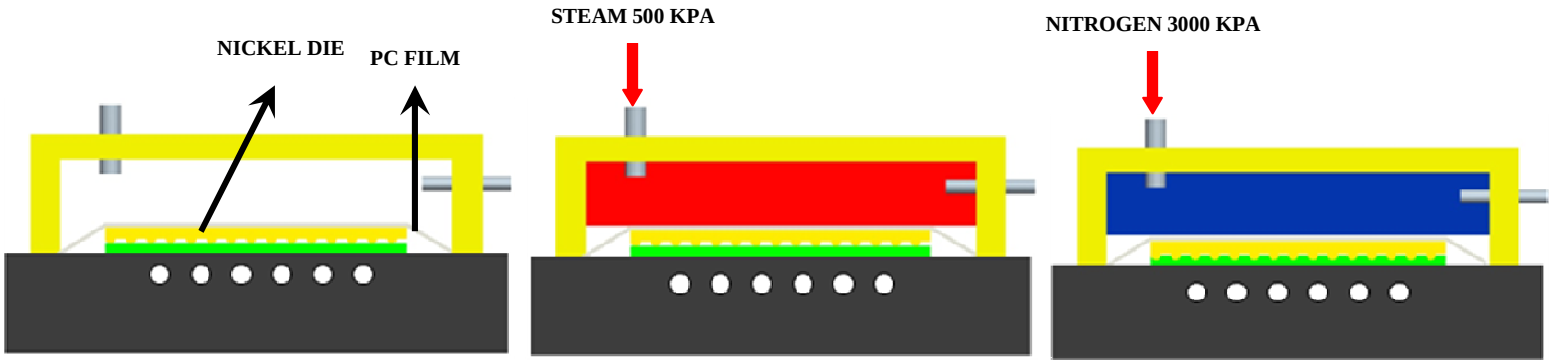

Figure 5: Mold design for rapid thermal cycling using steam heating and water cooling.

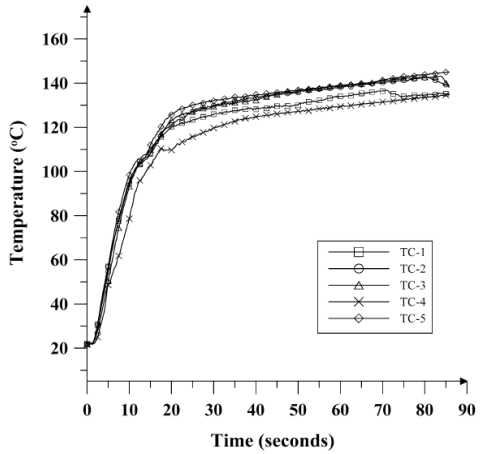

(b)

Figure 6: Heating response of a nickel die using steam heating [12].

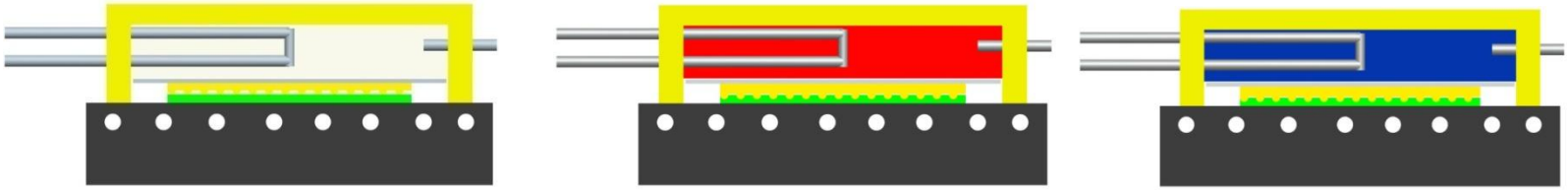

Figure 7: Mold design for rapid thermal cycling using oil heating and water cooling.

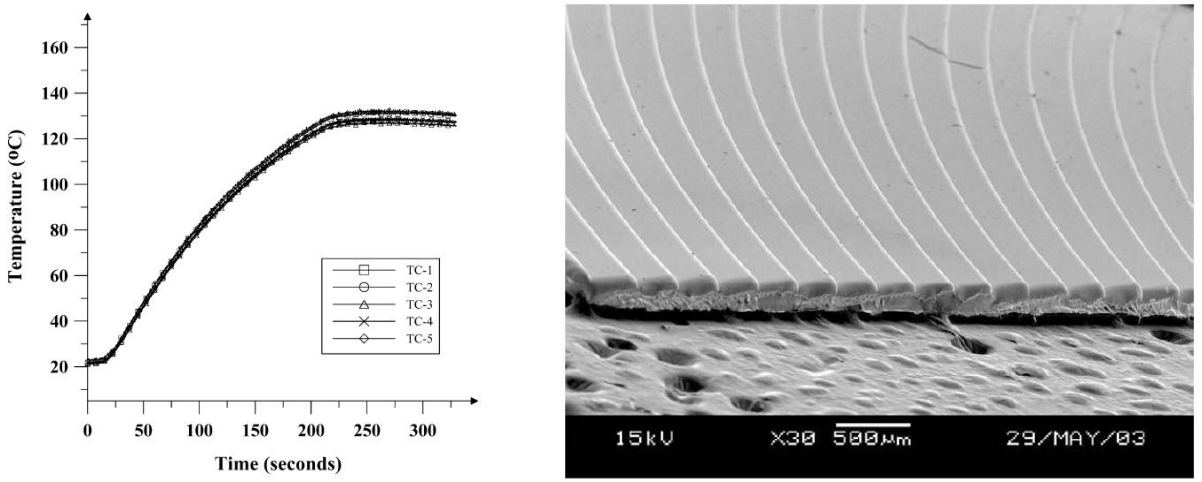

a) b)

Figure 8: Mold rapid heating with hot oil: a) heating response and b) embossed PVC substrate [13].

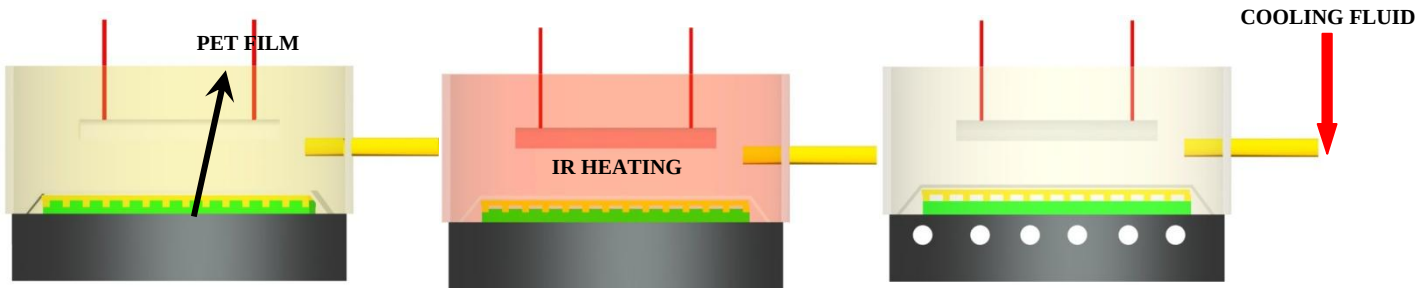

Figure 9: Mold design for rapid thermal cycling using IR heating.

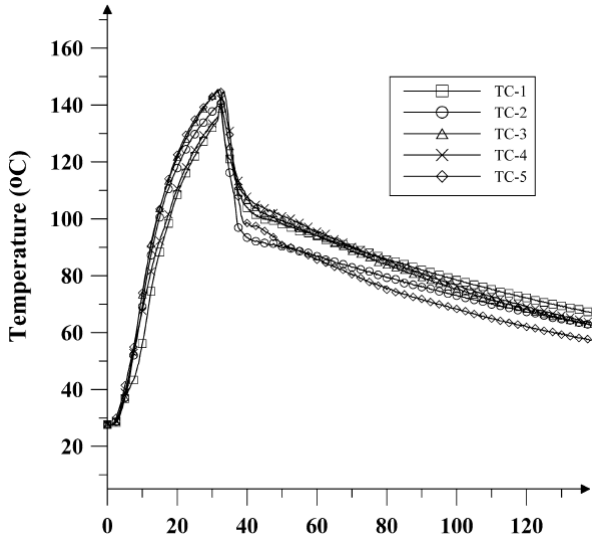

Figure 10: Mold surface temperature response with IR heating and gas cooling [13].

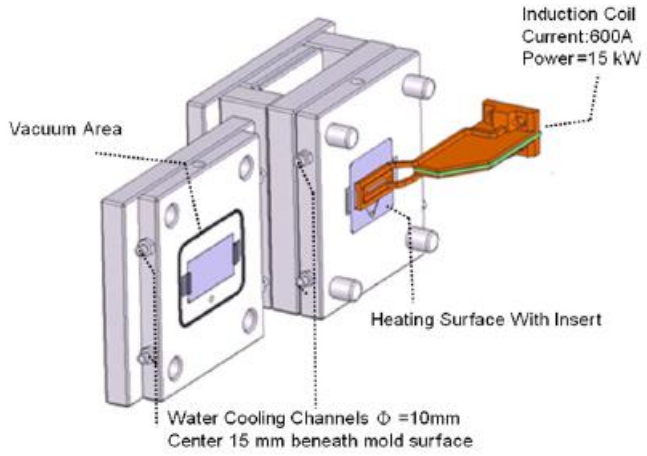

a)

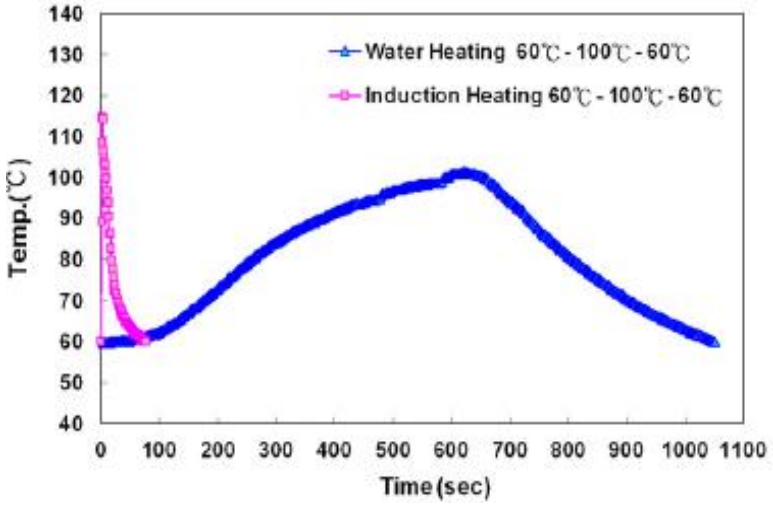

b)

Figure 11: Mold rapid thermal cycling using induction heating: a) heating setup and b) heating and cooling response [16-18].

Chen et al. [16-18] investigated an induction heating technique in micro-injection molding. Their experimental setup for inductive mold heating is shown in Fig.11a. The surface of the mold insert was machined with microfeatures. With induction heating, the mold was heated from 60°C to about 140°C in 2 to 3.5 s. After the mold preheating, PMMA was injected into the cavity, and the mold was cooled to 60°C in almost 110 s. They were able to achieve a total cycle time of approximately 114 s (Fig.11b.).

Mold rapid heating by infrared radiation heating using halogen lamps was explored by Seunarine et al. [19]. Fig.12 shows the experimental setup. Polycaprolactone (PCL) and Topas® cyclic olefin copolymer (COC) films were placed over a nickel stamp. The nickel stamp with nanometer scale features was heated by the halogen lamps placed on the top of the stamp. A thermocouple embedded inside the polymer was used to monitor the temperature during heating and cooling. Both PCL and COC films were heated from 30°C to 100°C in 45 s, as shown in Fig.13a. As the nickel master reached the polymer softening temperature, the top plate was lowered, and the pattern transfer was completed. At the end of the embossing stage, the polymer material was cooled to room temperature through conduction. The embossed PCL and COC cooled to room temperature in 30 s and 60 s, respectively (Fig.13b). Fig.13c shows the embossed surface on PC. Using the optical heating method, they were able to achieve a total cycle time of 105 s.

Yao et al. [20,21] developed a high-frequency resistive heating technique for mold rapid thermal cycling, as shown in Fig.14. The mold insert surface was electrically heated using high-frequency current at a frequency between 500 kHz and 1 MHz. In high-frequency heating, the heat generation is localized at the mold surface because of the skin effect. The typical surface thermal response of the insert is shown in Fig.15a. The insert was thermally cycled between 70°C and 200°C in about 5 s. An Instron universal testing machine was retrofitted for the embossing purpose .The Instron machine provided control on either the depth of the microfeatures or the pressure applied to the

polymer substrate. A vacuum fixture was used to secure the polymer blank during the embossing and demolding stages. The mold insert was mounted to the end of the compression load cell using a mechanical fixture. Compressed air was used as coolant during the mold cooling stage. Various polymer microstructures such as hexagonal wells, moth eye and micro holes were embossed onto polymeric substrates, as shown in Fig.15b.Using the high-frequency resistive heating technique, they were able to achieve a cycle time of 20 s for embossing of these structures.

A room-temperature embossing approach was developed to achieve a reduction in cycle time [22], as shown in Fig.16. In this approach both the polymer and the mold were at room temperature. An Instron universal testing machine was retrofitted for the experiment. Microfeature of 100 × 500 μm, as shown in Fig.17, was embossed onto PTFE substrates with a cycle time of 180 s. The authors also noted that the embossed structure underwent viscoelastic recovery over a period of time and could not maintain the fidelity of the original geometry (Fig.18).

Chien et al. [23] used an ultransound assisted embossing process for fabricating grooves and pillars with varying width from 400 nm to 2 μm and with a depth of 300 nm onto thermoplastic polymers. Ultrasonic vibrations concentrated through a horn and transmitted through the mold resulted in localized melting of the polymer near the mold. Fig.19a shows the experimental setup that was used for the process. The polymer was initially spin-coated over a substrate with a thickness equivalent to that of the height of the required micro/nano structure. The spin-coated polymer was cured at 150°C over a period of 3 min. The silicon mold was placed over the surface of the polymer, and the lamination was placed under an ultrasonic horn on a pneumatic press. This was followed by the application of ultrasonic vibrations through the horn. The intermolecular friction between the polymer and the mold raised the temperature above Tg and caused localized flows.

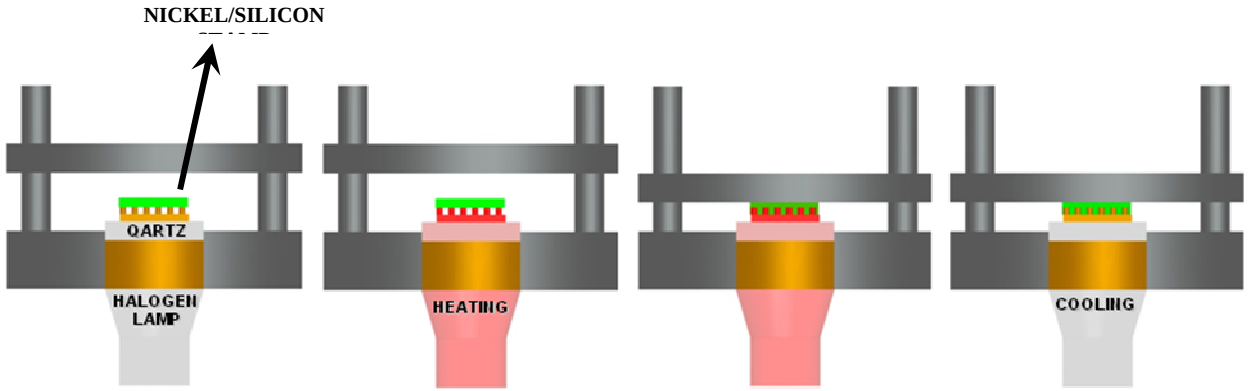

Figure 12: Mold rapid heating using halogen lamps.

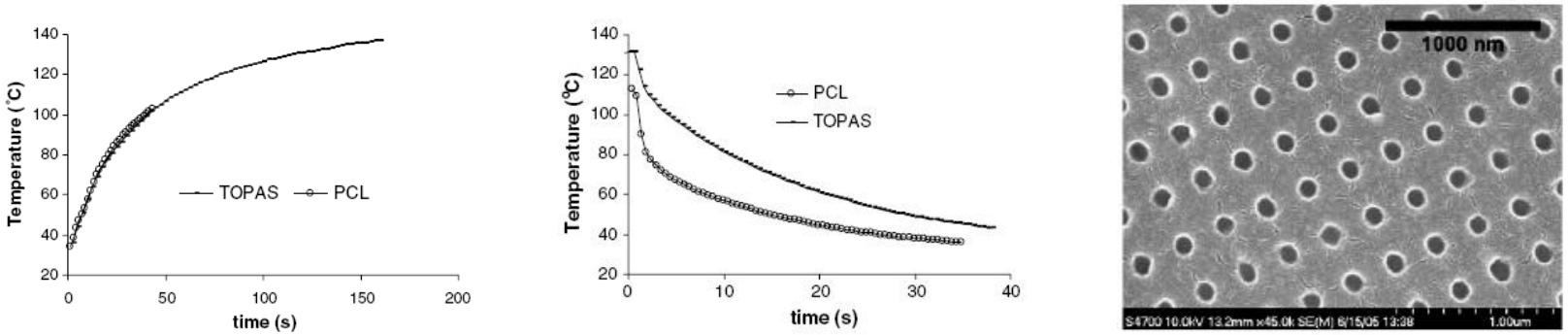

a) b) c)

Figure 13: Infrared heating of a nickel die: a) heating response, b) cooling response and c) embossed PCL substrate [19].

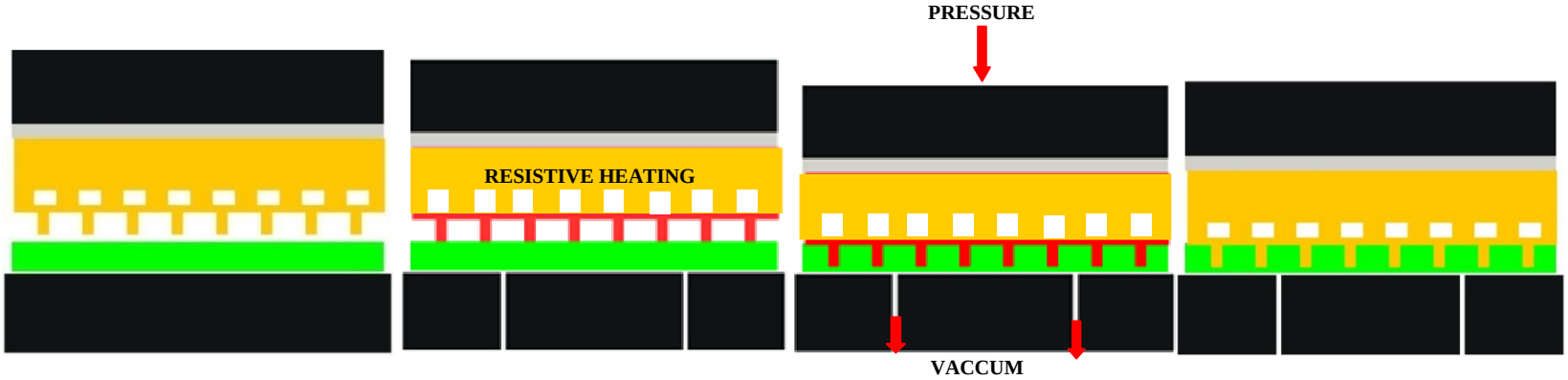

Figure 14: Mold rapid thermal cycling through resistive heating.

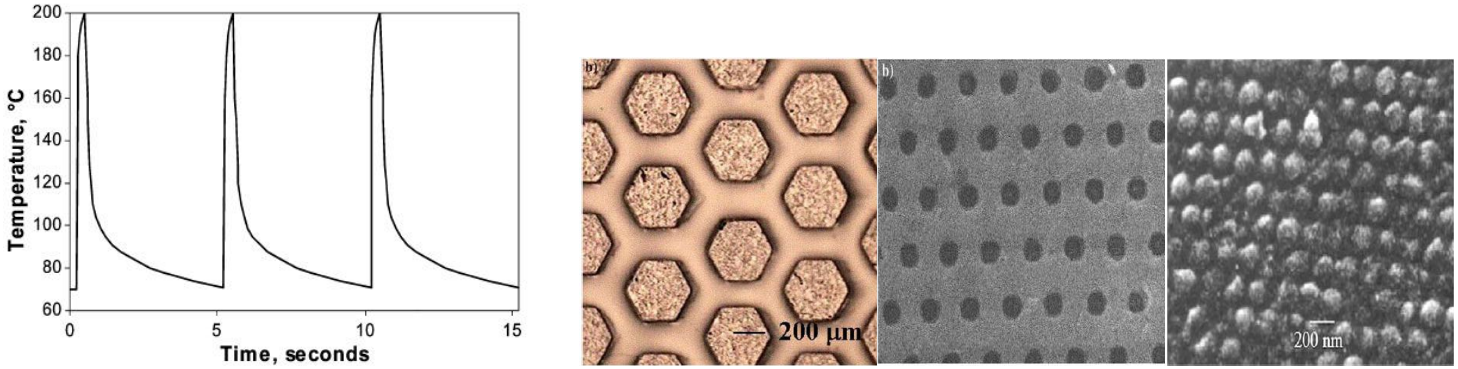

a) b)

Figure 15: a) Heating response of the mold and b) fabricated microstructures on PMMA and high-density polyethylene (HDPE) [20-21].

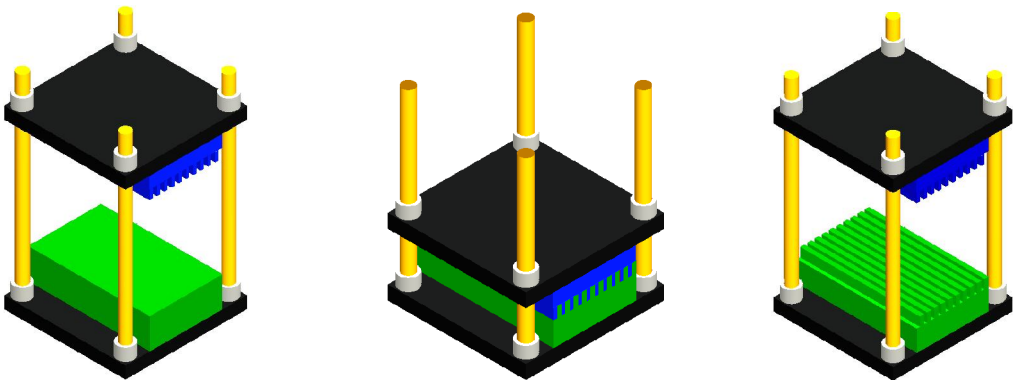

a) b) c)

Figure 16: Room-temperature embossing: a) start-up, b) embossing and holding, and c) mold opening.

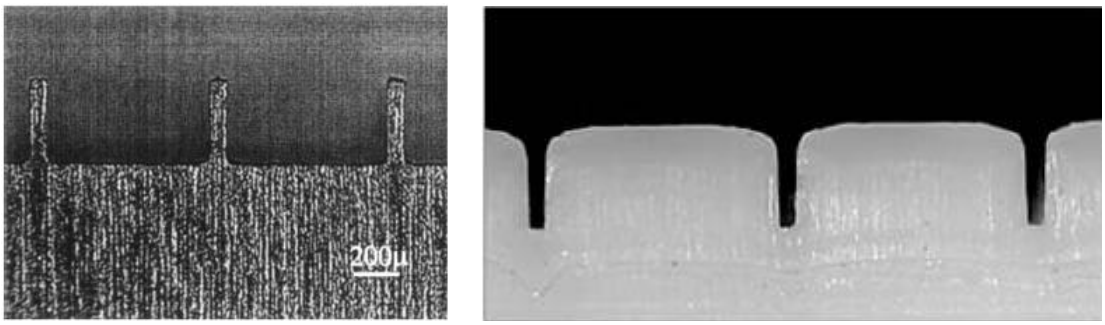

Figure 17: Embossing die and embossed microfeatures on Teflon [22].

The ultrasonic vibrations were applied over a period of 3 s. The polymer was cooled down to room temperature in a few seconds. However, the authors were unable to achieve complete fill of the mold cavity using this method (Fig.19b).This was attributed to the requirement for further process optimization. Ultrasonic heating was also investigated by Grewell et al. [24]. They used polystyrene (PS) and HDPE as the substrate materials. On PS, the pattern transfer was achieved with a cycle time of 10 s but the pattern transfer on the HDPE samples showed poor replicability. The authors also commented that better results could be obtained with thinner samples.

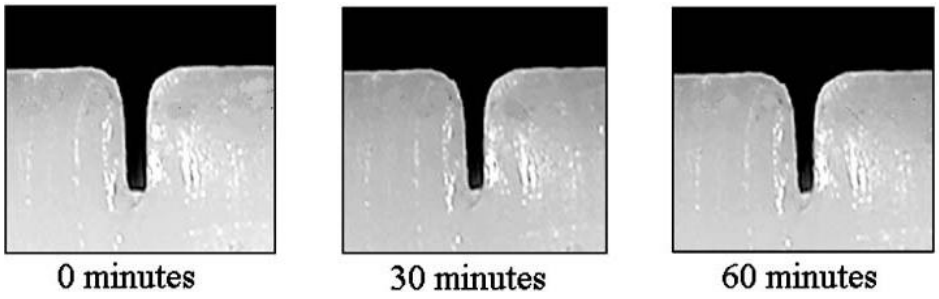

Figure 18: Viscoelastic recovery of a room-temperature embossed groove.

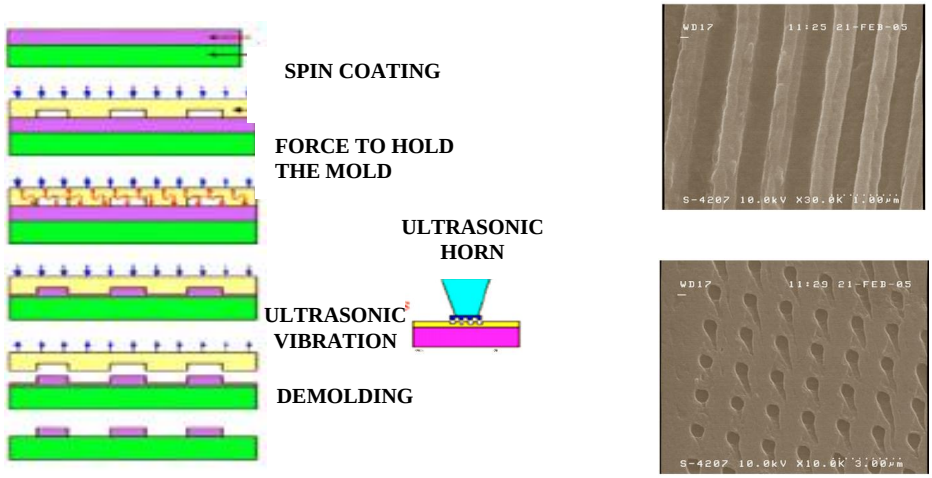

Figure 19: Mold rapid heating by ultrasonic heating: a) process sequence and b) embossed microstructure on HDPE [23].

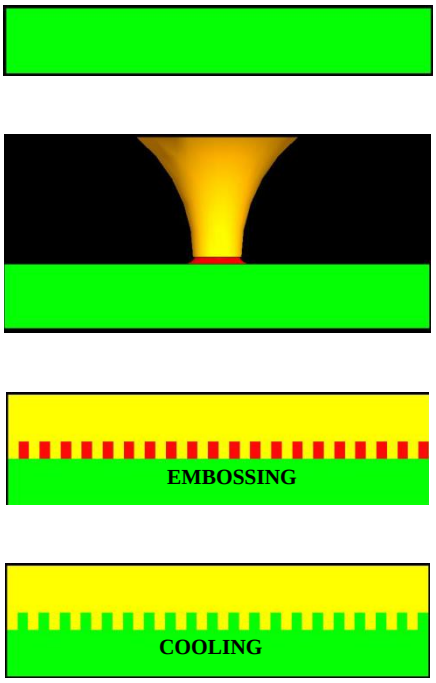

Figure 20: Hot gas-assisted embossing [25].

A hot gas-assisted embossing approach using hot air for mold heating was also investigated in the literature [25]. This process is illustrated in Fig.20. The mold was maintained at room temperature, and the polymer was heated close to its melting temperature using a hot air gun at 250°C. An embossing tool was then forced against the molten HDPE, and a dwell time of 3 s was applied. The embossed polymer was cooled close to room temperature before demolding. The replicated edges were found to be rounded; this was due to the low hydrostatic pressure, resulting in incomplete filling of the tool.

2.2 Literature Review on Patterning Shell Type Geometries

Thermoplastic structuring of shell patterns on continuous films using a roller embossing process has been available industrially for several decades for fabrication of products in various applications, such as diapers, packaging and raincoats [7,26-29]. The roll embossing process, however, is designed towards improvement of the surface

appearance and property of the product rather than the accuracy of the patterned structures. Mature processes do not exist for precision fabrication of shell patterns on thermoplastic films. Efforts have been made to scale down conventional polymer forming techniques such as thermoforming and modify micromolding techniques such as hot embossing for precision structuring of polymeric films [7,11,28].

Tryckenmuller et al. [11,29] used a microthermoforming process to pattern 25 μm thick PS film with 125 μm deep and 250 μm wide microchannels. The thermoforming setup consisted of a mold, a polymer film and a counter plate. A PS film was placed over the substrate with holes for pressurizing the film during embossing. The entire setup was placed over a countertop with channels for evacuating and pressuring the chamber. The mold was placed between two seals, as shown in Fig.21. The chamber was evacuated, forcing the hot mold against the polymeric film. Compressed nitrogen was forced into the channels, deforming the film against the mold cavities. After embossing, the mold was cooled to room temperature. Although this method was successfully employed to thermoform microfluidic analysis chips, as shown in Fig. 22, complete replication and uniform film thickness were difficult to reach due to the increased permeability of the polymer film to gasses at high temperatures. In this process, film heating is achieved through heat conduction between the polymer film and the hot mold. As the polymer film is pressed against the mold, the portion of the polymer film below the mold cavity cannot be heated resulting in a non-uniform temperature across the embossing film. This restricts the use of the microthermoforming process for patterning high aspect ratio structures [29]. Another disadvantage is the difficulty in achieving a uniform film thickness after patterning, as shown in Fig.22.

Dreuth et al. [7] adapted the roller embossing approach to fabricate 50 μm thick patterns on 10 μm thick polyethylene terephthalate (PET) film. Fig.23 shows their experimental setup. The to-be-embossed structures were directly micromachined onto the rolls. The width of the structures on the rolls was about 1 cm. The speed and the

temperature of the rolls were controlled by a computer program. The pressure exerted during the embossing process was determined by the weight of the embossing rolls. Two levels of embossing temperatures were used: 110°C and 170°C. The roll speed was maintained at either 0.77mm/s or 39mm/s. The polymer film between the embossing rolls deformed and assumed the shape of the roll molds. The embossed film was air cooled. The disadvantage of this process is that the patterned polymer film emerging from the roll is above the polymer's soften temperature, resulting in unwanted feature recovery and thus poor fidelity of the patterned geometry, as shown in Fig.24. Moreover, it is extremely difficult to fabricate a pair of rolls with mated microstructures and to synchronize their speed during the embossing process. The authors also reported damage to the embossing structures on the roll due to misalignment and friction.

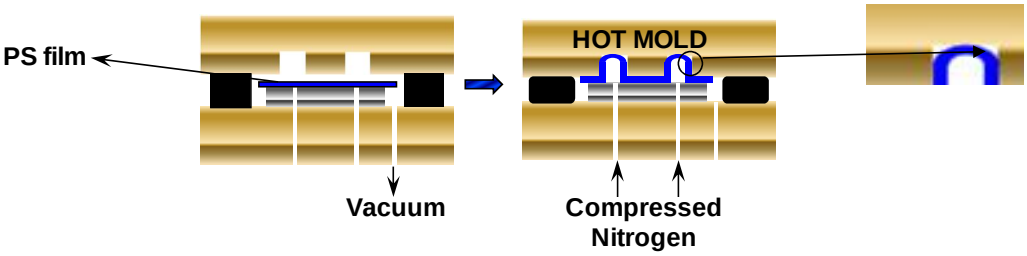

Figure 21: Microthermoforming process.

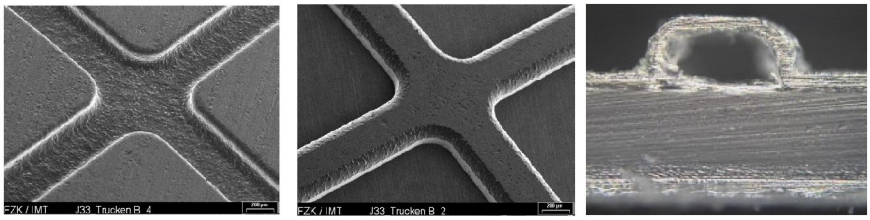

Figure 22: Microthermoformed PS film [29].

In another effort [7], the above authors used hard counter tools to structure PET films (Fig.25). Two stainless-steel positive and negative pieces were machined with

mating microfeatures. The similar sequence of operation as in hot embossing was followed for feature transfer. The positive and the negative masters were preheated above the Tg of the polymer. During the embossing stage, a 1.5µm thick PET film was pressurized between the mating dies. At the end of the embossing stage, the polymeric film was cooled to room temperature. Although shell-type geometries can be patterned using this technique, machining of mating tools at a small scale is difficult and expensive. Another difficulty is in aligning the pair of tools during embossing and ejection. The authors noted that the misalignment of the counter tools often resulted in the tearing of the film during the embossing process. Shell-type patterns were also replicated by the use of hard and deformable counter tools. In this case, one hard tool is replaced by a deformable counter tool with deformation properties similar to that of the embossed polymer, as shown in Fig.26. The polymer film and the deformable counter tool soften and take the shape of the die during the embossing process. The primary difficulty with this thermoplastically deformable counter tool is in matching the necessary properties between this soft tool and the embossing film. In particular, the deformable tool undergoes permanent deformation during embossing and may cause ejection issues.

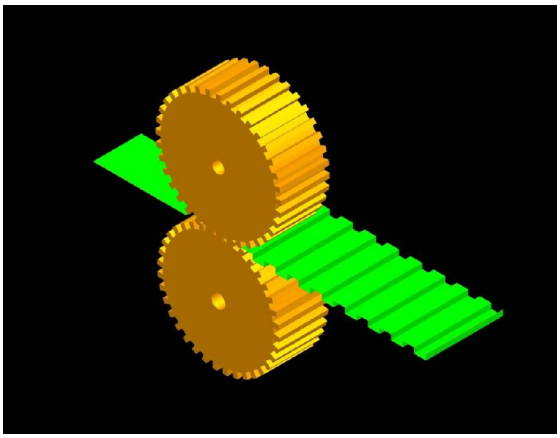

Figure 23: Roll embossing of thin polymer film.

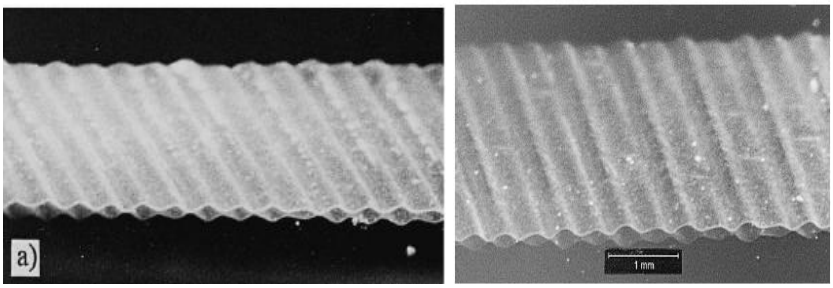

Figure 24: Roll embossed PET film [7].

Dumond et al. [25], investigated the use of lithography and embossing techniques for fabricating nanoscale shell-type geometries (Fig.27). Two silicon grating molds were selected, one with 500 nm pitch, 250 nm linewidth and 250 nm depth to define the nanochannels, and other with 1 μm pitch, 500 nm linewidth and 500 nm depth to define the channel enclosure and isolate the individual nanochannels. The mold was machined using lithographic techniques. PMMA with a weight average molecular weight (Mw) of 1.2×10^5 and T_g of 105°C was spin coated onto the 250 nm linewidth and 250 nm depth mold. The spin-coated PMMA was cured at 80°C for 3 min to remove the solvent. The 500 nm linewidth mold was aligned over the cured PMMA and embossed at 150°C and 5 MPa over a period of 5 min. The mold was cooled to room temperature at the end of embossing. Fig.28 shows completely replicated structures by this method. Nevertheless, this lithography and spin coating based method is expensive and slow and thus difficult to scale up for mass production.

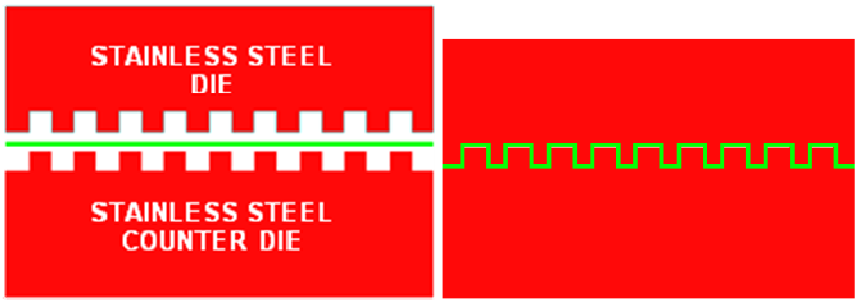

Figure 25: Shell fabrication using a pair of hard counter tools.

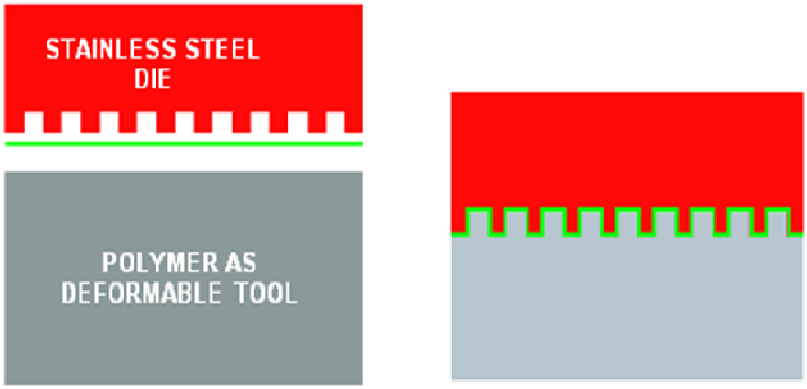

Figure 26: Shell fabrication using a deformable counter tool.

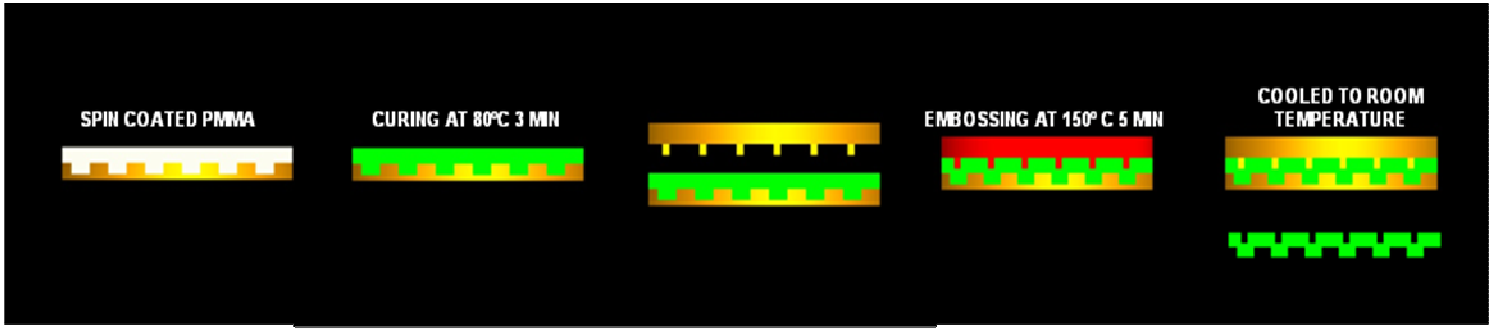

Figure 27: Shell pattern fabrication using lithography and embossing techniques.

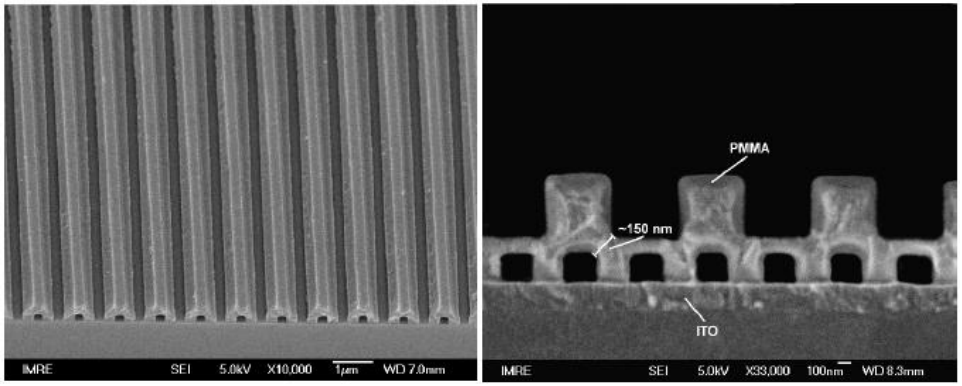

Figure 28: Embossed shell type patterns on PMMA [25].

2.3 Literature Review on Replication of High Aspect Ratio 3-D Features

Limited work has been carried out in the past in hot embossing of 3-D discrete features and parts. Most work on replication of 3-D discrete features was performed with injection molding machines. However, the use of injection molding has several limitations including higher residual stresses and higher tooling cost.

Heckele and Durand [26] developed a technique for producing through-holes by hot embossing. They used a substrate with two layers of different materials. After embossing, the tool features protruded through the upper layer into the lower layer. After removal of the lower layer, through holes were left on the upper layer. Verner [27] described a process involving identical top and bottom mold halves, both containing pins, whose top surfaces are attached to each other upon mold closure. The authors used a COC sheet as a hole punching substrate (Fig.29). The COC sheet was placed between the embossing masters with mold inserts of various diameters. The punching tool helped with pressure buildup during the embossing process. The authors successfully embossed through holes on the COC sheet, but they noted the presence of burs on the entrance of the embossed hole. The authors also tested two other embossing tools as shown in Fig.30. The COC sheet was placed between the two embossing masters and embossed. With joint punching actions on both sides of the COC sheet, burs were removed from the hole entrance. However, with this approach, a thin residual layer is present in the middle of the hole. Similar ideas may be developed for hot-embossing discrete 3-D parts out of polymer sheets.

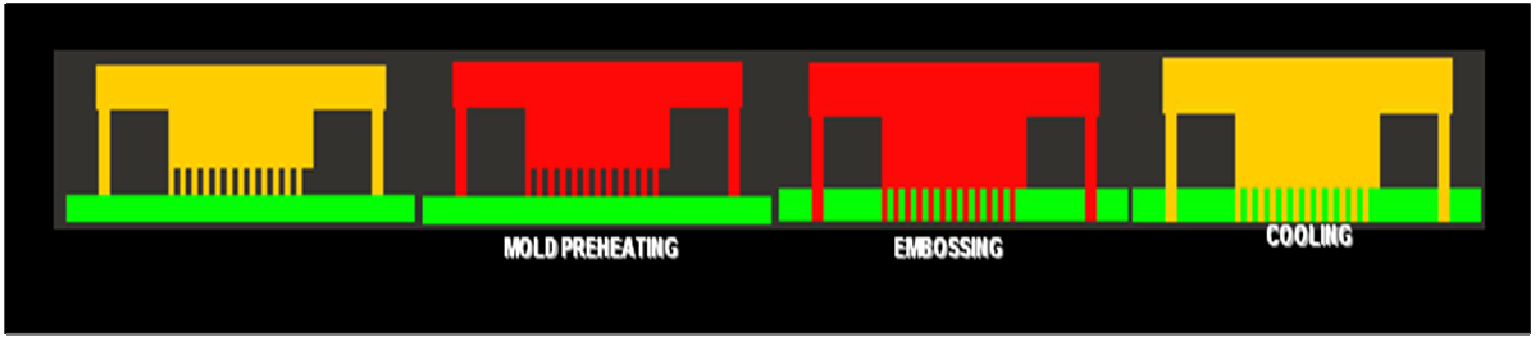

a)

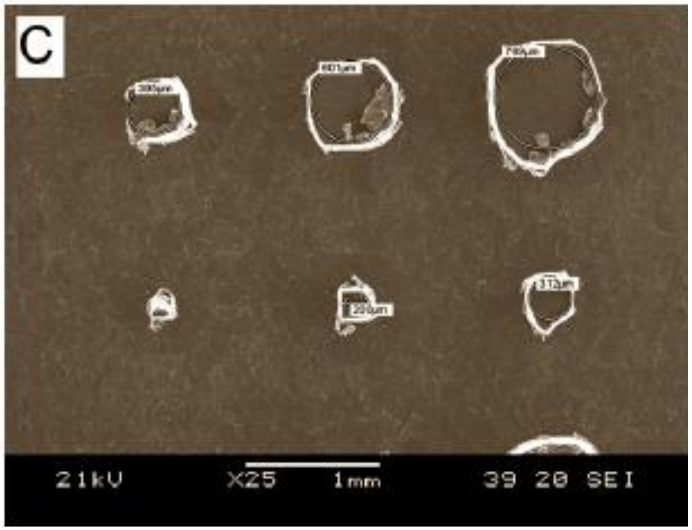

b)

Figure 29: One-sided through-hole embossing: a) experimental sequence and b) embossed through holes with burs [27].

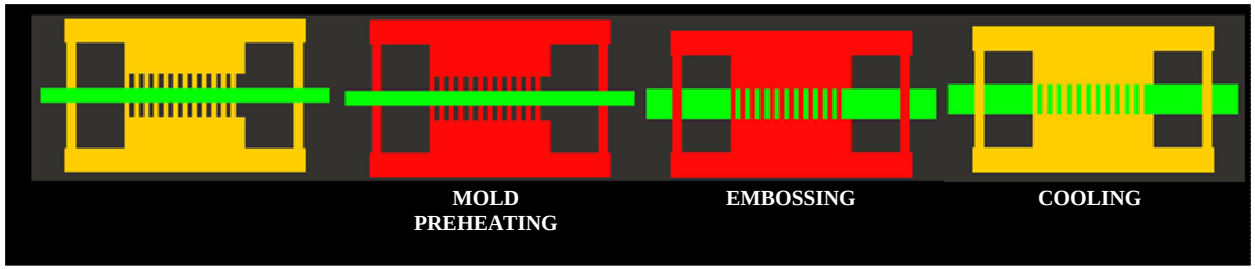

a)

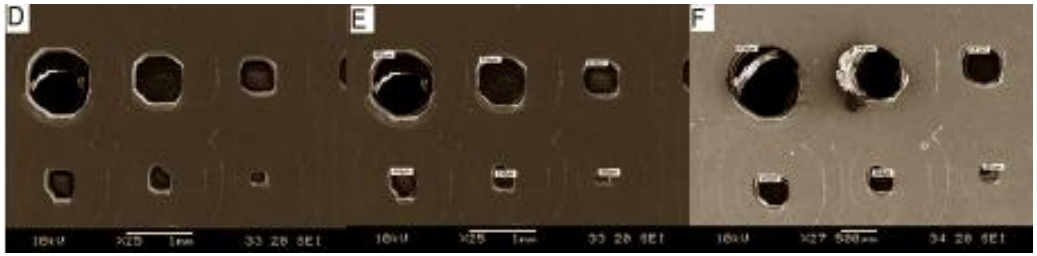

b)

Figure 30: Two-sided hole punching process: a) experimental sequence and b) embossed holes on a COC sheet [27].

2.4 Review on Modeling of Polymer Flow during Embossing

Considerable effort has been made in the past to understand the effect of temperature, pressure and geometry on the flow behavior during hot embossing. Hot embossing is essentially a thermoplastic molding process, involving similar operation sequences as in compression molding. However, the deformation temperature of the polymer during hot embossing is typically lower, close to the polymer softening temperature. The flow behavior exhibited by the polymer at this molding temperature may be substantially different from those in other higher-temperature processes, such as injection molding and extrusion [30]. The isothermal and non-isothermal flow behavior of polymer films during the hot embossing process has been widely studied in the past. Juang et al. [30] used DEFORM®, a commercial finite element code, to understand the polymer flow behavior during isothermal and non-isothermal embossing processes. For the isothermal embossing process, a dynamic shear viscosity fitted into a power-law model was used and, for the non-isothermal flow model, the calculated dynamic shear viscosity at various temperatures above Tg was used. The flow behavior exhibited by the polymer during the isothermal embossing process resembled an extensional flow (Fig.31), while the nonisothermal flow showed an upward movement along the walls (Fig.32). Young [31] studied the polymer flow behavior and numerically computed the pressure distribution during imprinting of various positive embossing geometries. A two-dimensional isothermal viscous flow model was used to study the flow behavior. Under a constant temperature of 180°C and an imprinting speed of 200 nm/s the polymer exhibited an elongational flow behavior (Fig.33). Before the polymer touched the tool base, the induced high pressure area was found to be under the imprinting tool. As the polymer touched the base of the tool, most of the polymer was under compression and the pressure rised drastically (Fig.33). The flow patterns during embossing were found to be affected by the distance between the positive patterns and also by the number of patterns.

The increase in the number of patterns on the die and decrease in the pattern distance caused a marked increase in the filling pressure (Fig.34 and 35). This phenomenon was attributed to the increase in flow resistance inside the channels. The flow resistance is directly proportional to the polymer flow distance and inversely proportional to the cubic power of the channel height. Eriksson et al. [32] used a molecular stress function constitutive model to study polymer flow during replication of surface microstructures. The general form of the constitutive model was written as

$$\tau = \frac{5}{4\pi} \int_{-\alpha}^{t} M(t - t') \, f(x, t, t')^2 \, S_{DE}(x, t, t') dt' \qquad (1)$$

where M(t-t') is the linear memory function, f(x,t,t') denotes the molecular stress function and $S_{DE}(x,t,t')$ represents the strain tensor from the Doi-Edwards model. The numerical modeling of the flow was performed on two length scales, at a macroscale describing the steady planar flow (relative to the flow front) between two parallel mold plates and at a microscale describing the time-dependent flow into the structure. The information from the macroscale was passed to the microscale as an applied local boundary condition. The finite element simulation results showed quantitative agreement with the experimental results with small experimental scattering for a wide range of experimental conditions (Fig.36).

Yao et al. [33] used a non-isothermal viscoplastic model to study the flow behavior exhibited by polymers during embossing process. The flow stress was modeled to be a function of strain, strain rate and temperature, The numerical and experimental results revealed that the size of the cavity has a major effect on the heat diffusion process and consequently on the filling process during nonisothermal embossing. For large cavities, the heat diffusion process is not as fast as the embossing process. As a result, only the polymer in the vicinity of the contact becomes significantly heated and localized squeezing flow occurs. As the cavity is isomorphically downsized, the relative speed of the heat diffusion process becomes higher and higher, finally leading to a uniform

temperature distribution of the polymer substrate and a uniform flow field, as shown in Fig.37.

The film deformation during rubber-assisted embossing process is similar to that of thermoforming and blow molding process. Considerable amount of work has been carried out to model thermoforming and blow molding of polymer sheets. Among the models available in literature, hyperelastic constitutive laws with a memory function have been mainly used for simulating these processes. Lee et al. [34] investigated the influence of rheological parameters and processing parameters on thickness distribution during a vacuum snap forming process using a Wagner model. The Wagner model is a K-BKZ type single integral nonlinear constitutive model, with parameters obtained by data fitting of shear and elongational data. The K-BKZ type single integral model has the following general form:

$$\underline{\underline{T}} = -p\underline{\underline{I}} + \underline{\underline{\tau}}$$

$$\underline{\underline{\tau}} = \int_{-\alpha}^{t} \sum_{i=1}^{N} \frac{\eta_i}{\lambda_i^{\,2}} \exp\left(\frac{-(t-t')}{\lambda_i}\right) \left[\varphi_1(I_1, I_2)\, \underline{\underline{C}}^{-1}{}_t(t) + \varphi_2(I_1, I_2)\, \underline{\underline{C}}_t(t')\right] dt' \qquad (2)$$

where $\underline{\underline{C}}^{-1}{}_t(t')$ and $\underline{\underline{C}}_t(t')$ are the finger strain tensor and Cauchy strain tensor. The damping functions $\varphi_1(I_1, I_2)$ and $\varphi_2(I_1, I_2)$ in the Wagner model are defined as follows:

$$\varphi_1 = \exp\left(-\beta\left[\alpha I_1 + (1-\alpha) I_2 - 3\right]^{0.5}\right), \varphi_2 = 0 \qquad (3)$$

The authors reported that there was a considerable fitting error (11% error) between the experimental and simulation results. Several other researchers [35-39] have also reported large differences between experimental and simulated thickness distribution. Erchiqui et al. [38] used a different constitutive model, based on membrane theory and Lagrangian formulation, to simulate thermoforming of an ABS (acrylonitrile butadiene styrene copolymer) thin sheet under the action of gas flow. The influences of hyperelastic models (Ogden and Mooney-Rivlin) and viscoelastic models (Lodge and Christensen) on thickness and stress distribution in the formed part were analyzed. McEvoy et. al [39]

developed a creep constitutive model for blow molding and simulated PET blow molding using both solid and shell elements. Nam et al. [40] used three-dimensional solid elements and membrane (shell) elements to model free inflation, vacuum forming and plug assisted forming. Constitutive laws based on the hyperelastic Mooney-Rivlin model were used, and the influence of non-isothermal temperature distribution was investigated. A similar model, based on an explicit time integration scheme, was proposed by Marckmann et al. in [41]. The influence of temperature in the thermoforming process was numerically investigated also by Song et al. [43], who developed an FEM (finite element method) code combining a rigid viscoplastic equation for forming computation, Arrhenius and Williams equations for viscosity computation, and a Galerkin FEM equation for computing the temperature field. Schmidt et al. [44] proposed an axysimmetric numerical simulation scheme based on a volumic approach, using an Update-Lagrangian finite element formulation and an automatic remeshing technique. Industrial case studies were carried out by Wiesche [45] and by Gao et al. [46].

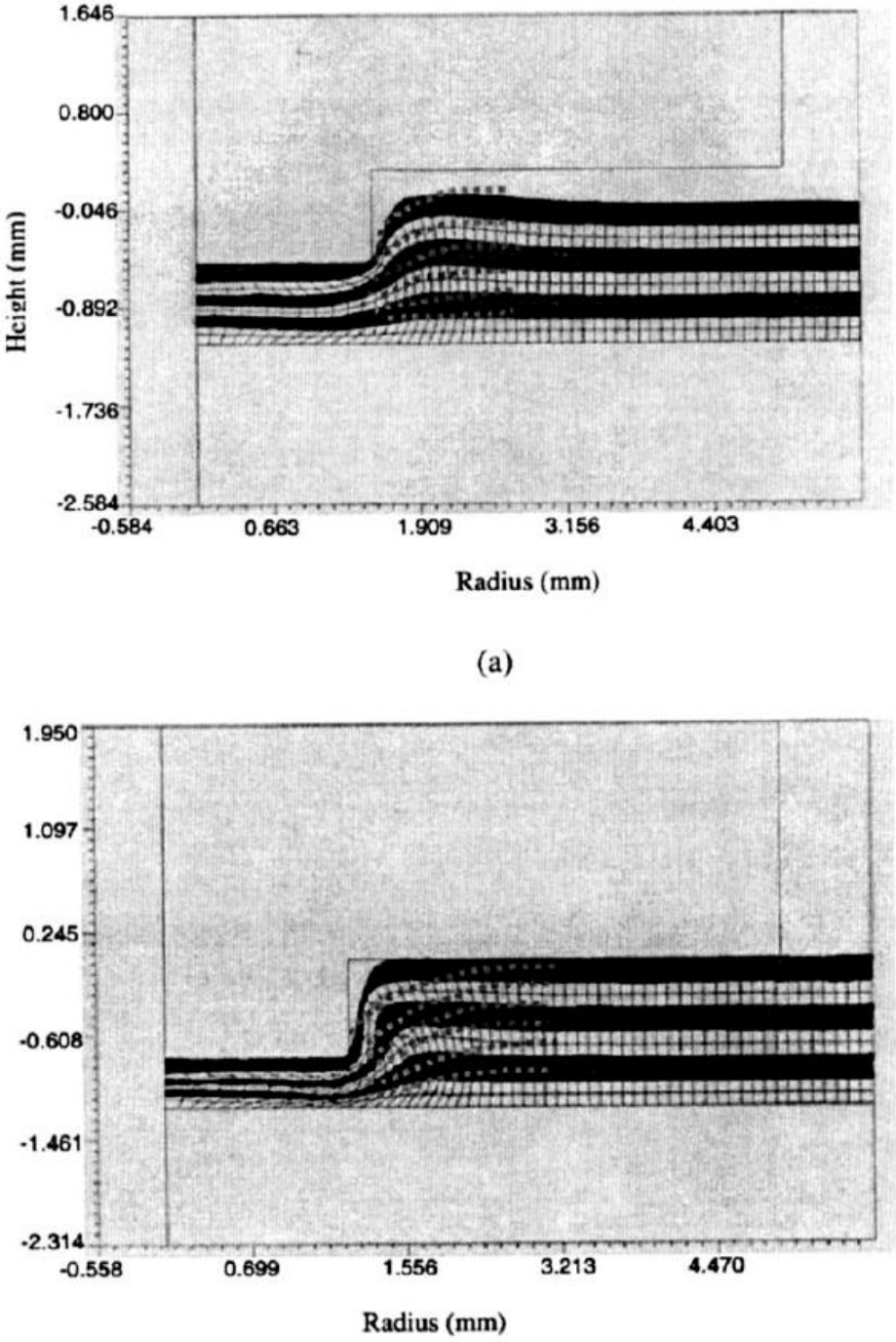

Figure 31: Simulation results of flow pattern at a) 300 µm and b) l500 µm embossing depth under isothermal embossing [30].

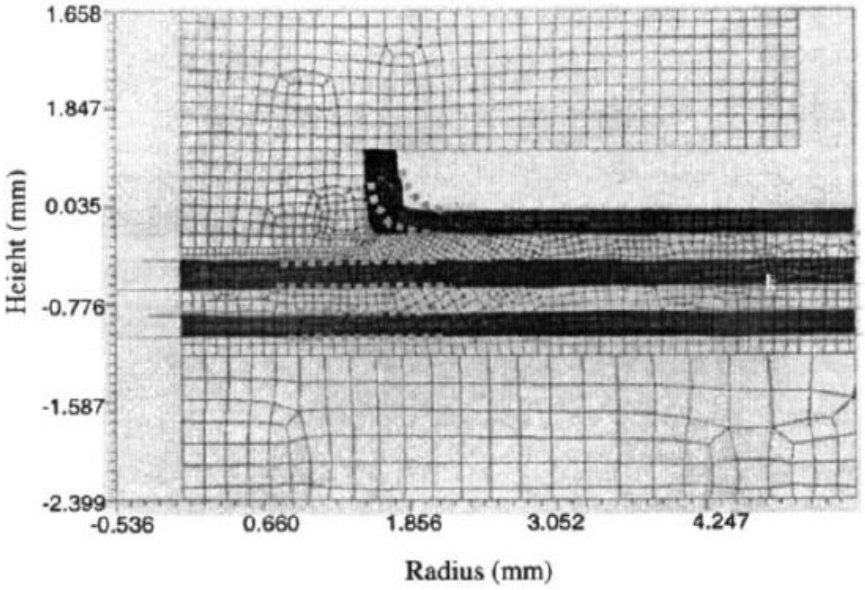

(a)

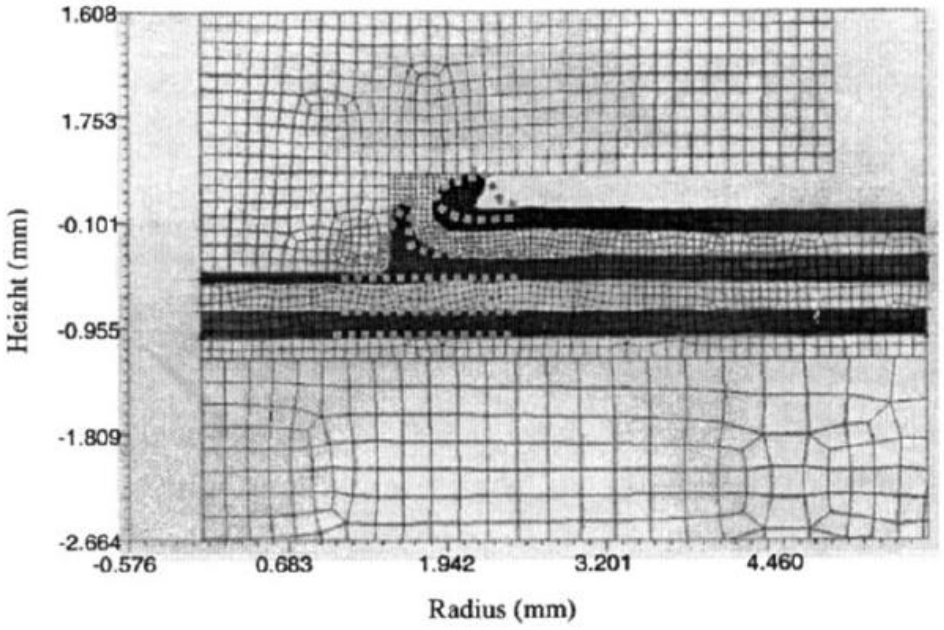

(b)

Figure 32: Simulation results of flow pattern at a) 300 µm and b) l500 µm embossing depth under non-isothermal embossing [30].

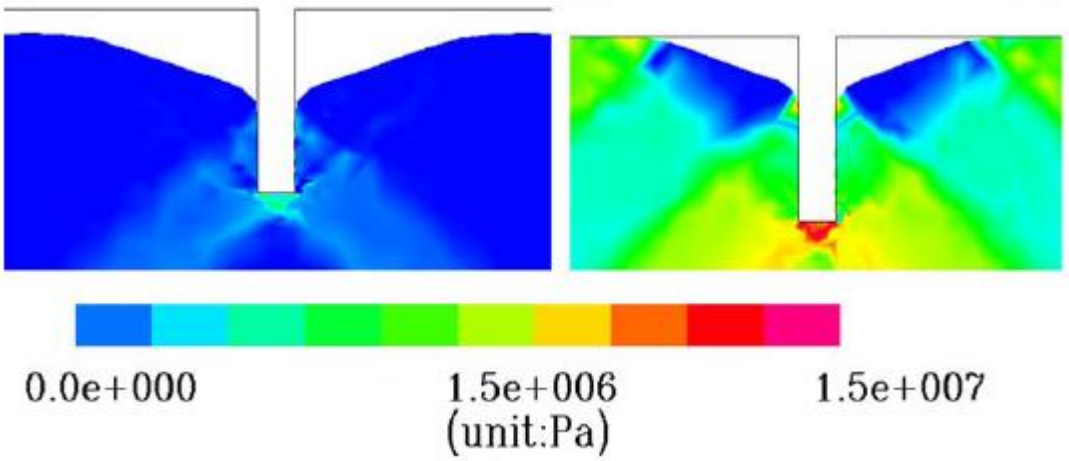

Figure 33: Distributions of the pressure for different depths of imprinting at a temperature of 180°C: (a) 400 nm and (b) 480 nm [31].

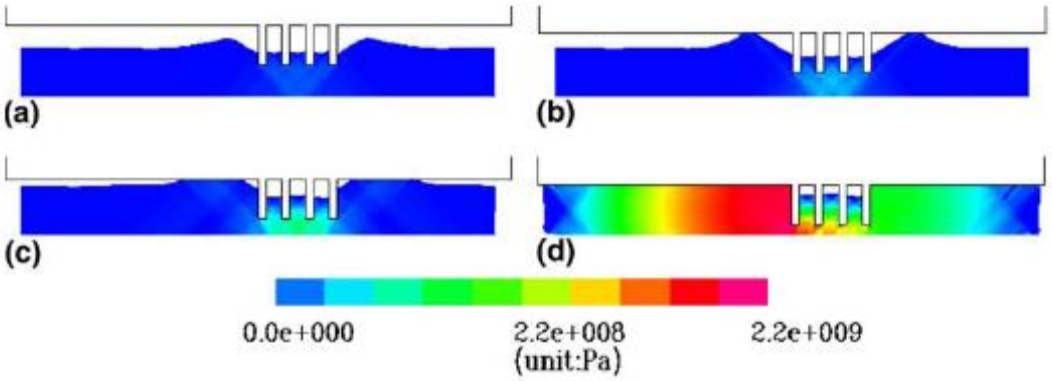

Figure 34: Distributions of the pressure for different depths of imprinting at a temperature of 180°C: (a) 200 nm; (b) 300 nm; (c) 400 nm; and (d) 480 nm [31].

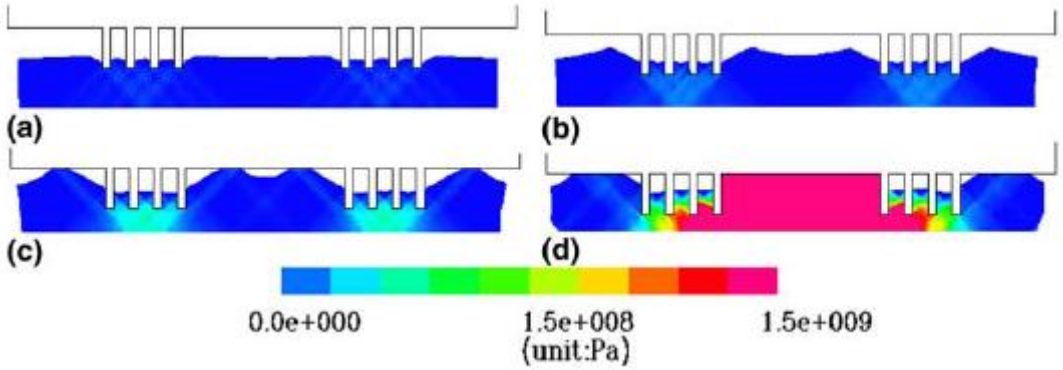

Figure 35: Distributions of the pressure for different depths of imprinting at a temperature of 180°C: (a) 100 nm; (b) 200 nm; (c) 320 nm and (d) 400 nm [31].

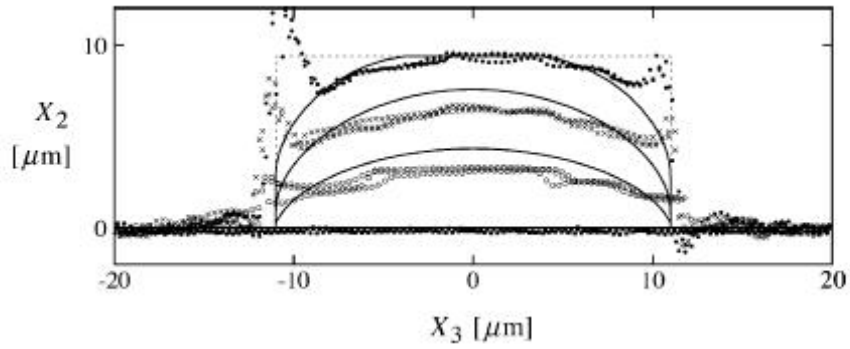

Figure 36: Shape of three microstructures developed at a characteristic shear rate of the flow of $v_0/H = 0.037\ s^{-1}$ where H = 0.50 mm at 170°C [32].

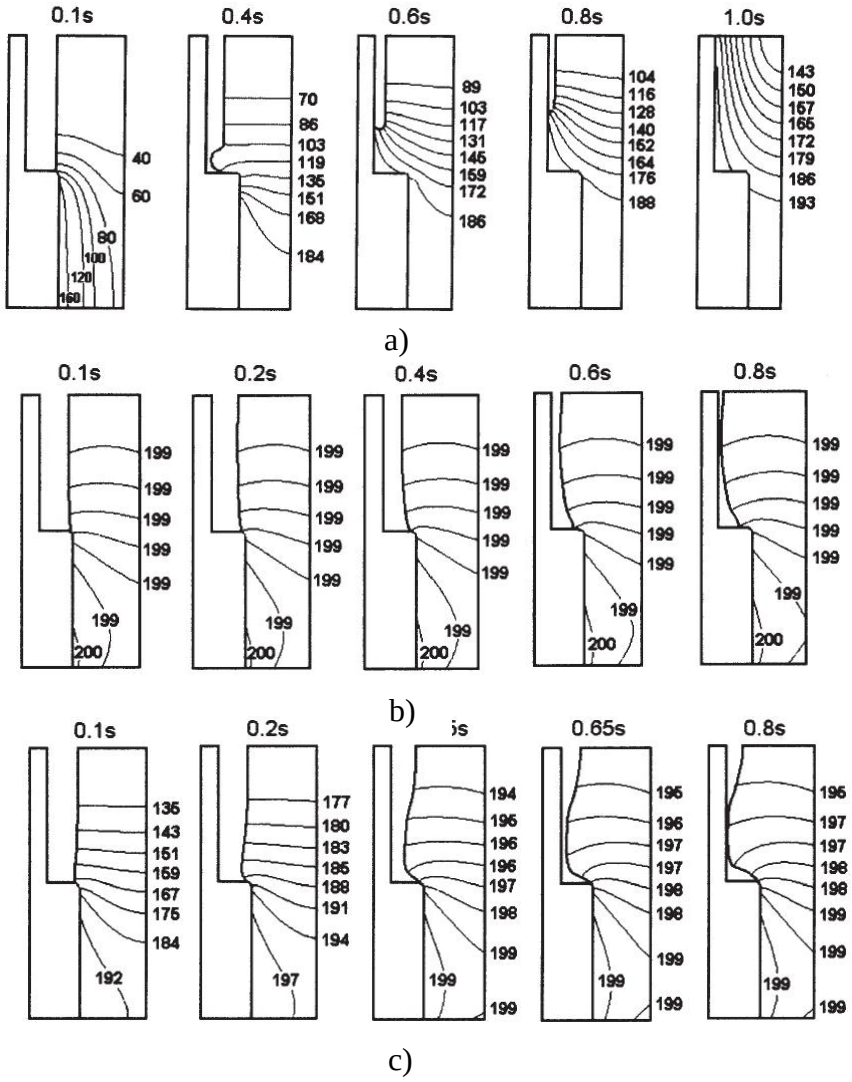

Figure 37: Flow front movement and temperature distribution inside the cavity for different cavity thicknesses: (a) 100µm, (b) 6µm, and (c) 25µm. The temperature distribution is shown in contours and in the unit of degree centigrade [33].

CHAPTER 3

TWO-STATION EMBOSSING

3.1 Abstract

This chapter reports a two-station embossing process that was developed by decoupling the heating and cooling processes during embossing through the use of shell-type molds. The separate heating and cooling stations reduces the large thermal mass associated with the mold. Experimental studies showed that aluminum stamps with a thickness of 1.4 mm can be rapidly heated from room temperature to 200°C in 3 s using contact heating against a hot station at 250°C. Microchannels and microlenses were successfully embossed onto HDPE substrates and ABS substrates, respectively, using a heating time less than 3 s and a total cycle time around 10 s.

3.2 Introduction

The major limitation of the hot embossing process is its long cycle time caused by mold thermal cycling. An embossing mold typically consists of two parts: a thin stamp with a thickness of 2 mm or less and a backup base. The material for the stamp can be silicon, glass, quartz, nickel, steel, or other similar materials although a durable metallic material is preferred. In the standard hot embossing process, the stamp is fastened, bonded, or welded to the base to form an integrated embossing tool while heaters and cooling channels are embedded in the base to thermally regulate the entire embossing tool. The relatively large thermal mass of the mold assembly, however, results in a long cycle time in hot embossing.

In this research, a two-station embossing process was developed and investigated for cycle time reduction. Fig.38 schematically shows the principle of the two-station process for mold rapid heating and cooling. The main design objective is to decouple the

heating stage from the cooling stage, thereby achieving energy efficiency and short thermal cycles. For this purpose, the heating and cooling stages are separately carried out on each of the two stations, namely a hot station and a cold station. To reduce the thermal mass, a thin-shell mold is used. Mold features (e.g. channels, microfeatures, welding patterns, etc.) to be embossed can be directly fabricated at the surface of the shell. During the heating stage, the shell is placed in contact with the hot station and rapidly heated through heat conduction. To ensure good interfacial contact, vacuum forces and non-permanent electromagnetic forces can be applied at the interface between the shell and the hot station. Because in hot embossing the polymer is pressurized against the other surface of the shell, the interfacial contact quality is greatly enhanced. Similarly, the cooling stage is carried out by contacting the heated shell with the cold station. It can be seen that, throughout the entire process, only a minimized thermal mass participates in the thermal cycling. More importantly, the insulation layer between the mold surface portion and the mold base, as used in most rapid heating and cooling methods, can now be eliminated. The hot and cold stations work as two separate mold bases for the tool surface portion (i.e. the shell) to selectively attach to during the process. Because of this decoupled design, the new process is also free from the interfacial thermal mismatching problem [21,47,48], as encountered in other rapid heating and cooling approaches.

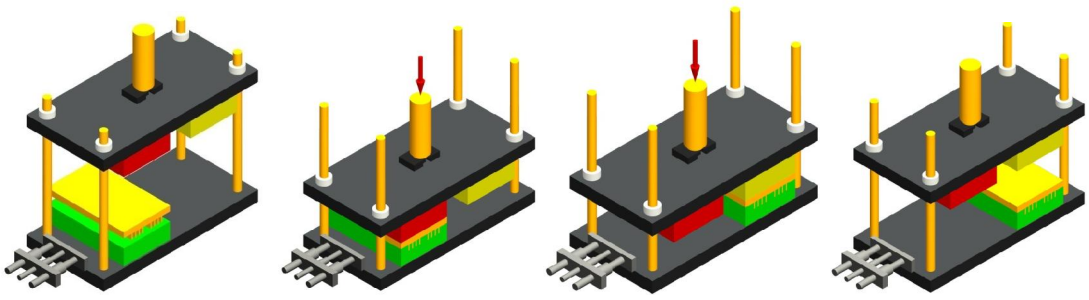

a) b) c) d)

Figure 38: Two-station embossing process: a) startup, b) embossing stage, c) cooling stage, and d) mold opening stage.

The fundamental steps involved in thermoplastic molding include melting/softening, deformation, holding, and cooling. The two-station embossing approach follows a similar sequence of operations. The shell mold at room temperature T_0 is placed over the polymer substrate. The hot station maintained at temperature higher than the polymer softening temperature is brought in contact with the mold and heats the mold through heat conduction. The time t_0 corresponds to the start of the heating stage (Fig.39). The heating stage is followed by the embossing stage which starts at time t_1 when the mold temperature reaches T_1, equal to the polymer softening temperature. During the embossing stage the polymer deforms and fills up the mold cavity. After mold fill, the embossing pressure p_0 is maintained, and the corresponding holding stage lasts until time t_2. At time t_2, the mold is opened for switchover to a cold station; the mold and the polymer substrate still above the polymer softening temperature are moved to the cooling station, and the pressure is reapplied at time t_3. The cooling station is maintained at room temperature. A holding step is performed simultaneously with the cooling stage. This additional holding step plays a critical role in compensating for thermal shrinkage and achieving high dimensional accuracy. At the end of the holding and cooling stage, i.e., at time t_4, the polymer at a temperature close to the room temperature is removed out of the mold. The difference between t_3 and t_2 corresponds to the time used for moving the mold and the embossed polymer from the hot station to the cooling station.

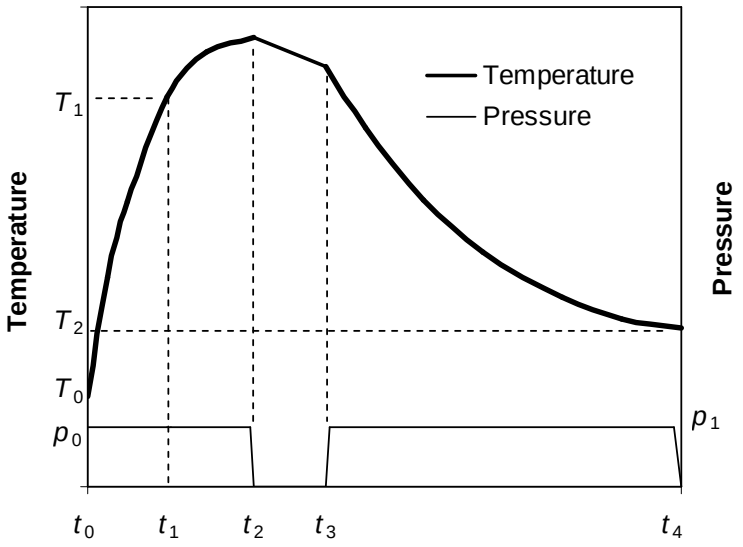

Figure 39: Illustrative temperature and pressure history of the stamp during a two- station embossing cycle. T_0, T_1, and T_2 are the initial temperature, the polymer softening temperature, and the mold opening temperature. p_0 and p_1 are the embossing pressure and holding pressure, respectively. The pressure used during holding/cooling may be different from that during embossing. t_0, t_1, t_2, t_3, t_4 are time instants. At time t_0, contact heating starts. At time t_1, the stamp reaches the polymer softening temperature. The time between t_2 and t_3 is used for switchover. At time t_4, the mold is opened.

3.3 Experimental

3.3.1 Material

HDPE and ABS were used as two embossing polymers. Both polymers were in sheet forms with a thickness of 3.2 mm, obtained from McMaster Carr Supply Company.

3.3.2 Shell Mold Fabrication

An ultraprecision machining process involving slow tool servo control and single-point diamond cutters was used for the fabrication of shell molds. The ultraprecision machine has three linear axes that are equipped with linear lasers scales capable of resolving 8.6 nm at a maximum speed of 1800 mm/min. The straightness on all slides is less than 250 nm over the entire travel distances. The work spindle can be operated at

6,000 rpm with axial and radial motion error of less than 25 nm. The work spindle can also maintain angular position to less than 0.5 arc second in modulated mode. During a diamond turning process, the Y axis may be fixed, i.e., Y position remained constant while the spindle is rotating or the Y axis can be moving but (usually) the spindle rotation is fixed (controlled by the servo motor directly coupled to the spindle). Two types of metallic shell stamps, one with protruded rings of microfeatures on an aluminum disk and the other with a plurality of microlenses on a brass disk, were fabricated using the ultraprecision machining process. Both disks are 1.4 mm thick and 25.4 mm in diameter. The four protruded circular ribs (only partially shown in Fig.40a) on the microchannel embossing stamp are 50 μm wide and 100 μm high. The lens pockets on the microlens embossing stamp are 80 μm in opening and 8 μm deep (Fig.40b).

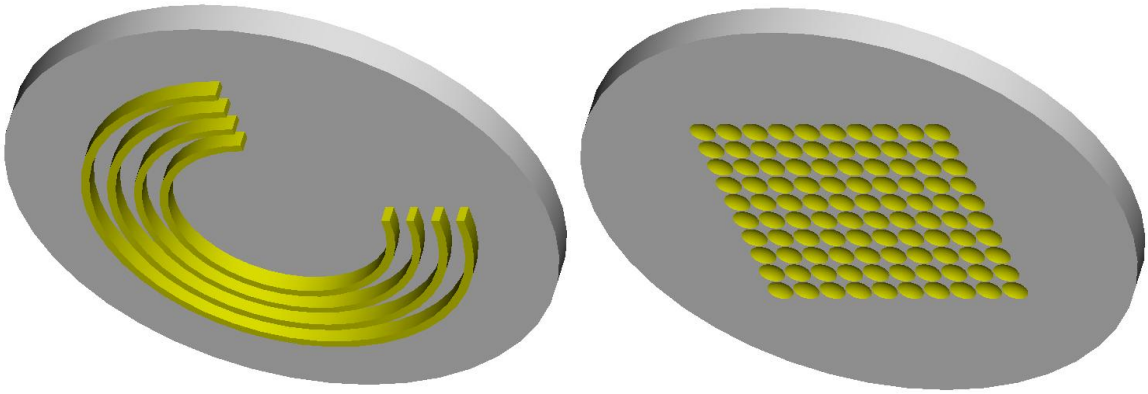

(a) (b)

Figure 40: Geometries of the stamps used in two-station embossing experiments: a) an aluminum stamp for microchannel embossing, and b) a copper stamp for microlens embossing. Both stamps are 1.4 mm thick and 25.4 mm in diameter. The four protruded circular ribs on the microchannel embossing stamp are 50 μm wide and 100 μm high. The lens pockets on the microlens embossing stamp are 80 μm in opening and 8 μm deep.

3.3.3 Two-Station Embossing Setup

A pneumatic press was modified for two-station embossing, as shown in Fig.41. The customized embossing setup consists of a Janesville tool 5000 series pneumatic press and a platen assembly. The pneumatic press has a precision machined four-post casting that incorporates a multistage cylinder with a load capacity of 27 KN. The pneumatic press was connected to an air compressor, capable of delivering 70 psi (0.5 MPa) by means of an air purifier and regulator. The air purifier was found to be essential since it reduced the clogging of the piston during the embossing process. The embossing pressure was regulated by controlling the inlet air pressure to the pneumatic press.

The platen assembly consists of a stationary or lower platen and a moving or upper platen, as shown in the Fig.41. The stationary platen was fastened to the base of the pneumatic press by means of a lock screw. The moving platen is connected to the piston of the pneumatic press by means of a stainless steel threaded stud. The daylight opening between the mold and the base plate was set to approximately 5 cm by adjusting the threaded stud connecting the platen and the piston. This was done to ensure that there was no contact between the mold and the polymer substrate prior to the embossing process. The hot and cold plates were attached to the upper platens. Both the hot and the cold plates are made of stainless steel (420 SS), each with a platen size of 75 x 75 mm. The top and bottom surfaces of the steel plates were precision ground. Two circular channel of diameter 12.5 mm machined along the length of the hot plate were inserted with two 240 W cartridge heaters. The temperature of the hot plate was controlled by a closed loop, single input, double output programmable Micromega controller. In order to achieve tight control over the processing temperature, the controller was programmed under Auto PID control. A “K” type thermocouple inserted into a circular slot on the back of the hot plate was used to read and regulate the temperature of the hot plate through feedback control.

The hot and cold plates were fastened to the moving platen of the pneumatic press assembly by four tap screws. A 75 x 75 mm calcium silicate board of thickness 12.5 mm was placed between the hot plate and the moving platen of the press assembly to prevent heat loss through the platen. . The hot station was maintained at a constant heating temperature of 250°C. The cold station was kept at room temperature. The embossing load used was around 270 N for all samples. When the embossing stage was completed, typically less than a few seconds, the embossed polymer together with the shell mold was switched from the hot station to the cold station and cooled under the same force as the embossing force.

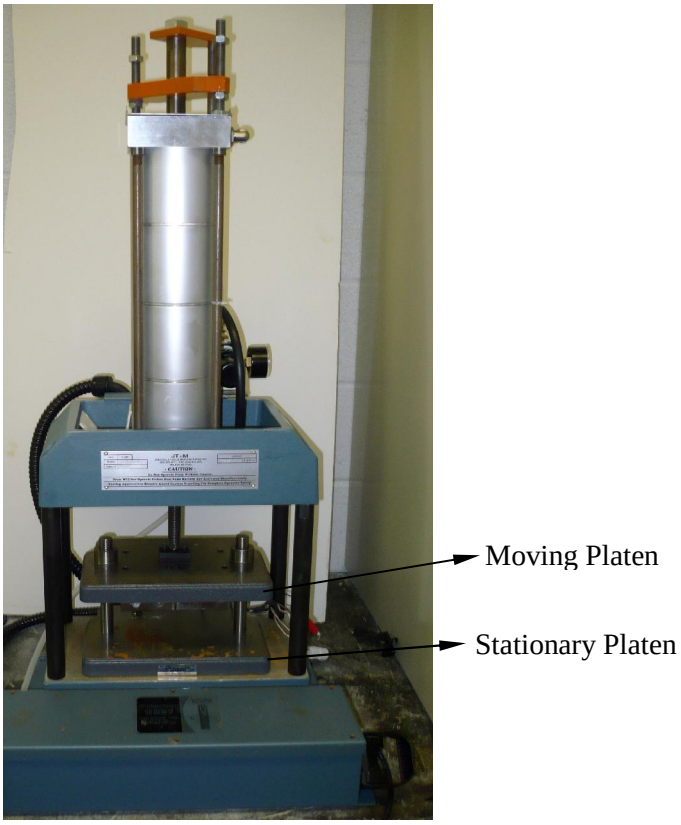

Figure 41: Two-station embossing setup showing retrofitted pneumatic press with stationary and, moving platens.

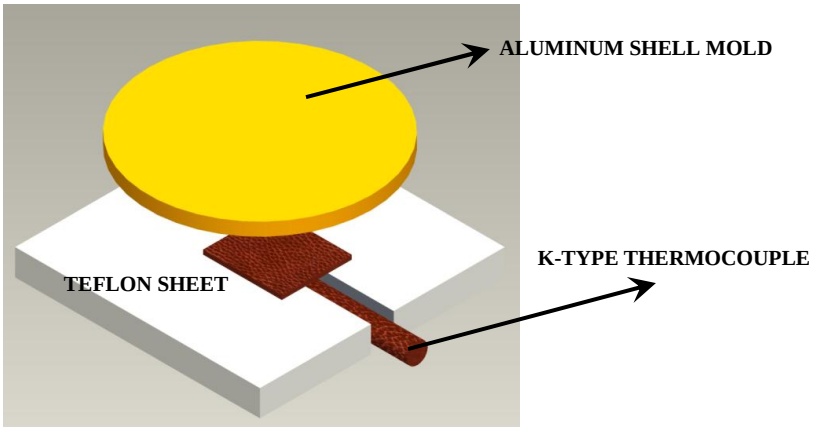

Figure 42: Aluminum mold with a thermocouple assembly for heating response experiments.

3.3.4 Heating and Cooling Response Experiments

Experimental studies were carried out to understand the heating and cooling response of the shell type mold during two-station embossing. In this study, an aluminum disk of diamenter 25 mm and thickness 1.4 mm with precision surface finishes and a steel plate of 50 × 25 × 1 mm were used as thin-shell mold. The hot station was maintained at 250°C and the cold station was left at room temperature. The large lower platen of the press was also left at room temperature. A Teflon sheet with a thickness of 3 mm was laid on the bottom platen. The metal disk was placed on the top of the Teflon sheet. Between the Teflon sheet and the metal disk a K-type thermocouple was installed for measuring the shell surface temperature, as shown in Fig.42. A rectangular channel was cut along the center of the Teflon sheet for accommodating the thermocouple wire. The use of the rectangular channel eliminated errors in measurements caused by possible interference with the thermocouple wire. The thermocouple was connected to an Omega PDaq temperature monitor capable of recording 25 temperature measurements per second.

During the heating stage, the hot station was forced against the metal disk. As the heating stage progressed, the temperature data was simultaneously recoded by the monitor. At the end of the heating stage, the pressure was released, the mold along with

the thermocouple and the Teflon base was moved to the cooling station, and the pressure was reapplied. Various heating times and cooling times were employed during the experiments to study the effects of these process parameters on the heating and cooling performance of the mold.

3.4 Two-Station Embossing Results

3.4.1 Heating Response

Fig.43 shows the experimental heating response of a 1.4 mm-thick aluminum shell in contact with the stainless steel hot station which had a set temperature at 250°C. Several trials were made and the results were consistent, as shown in the Fig.43a. It is seen that, in about 3s, the shell surface temperature can be heated to 200°C. For the four volume plastics (i.e., polyethylene, polystyrene, polyvinylchloride, and polypropylene), this temperature is high enough for softening the polymer. For polymers with higher softening temperatures, the heating temperature within a designated period of time can be effectively raised by increasing the hot station temperature. Fig.43b. shows the heating response of a 1-mm-thick steel shell in contact with the stainless steel hot station set to 250°C. Although it is thinner than the aluminum shell, the stainless steel took longer to reach 200°C. It now takes about 4.5 s for the shell surface to reach 200°C.

Integrated heating and cooling responses of the 1.4-mm-thick aluminum shell are shown in Fig.44. The shell was heated for 5 s then switched to cooling. However, because of the slow movement of the pneumatic press, it took about 5 s for the switchover from heating to cooling. Three trials are shown in Fig.44 and some inconsistency owing to the limitation of the machine exists. Despite this limitation, fast cooling can be observed. All the above experiments were conducted using a compression force of about 2500 N. The corresponding pressure acting on the shell is 5 MPa. Since the pressure may have a significant effect on the interfacial conductance, a higher level of

compression force (3 times as high) was also used for comparative studies. However, the difference between the results before and after the change was unnoticeable. Nevertheless, it may not be concluded that the pressure has barely any effect on the thermal response, but rather it is believed that at these pressures the change of the contact condition (i.e. the contact condition between the surface asperities of the two mating surfaces) is little.

The two-station strategy is not limited to hot embossing, but rather it can be applied to different thermoplastic molding and forming processes wherever rapid thermal cycling is needed. The technical implementation is straightforward if the mold to be used has generally a flat surface. Examples include embossing/stamping of surface features and welding/sealing of thermoplastic films/sheets. For surfaces with generic contours, as encountered in thermoforming and compression molding, the surface contours of the hot and cold stations need to be modified accordingly. In these more demanding cases, special efforts may be needed to promote uniform contact between the two contoured surfaces. One possible enhancement is to employ high-temperature and highly conductive grease between the two contoured surfaces.

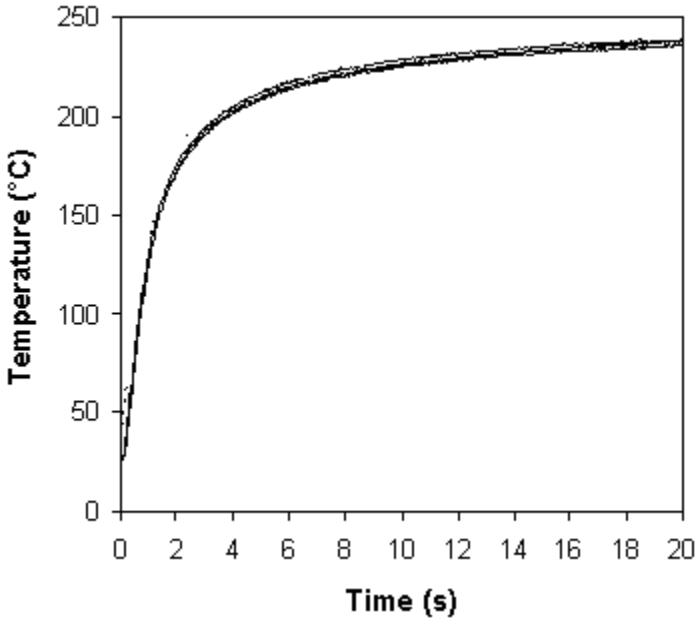

a)

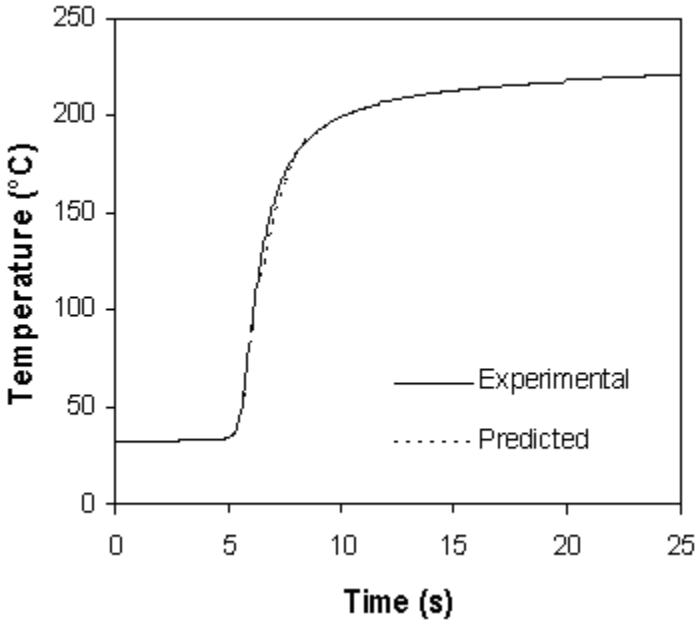

b)

Figure 43: Heating response of shell molds: a) a 1.4-mm-thick aluminum stamp and b) a 1-mm-thick steel stamp, in contact with a stainless steel hot station at 250°C.

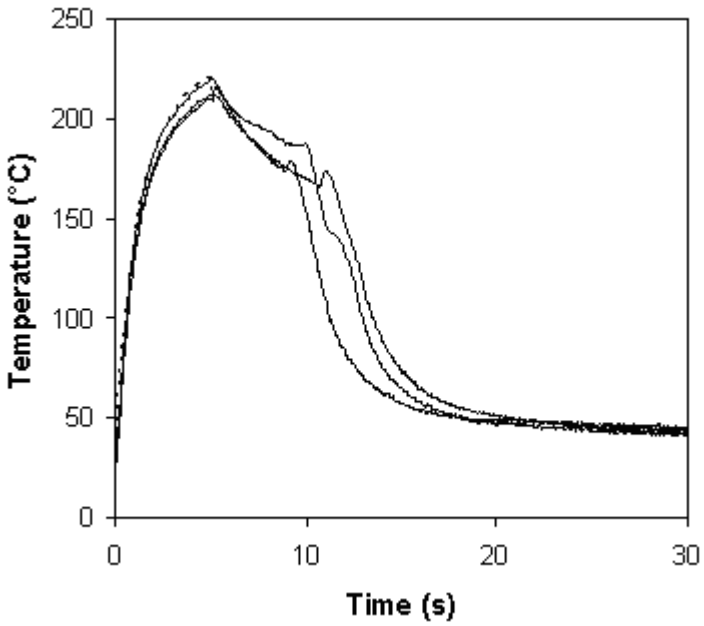

Figure 44: Thermal cycling of .a 1.4-mm-thick aluminum shell mold in contact with a hot station at 250°C and a cold station at 25°C

3.4.2 Microchannel Embossing

The embossed microchannels (a negative pattern to the microribs in Fig.40a) on HDPE substrates using the two-station embossing strategy are shown in Fig.45. With the two-station strategy, microchannels were successfully fabricated on the HDPE substrate with a heating time less than 3 s and a cycle time around 10 s (Fig.45a). By investigating the replication quality at the edge of the microchannel (Fig.45.b), it can be seen that good replication fidelity was obtained with this short cycle time. As compared with the standard hot embossing process with typical cycle time of 10 min or longer [49], the reduction in cycle time is indeed substantial. Further, it should be noted that thick polymer substrates (e.g. 3.2 mm in this study) can be effectively embossed with the two-station strategy. The standard hot embossing process is typically limited to very thin polymer substrates because thick substrates involve higher thermal load, resulting in even

longer cycle time and increased potential of material degradation. Using the two-station strategy, a minimal thermal load is applied to the polymer substrate, thereby eliminating these problems.

3.4.3 Microlens Embossing

The brass shell mold with the negative pattern of a microlens array was used for embossing experiments on ABS substrates. Different contact heating times, namely, 1 s, 3 s, 6 s, and 10 s, were used with a hot station temperature at 250ºC. At 1 s of heating time, there was no replication on the ABS substrate, judged by scanning electron microcopy (SEM). At 3 s of heating time, good replication of the lens array was achieved, as shown in Fig.46. In this case, the total cycle time (including the necessary cooling time for mold opening) was around 10 s. The zoomed view in Fig.46.c shows surface defects on the master, formed when the diamond tool rubbed against the surface during machining. These defects were found to replicate themselves very well to the ABS substrate (Fig.46d). When the heating time increased to 6 s, there was unnoticeable change in the replication quality. However, at the 10 s heating time, some detached residuals were found in the center of the embossed lens, as shown in Fig.47. This appears to be caused by the excessive adhesion between the polymer and the copper stamp developed under pressure and heat during the prolonged embossing stage. In hot embossing and micro injection molding, the traditional methods for promoting mold separation using mold releasing agents become inappropriate because of the small size of the part feature. In this case, proper adjustment of the embossing and holding stages becomes critical for achieving a balanced outcome between ease of demolding and effectiveness of shrinkage compensation.

Surface topographies (obtained using a Veeko Wyko NT1100 Optical Profilometer) for both the master feature and the embossed lens are shown in Fig.48. The

roughness resulting from diamond machining on the master can be clearly seen and it was transferred to the embossed lens. A quantitative comparison of the contour profiles of the microlens array on the ideal surface, the machined mold surface, and the embossed polymer surface (with 3 s of contact heating) is provided in Fig.49 (obtained using a Veeco Dektak Series 3 stylus profiler). The ideal profile refers to the profile used in the CNC programming. It can be seen there are small deviation from the ideal profile to the machined profile. The embossed profile appears to have smaller curvature (reciprocal of the local radius) than the one on the mold. This is believed to be caused by the nonlinear shrinkage and viscoelastic nature of the polymer, which may be minimized with increased holding pressure and time.

3.5 Biomimetic Transfer Using Two-Station Embossing

Biomimetic surface structures such as anti-reflective protrusions on the moth eye and self cleaning pillars on the lotus leaf have a profound influence in the development of technologically important engineering devices and systems. In this study, we prepared microstructured polymer surfaces that mimic the surface patterns on the pronotum and the wing of dung beetles (Phanaeus vindex shown in Fig.50) using two-station embossing techniques. A sequential approach involving two-station embossing was used to transfer the surface structures on the dung beetle to polymer substrates, as illustrated in Fig. 51.The major steps involved were sputtering, electroforming and two-station embossing.

3.5.1 Sputtering

Samples of the pronotum and wing sections of the dung beetle were sputter coated with gold. The sputtering was carried out for a period of 5 min with current at 20 mA under vacuum of 0.7 torr. The resulting gold layer is of 10s of nanometer in thickness.

3.5.2 Electroforming

The sputter-coated insect pronotum and wing samples were degreased first using a special degreasing solution for electroplating. One edge of the sample is then glued using a conductive silver adhesive to a copper wire (7 mm in diameter, used as an electrode). The electroforming process was carried out in a Caswell electroplating rectifier. The main difference between electroplating and electroforming is the amount of current and time used. Over the total electroforming period of 48 hours, the current was set at 50 mA. With higher current, the electroformed nickel tends to be brittle. The uniform deposition of the metal over the substrate was enabled by the constant agitation of the bath. The PH value of the electrolyte was maintained between 4.5 and 5.5 during electroforming to prevent any adverse peeling effects.

3.5.3 Two-Station Embossing Of Biomimetic Surface.

The electroformed nickel shell was peeled off from the insect section. After some unwanted electroforming residuals surrounding the shell and near the electrode were trimmed off, the nickel shell was directly used as an embossing master. The two-station embossing approach was used for pattern transfer with an embossing time of 5 s and a cooling time of 10 s.

The embossed ABS samples were gold sputtered and investigated using a digital stereomicroscope. The natural surface of dung beetle has a unique topography consisting of cordillera, ridges, islands and valleys. The lateral size of these features ranges from less than 50 to 200 μm, depending on the location and types of features. Smaller parasite features can also be seen on large features, such as cordilleras. The results on feature transfer of the surface structures on the wing (at two different locations A and B) are shown in Fig.52 and Fig.53. The characteristic feature size at location B is a little larger

than that at location A. The micrographs showed good feature transferring faithfulness at both locations. The nickel stamp has the negative pattern of the natural surface. The ridges on the initial surface now become valleys and the valleys become ridges. After embossing, these negative features are turned back to the positive ones. It should be noted that in feature transfer, at least 2 transfers are needed to restore the original pattern. Thus, if one directly uses the natural surface as the master for feature transferring to the final polymer surface, an undesired negative pattern will result. In contrast, if soft molding is used before electroforming as the first step in feature transferring, the original pattern can be recovered, but totally 4 transfers are needed. The increased number of transfers will certainly depreciate the transfer accuracy. Fig.53 shows the transferring quality of surface features on the pronotum. From the comparison, it is seen that comparable features to those on the pronotum were produced on ABS substrates. Fig.54 compares the contact angles of the ABS surfaces before and after being patterned with the biomimetic structure. The original ABS surface is hydrophilic with a water-contact angle of about 44°. The patterned ABS surface with the biomimetic structure, however, is hydrophobic, with a water contact angle from 90° to 96° depending on the location of the initial surface. This contact angle on the synthetic polymer is comparable to those of the original dung beetle surfaces as reported by Jin et al. [51].

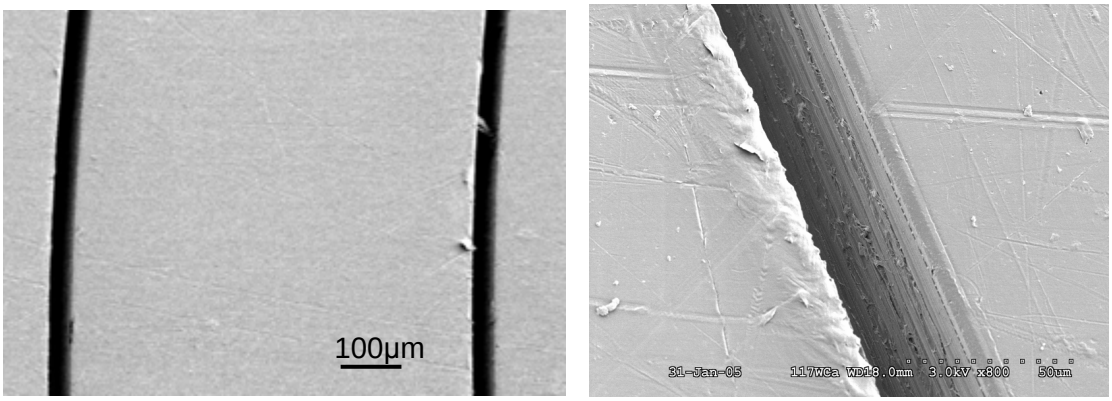

a) b)

Figure 45: Two-station embossing of microchannels on HDPE substrates: a) replicated microchannels, and b) replication at the edge of the microchannel.

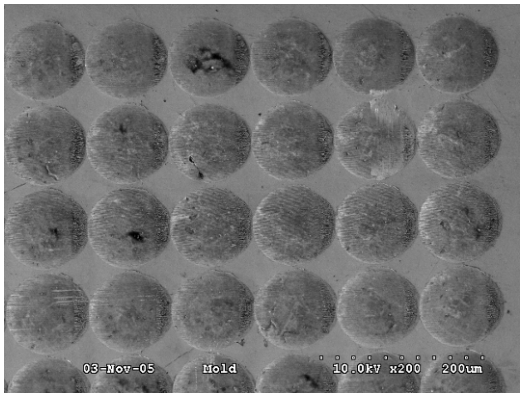

(a)

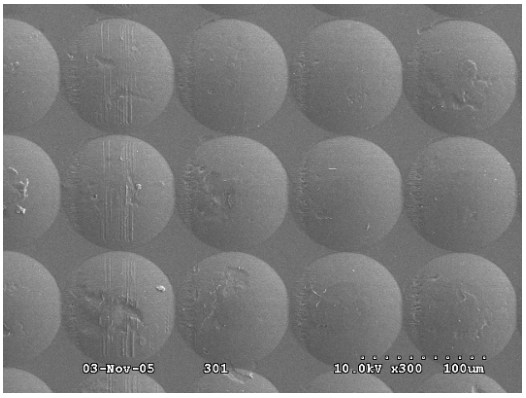

(b)

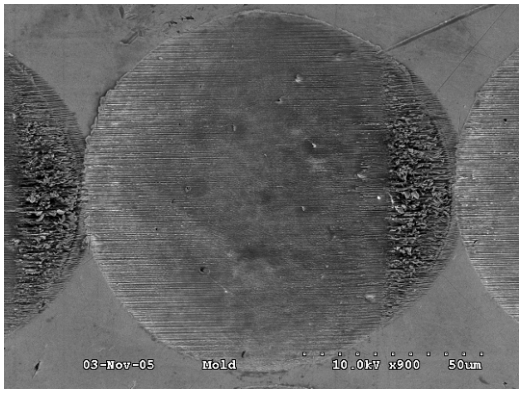

(c)

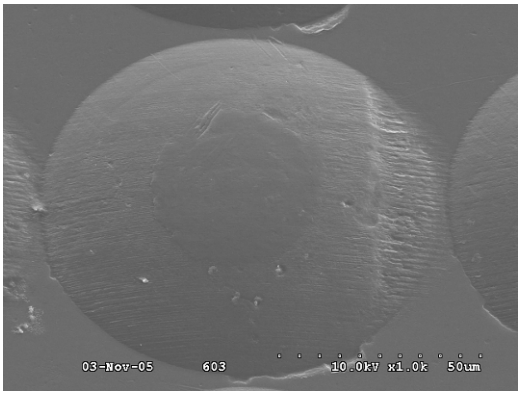

(d)

Figure 46: SEM of microlens arrays: a) the embossing master, b) the embossed ABS surface, c) local features of a lens pocket on the master, and d) local features of a microlens on the embossed ABS substrate. The microlenses were embossed using a 3-s contact heating time.

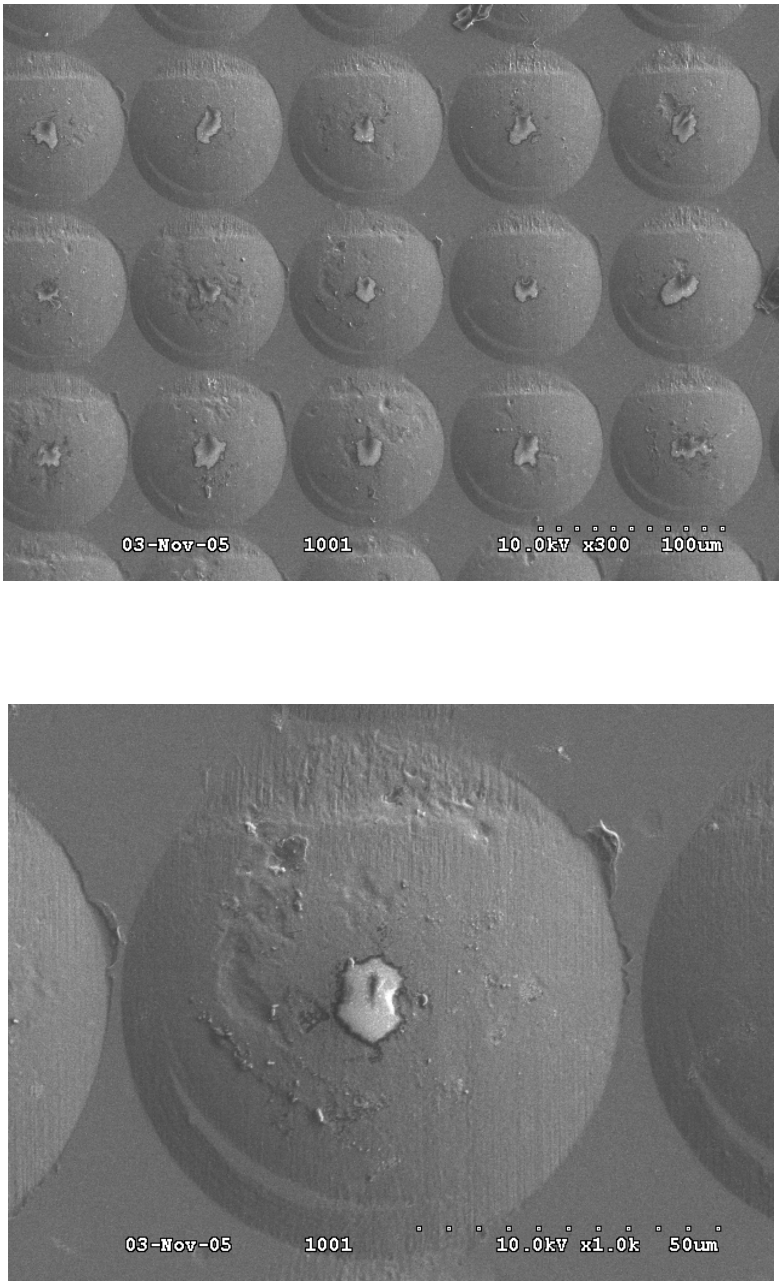

Figure 47: SEM of microlenses embossed using a contact heating time of 10 s.

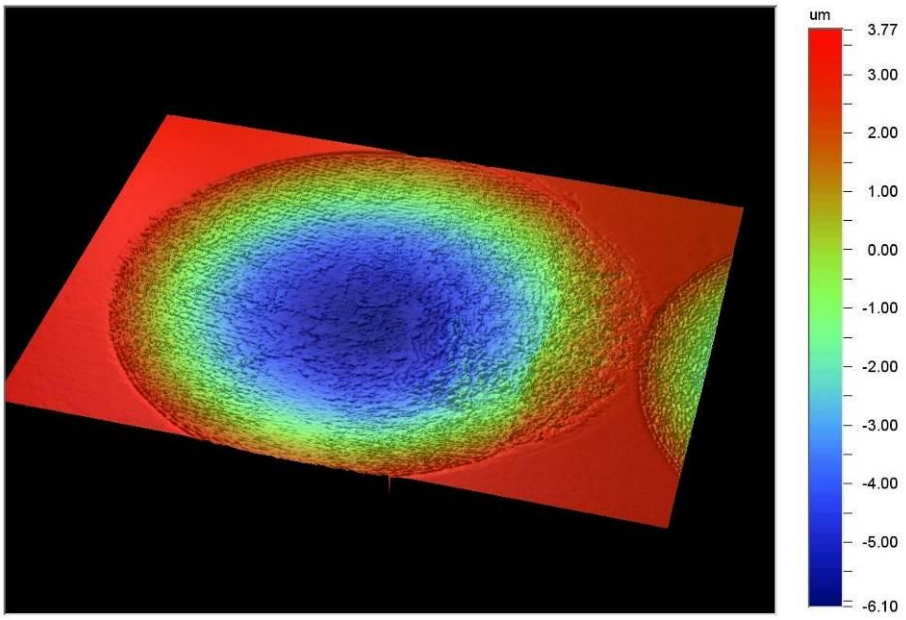

(a)

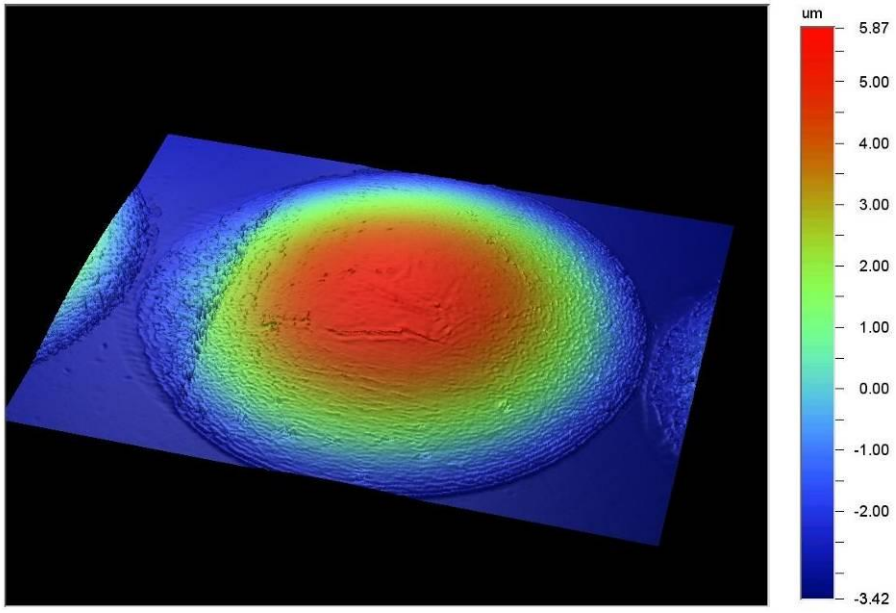

(b)

Figure 48: Surface topography of microlens arrays: a) the embossing master, and b) the embossed ABS surface.

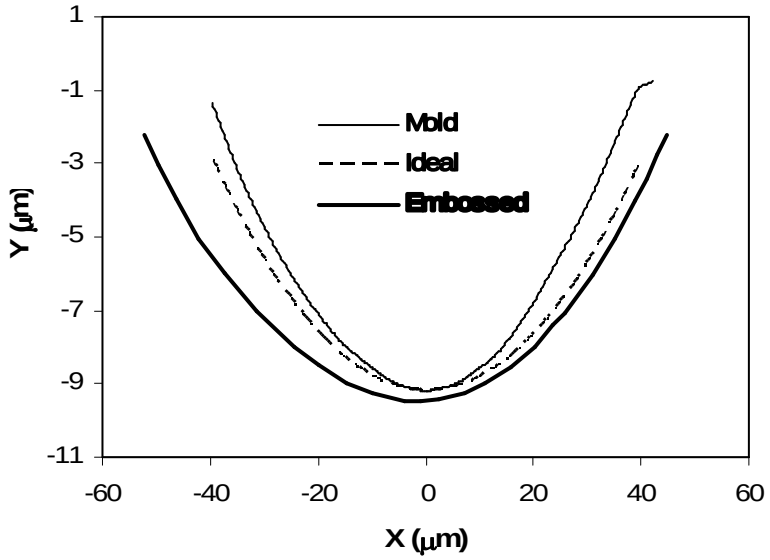

Figure 49: Comparison of the contour profiles of the microlens array on the ideal surface, the machined mold surface, and the embossed polymer surface (with 3 s of contact heating).

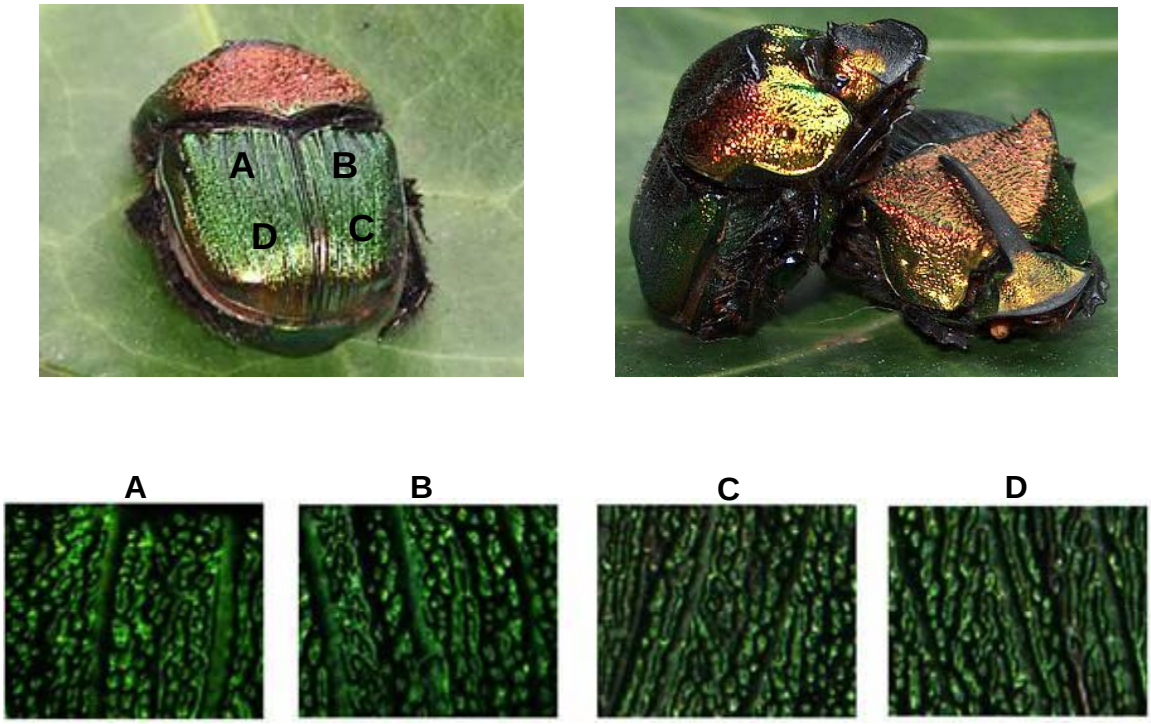

Figure 50: Dung beetle (type: Phanaeus vindex) with its wing surface structures. A, B, C and D denote different locations on the wing.

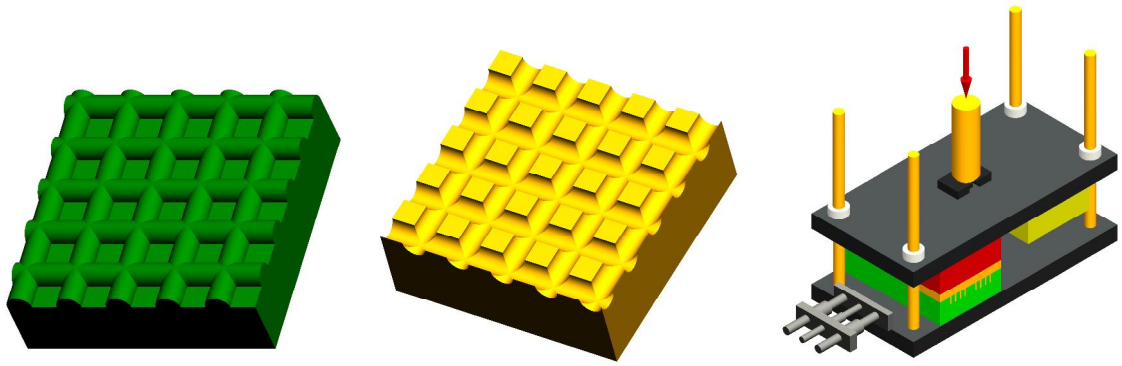

a) b) c)

Figure 51: Sequential steps involved during biomimetic transfer of functional structures on to ABS: a) sputtering on wing, b) die electroforming, and d) pattern transfer through two-station embossing.

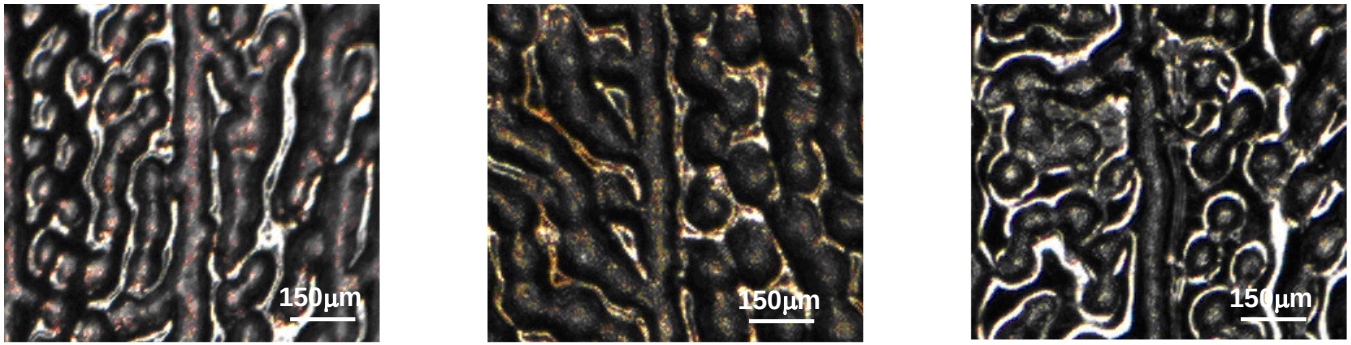

a) b) c)

Figure 52: Replication of the surface structures at wing location A to ABS: a) gold-sputtered original wing structures, b) structures on the electroformed nickel mold, and c) embossed structure on ABS.

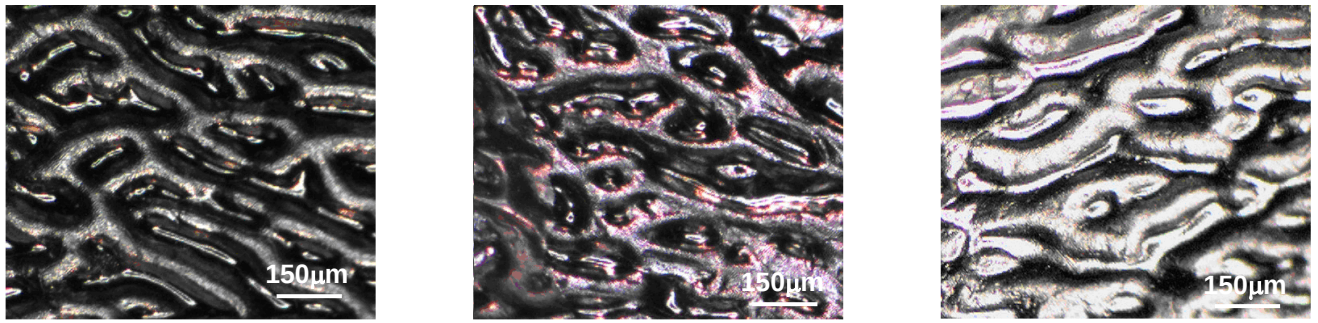

a) b) c)

Figure 53: Replication of the surface structures on the pronotum to ABS: a) gold-sputtered original wing structures, b) structures on the electroformed nickel mold, and c) embossed structure on ABS.

a)

b)

Figure 54: Contact angle measurement on the standard and patterned ABS surface: a) non-patterned surface, b) patterned ABS surface.

CHAPTER 4

MODELING OF TWO-STATION EMBOSSING

4.1 Abstract

Chapter 3 covered experimental studies on two-station embossing process. The experimental results showed aluminum shell molds with a thickness of 1.4 mm can be rapidly heated from room temperature to 200°C in about 3 s using a hot station at 250°C and surface microfeatures can be transferred from thin metallic stamps to polymer substrates with cycle times less than 10 s. In chapter 4, numerical simulation results are presented. The simulations were performed to study the effect of different design parameters, including thermal contact resistance, shell material and shell thickness, on the thermal response at the mold surface. The two-station embossing process for the microlens was also numerically studied. The simulated filling behavior agreed with the experimental observation and the predicted thermal and deformation history of the polymer offers a good explanation on the experimentally observed process characteristics.

4.2 Introduction

The quality of a molded part is affected by design variables (e.g., the embossing technique, the shape, curvature and thickness of the mold, etc.), process variables (e.g., embossing rate, pressure, temperature, etc.) and material variables (e.g., rheological behaviors, chemical properties, thermal stability, etc.). From Fig.55, it can be seen that the two-station embossing process is controlled by multiple process parameters, including embossing time (t_2 - t_0), embossing pressure (p_0), switchover time (t_3 - t_2), holding pressure (p_1), cooling time (t_4 - t_3), hot station temperature, cold station temperature, and initial polymer temperature. The contact heating time is equal to the embossing time. The

holding stage and cooling stage occur simultaneously, and are therefore not listed separately. These process parameters may interact with each other to have a combined effect on the replication quality. To understand the characteristics and scalability of two-station embossing, it is helpful to study the evolution of the thermomechanical history of the polymer during the process. The thermomechanical history, however, is a function of multiple design and process variables, and is difficult to measure using an experimental approach. Mathematical modeling allows us to establish a fundamental understanding on the effects of these variables through solutions to the governing equations representing the process, thus enabling more efficient design and setup of the process. In this study, mathematical modeling along with rheological characterizations were undertaken to understand and establish the effects of the major design and process parameters during two-station embossing.

4.3 Modeling of Heat Transfer through the Shell Mold

During the two-station embossing process, essentially three slabs of materials are involved, namely, a polymer layer to be deformed, a metallic shell mold to be heated and cooled, and a bulky metallic base (either the hot station or the cold station), as shown in Fig.56. Heat transfer in such a system can be considered to be one-dimensional. The heat diffusivity of the polymer is typically two orders of magnitude lower than those of the metallic shell and the metallic base. If the temperature at the polymer-to-shell interface (referred to as shell surface hereinafter) is of interest and the time is short (e.g., less than several seconds), the polymer layer may be safely dropped in the model without a significant influence on the solution accuracy. Conduction of heat in multi-slab systems is documented in detail in the textbook by Carlslaw and Jaeger [52]. In the case when the thermal contact resistance between neighboring layers can be neglected, analytical solutions can be readily obtained using the Laplace transform technique for many cases under various initial and boundary conditions. Particularly, Jansen [53] analytically

solved the heat conduction problem in a multilayer injection molding system assuming zero thermal contact resistance between layers. In more complicated cases, numerical methods are usually needed in obtaining solutions.

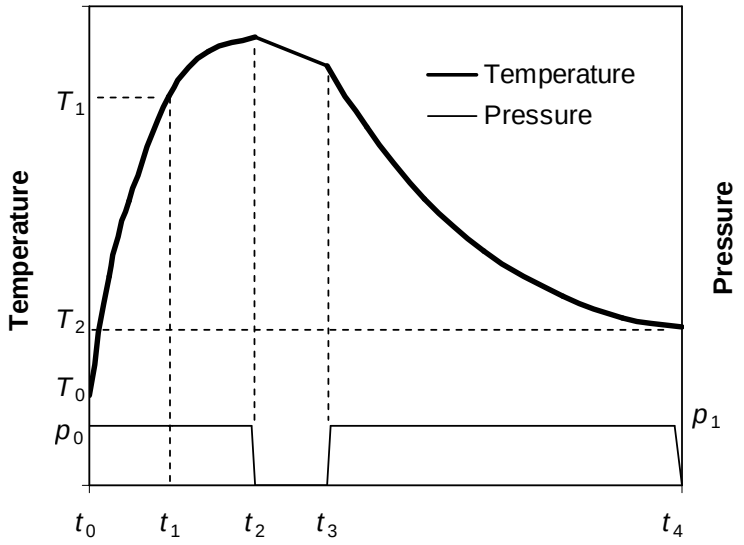

Figure 55: Illustrative temperature and pressure history of the stamp during a two-station embossing cycle. T_0, T_1, and T_2 are the initial temperature, the polymer softening temperature, and the mold opening temperature. p_0 and p_1 are the embossing pressure and holding pressure, respectively. The pressure used during holding/cooling may be different from that during embossing. t_0, t_1, t_2, t_3, t_4 are time instants. At time t_0, contact heating starts. At time t_1, the stamp reaches the polymer softening temperature. The time between t_2 and t_3 is used for switchover. At time t_4, the mold is opened.

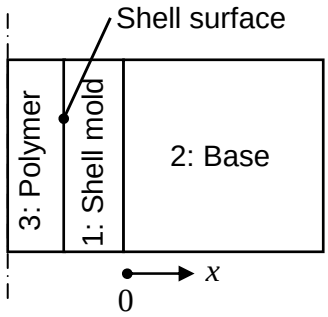

Figure 56: Three slabs of materials involved in the two station process.

At the start of the heating stage, the shell mold is forced against the hot station. The governing equations in this case can be written as:

$$\frac{\partial^2 T_1}{\partial x^2} - \frac{1}{\alpha_1}\frac{\partial T_1}{\partial t} = 0, \text{for} - l_1 < x < 0, t > 0 \tag{4}$$

$$\frac{\partial^2 T_2}{\partial x^2} - \frac{1}{\alpha_2}\frac{\partial T_2}{\partial t} = 0 \text{ for } 0 < x < l, t > 0 \tag{5}$$

where $T, x, t, l, \text{and } \alpha$ are temperature, coordinate, time, thickness, and thermal diffusivity, respectively. The subscript denotes the layer index, i.e., "1" for the shell mold and "2" for the hot base. With zero thermal resistance at the interface of separation, the boundary conditions are:

$$k_1 \frac{\partial T_1}{\partial x} = k_2 \frac{\partial T_2}{\partial x}, \text{for } x = 0, t > 0, \tag{6}$$

$$T_1 = T_2 \text{ for } x = 0, t > 0, \tag{7}$$

The shell surface temperature, $T_s(t)$, can be analytically obtained, given initial conditions of $T_1 = T_i$ and $T_2 = T_h$ at $t = 0$ and an assumption of $l_2 >> l_1$,

$$\tilde{T}_s(t) = \frac{T_s(t) - T_i}{T_h - T_i} = \frac{2b_2 T_0}{b_1 + b_2} \sum_{n=0}^{\infty} \left(\frac{b_1 - b_2}{b_1 + b_2} \right)^n \text{erfc} \left(\frac{(2n+1)l_1}{2\sqrt{k_1 t}} \right), \tag{8}$$

where T_i and T_h are the initial temperatures of the shell mold and the hot station, respectively, $\tilde{T}$ is dimensionless temperature, $b = \sqrt{k \rho c_p}$ is an heat penetration coefficient, k is thermal conductivity, ρ is density, and c_p is heat capacity. In real cases, the thermal contact resistance plays an important role in affecting the actual heating response. The boundary condition with the consideration of thermal contact resistance changes to:

$$k_1 \frac{\partial T_1}{\partial x} = k_2 \frac{\partial T_2}{\partial x} = h(T_2 - T_1), x = 0, \ t > 0, \tag{9}$$

where h is the interfacial thermal conductance. With Eq. (9) as the boundary condition at the interface, an analytical solution is difficult to obtain. Instead, simple finite difference techniques were used to numerically solve the problem.

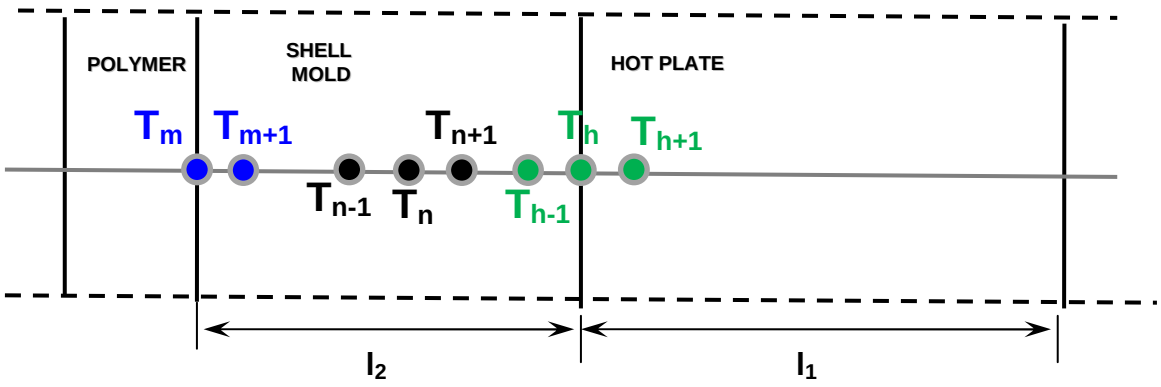

Figure 57: One-dimensional heat transfer model for two-station embossing.

A one-dimensional heat transfer model is shown in Fig.57. The dashed lines are lines of symmetry. The subscripts 1 and 2 are used to denote the thicknesses of the shell layer and the hot plate, respectively. This convention is used for other parameters. Thus, l_2, k_2, ρ_2, c_2 denote the thickness, thermal conductivity, density and specific heat of the heating layer, respectively. m,m+1…n-1,n,n+1…and h-1,h,h+1… are node indices. Depending on the boundary conditions and interface conditions, the finite difference formulas for the three layers are given as follows:

Surface node

$$T_m^{i+1} = T_m^i\left[1-2F_0\right]+2F_0T_m^i \tag{10}$$

Internal node

$$T_n^{i+1} = (1-2F_0)T_n^i + F_0\left[T_{n+1}^i - T_{n-1}^i\right] \tag{11}$$

Interface node

$$T_h^{i+1} = \frac{h\Delta t(T_{h-1}^i - T_{h+1}^i)}{\Delta x}\left[\frac{k_1}{\rho_1 c_1}+\frac{k_2}{\rho_2 c_2}\right] + T_h^i\left[1-\frac{2\Delta t}{\Delta x^2}\right]\left[\frac{k_1}{\rho_1 c_1}+\frac{k_2}{\rho_2 c_2}\right] \tag{12}$$

where the subscript of T denotes the node indices as shown in Fig.57; i denotes time step indices; Δx denotes the mesh size; $F_0 = \frac{k\Delta t}{\rho c \Delta x^2}$ is the mesh Fourier number; Δt is the time step. Since the three equations are in explicit form, the stability criterion $F_0 \leq 0.5$ must be satisfied for all materials. The same numerical procedure was previously used by Yao and Kim [53] for obtaining solutions for multilayer injection molds.

After a dwell time elapses, the hot base is removed and the cold base is placed against the stamp. The governing equations and boundary conditions are the same as in the heating stage, i.e., Eqs. (4), (5) and (9). However, the temperature distribution in the shell mold at the moment of switchover needs to be used as the starting temperature. The model provided above is under the assumption of thin slabs. In some practical cases, the size of the surface features or the spatial variation of the thickness of the shell mold could be large as compared with the shell thickness. In these cases, a full 3-D heat conduction analysis would be needed.

The thermal properties of the materials used in the simulation are listed in Table 1. The material used for both hot and cold stations is stainless steel. Two materials, aluminum and stainless steel, were used as the material for shell molds and the results were compared. The thickness of both hot and cold stations was maintained constant at 25°C while the shell thickness was varied. To verify the correctness of the finite difference code, a particular case with a 1-mm-thick aluminum shell and zero contact resistance (i.e. infinite thermal conductance at the interface) was performed and the numerical result was compared with the analytical solution (i.e. Eq. (8)). The error between the numerical result and the analytical result is negligible (below 1%).

Table 1: Thermal properties used in heat conduction simulation.

	ρ (Kg/m^3)	c_p (J/kg-K)	K (W/m-°K)
Aluminum	2700	900	237
Steel	7800	460	25

4.3.1 Heating Response

Fig.58 shows the surface thermal response of a 1.4-mm-thick aluminum shell in contact with the stainless steel hot station. The temperature is plotted in a dimensionless form, as defined by Eq. (8). The thermal response is affected overwhelmingly by the thermal conductance, h, at the interface between the shell and the hot station. A perfect contact at the interface is represented by $h = \infty$, while a fully insulated surface pair is represented by $h = 0$. As expected, the higher the interfacial conductance, the faster the heating rate at the shell surface results. For example, to reach a temperature of $\tilde{T}_s(t) = 0.8$, it only takes 1 s for a perfect contact, but takes more than 3 s for $h = 3000$ W/m2-K. The interfacial conductance in nature depends on the surface conditions and the two materials of the mating pair, as well as the pressure applied at the interface, thus needing to be experimentally determined on a case-by-case basis. The simulation results were thus compared with the experimental thermal response and the interfacial conductance corresponding to the best fit was determined to be 3000 W/m^2-K. This value is close to the data reported in the literature on stainless steel-aluminum contact, typically ranging from 3000 to 4500 W/m^2-K [55]. Using the dimensionless data in Fig.58, one can predict the temperature rise at the shell surface under a specific process condition. For example, it is predicted that the shell surface will be heated from room temperature to 200°C in 2.9 s if the hot station temperature is set to 250°C. This heating rate is fast enough to impact greatly on the thermal history of the polymer during thermoplastic processing, thus improving the part quality.

4.3.2 Effect of Shell Thickness

Fig.59 shows the effect of the shell thickness on the surface thermal response. The shell material is aluminum and the interfacial conductance is set to 3000 W/m^2-K. A classical way of accommodating the dimensional effect in heat conduction problems is to normalize the time with the square of the dimension. For multilayer systems with perfect

thermal contacts at interfaces, the plot of temperature versus normalized time results in a master curve [50]. This is owing to the scaling nature of the heat diffusion problem. For example, the cooling time for a slab will become four times as large if the thickness doubles [56]. However, for the present problem with thermal contact resistance involved, this master-curve plotting method does not work, as shown in Fig.60a. To accommodate the effect of an imperfect contact, a normalized interfacial conductance may be introduced with which Eq. (4), (5) and (9) can be rewritten into:

$$\frac{\partial^2 \tilde{T}_1}{\partial \tilde{x}^2} - \frac{1}{\alpha_1}\frac{\partial \tilde{T}_1}{\partial \tilde{t}} = 0 \text{, for } -1 < \tilde{x} < 0,\ \tilde{t} > 0, \tag{13}$$

$$\frac{\partial^2 \tilde{T}_2}{\partial \tilde{x}^2} - \frac{1}{\alpha_2}\frac{\partial \tilde{T}_2}{\partial \tilde{t}} = 0 \text{, for } 0 < \tilde{x} < l_2 / l_1,\ \tilde{t} > 0, \tag{14}$$

$$k_1 \frac{\partial \tilde{T}_1}{\partial \tilde{x}} = k_2 \frac{\partial \tilde{T}_2}{\partial \tilde{x}} = \tilde{h}(\tilde{T}_2 - \tilde{T}_1) \text{, for } \tilde{x} = 0,\ \tilde{t} > 0, \tag{15}$$

where $\tilde{x} = x/l_1$, $\tilde{t} = t/l_1^2$, and $\tilde{h} = hl_1$. The above equation states that for the same $\tilde{x}$, $\tilde{t}$ and $\tilde{h}$, the same $\tilde{T}$ will result. This works for the present problem and a master plot can be constructed, as shown in Fig.60b. For the master curve, $\tilde{h}$ is maintained constant at 3 W/m-K for all thicknesses. The corresponding h values are 6000, 3000 and 1500 W/m^2-K, respectively for thicknesses of 0.5 mm, 1 mm and 2 mm. From this master curve, one can predict that the surface heating rate will become four times as fast when the shell thickness doubles and the interfacial conductance reduces by a half. Another way to put it is that, for a constant interfacial conductance, the heating response will be less than four times as fast if the shell thickness is reduced by a half.

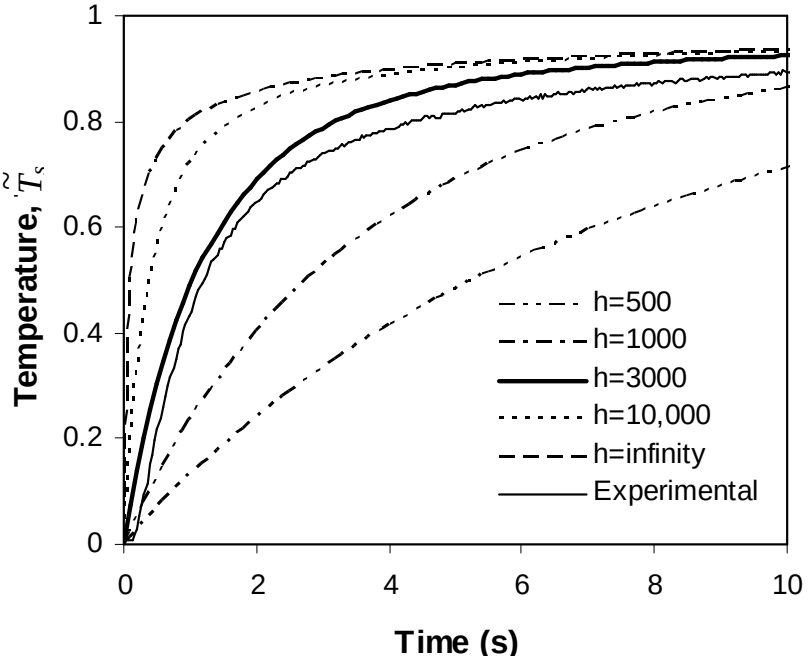

Figure 58: Predicted surface thermal response of a 1.4-mm-thick aluminum shell in contact with a stainless steel hot station. The dimensionless temperature, $\tilde{T}_s$, is defined as $\tilde{T}_s(t) = [T_s(t) - T_i]/(T_h - T_i)$, where T_i and T_h are the initial temperatures of the shell mold and the hot station, respectively. The interfacial conductance, *h*, varies from 500 W/m^2-K to infinity. An experimental thermal response with an aluminum shell at the same thickness is included for comparison. The simulation result agrees well with the experimental one with $h \approx 3000$ W/m^2-K.

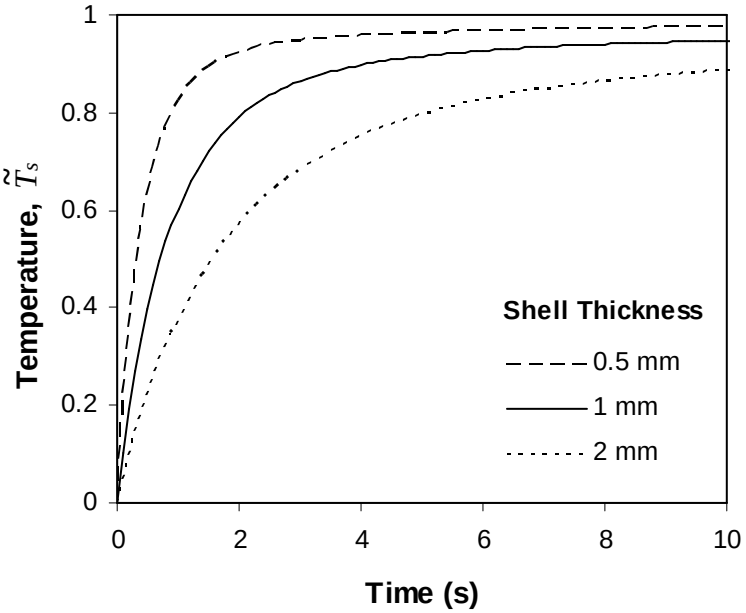

Figure 59: Predicted effect of shell thickness on the surface thermal response. The materials for the shell and the hot station are aluminum and stainless steel, respectively. the interfacial conductance is set to 3000 W/m^2-K.

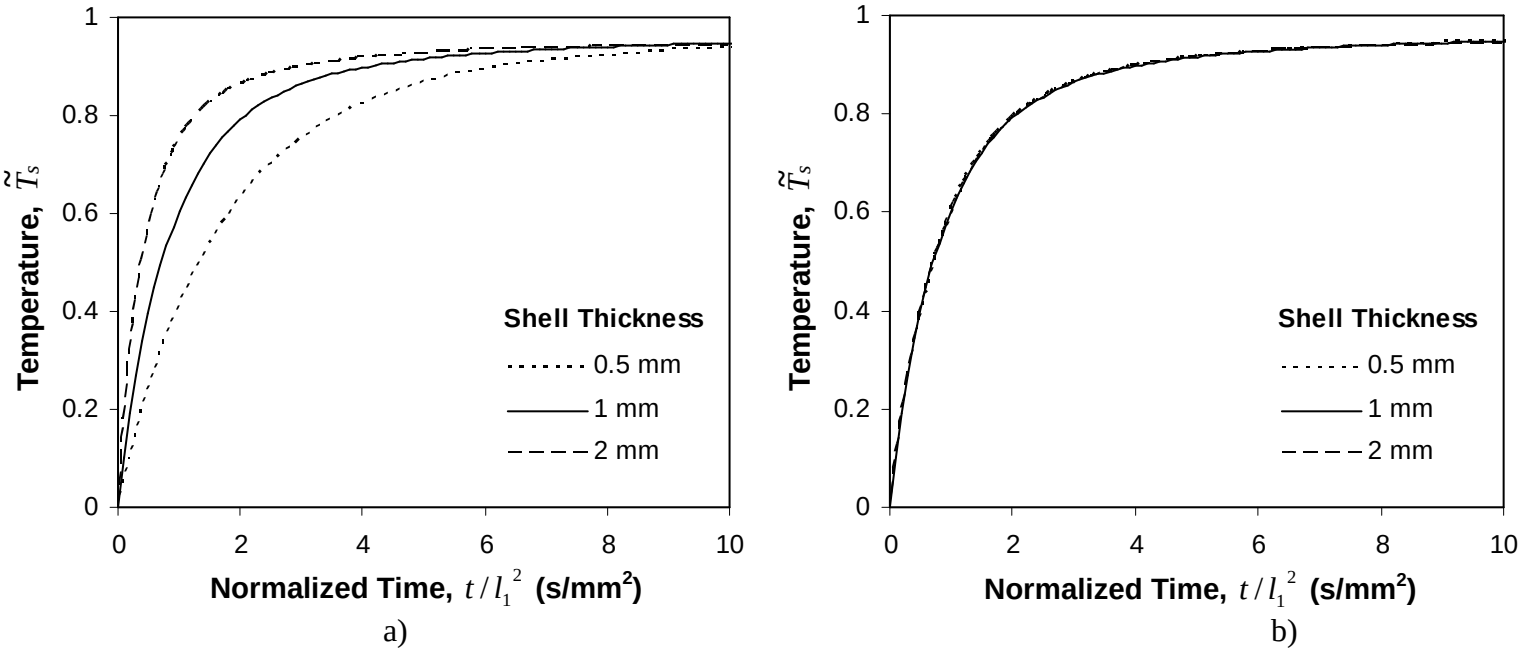

Figure 60: Predicted effect of shell thickness on the surface thermal response: a) normalized plot with constant interfacial conductance; and b) master plot with adjusted interfacial conductance. The materials for the shell and the hot station are aluminum and stainless steel, respectively. In a), the interfacial conductance is set to 3000 W/m^2-K and b) The interfacial conductance is 6000, 3000, 1500 W/m^2-K, respectively for shell thicknesses of 0.5 mm, 1 mm and 2 m.

4.3.3 Effect of Shell Material

Simulations were also conducted using stainless steel as the shell material. Fig.61 shows the predicted surface thermal responses of stainless steel shells with varied thickness in contact with the stainless steel hot station. The interfacial conductance is 2500 W/m-K. Again, it was determined by comparing the experimental thermal response with simulated ones with varied interfacial conductance. This value of interfacial conductance agrees with the typical values of stainless steel to stainless steel contacts, ranging from 1700 to 3700 W/m^2-K reported in the literature [55]. As expected, the steel shell is heated at a slower rate compared with the aluminum shell given the same thickness and similar interfacial conductance. For example, to reach $\tilde{T}_s$ of 0.8, it takes about 4 s for the 1-mm-thick steel shell while only taking 2 s for the aluminum shell with the same thickness. This can be justified by the large difference (14 times) in thermal diffusivity between the two materials.

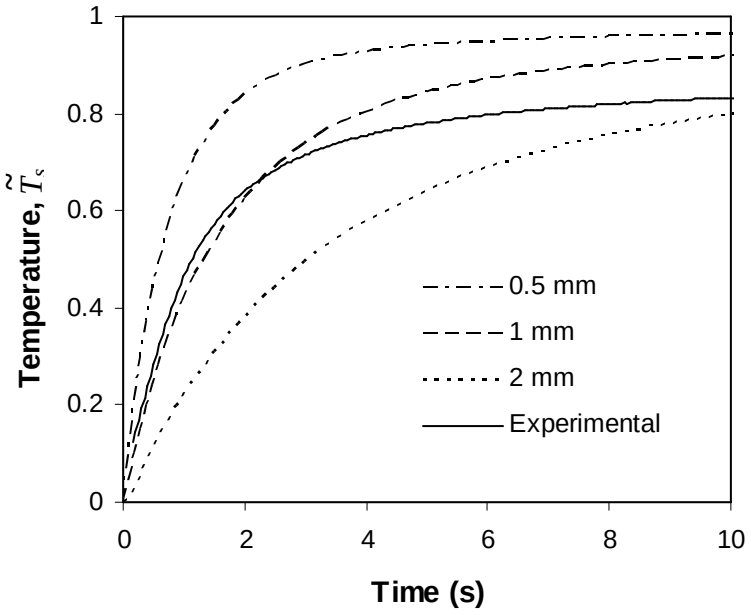

Figure 61: Predicted surface thermal response of stainless steel shells with varied thickness in contact with a stainless steel hot station. The interfacial conductance is set to 2500 W/m^2-K. An experimental thermal response with a 1-mm-thick stainless steel shell is included for comparison.

4.3.4 Thermal Cycling

Fig.62 shows heating and cooling responses during thermal cycling of a 1.4-mm-thick aluminum shell. The interfacial thermal conductance is set to 3000 W/m^2-K. Thermal responses with different heating times are compared. Based on the dimensionless thermal response, the thermal response of the shell for a given set of hot station and cold station temperature can be predicted. For example, given a hot station temperature of 250°C and a cold station temperature of 25°C, the shell can be heated from 25°C to 180°C in 2 s and then cooled to 50°C in a total cycle time less than 6 s. If the hot station temperature is raised to 350°C, the shell will be heated to 250°C in 2 s and then cooled to 50°C in a total cycle time less than 8 s. This fast heating and cooling response is comparable with the typical cycle times used in volume production of thermoplastic articles (e.g. thermoforming, injection molding, blow molding, etc.). Further, because the cooling stage is decoupled from the heating stage, the cooling response is faster than the multilayer system previously reported with similar heating layer thickness [51].

In the systems previously reported, the generated heat during the heating stage will sink to the mold base, thus lengthening the cooling stage subsequently. With the present method, this limitation is completely eliminated. Fig.63 shows the comparison between the numerical simulation and the actual experiments. From the numerical result, it is seen that cooling from the heated temperature to 50°C should take about 5 s. In contrast, the experimental results showed that, excluding the time spent on switchover, it took about 10 s for the shell to cool to 50°C from the heated temperature. The somewhat slower cooling response in the actual experiment can be explained. In the experimental setup, a 3-mm-thick Teflon sheet was used as a backup material for the thermocouple and it could be significantly heated during the 5 s heating stage, thus slowing down the cooling process.

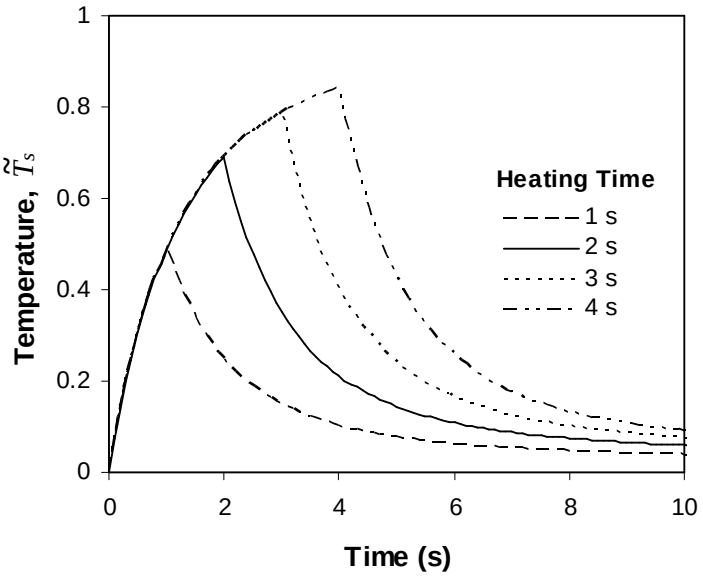

Figure 62: Predicted heating and cooling response during thermal cycling of a 1.4-mm-thick aluminum shell. The interfacial thermal conductance is set to 3000 W/m^2-K. Thermal responses with different heating times are compared.

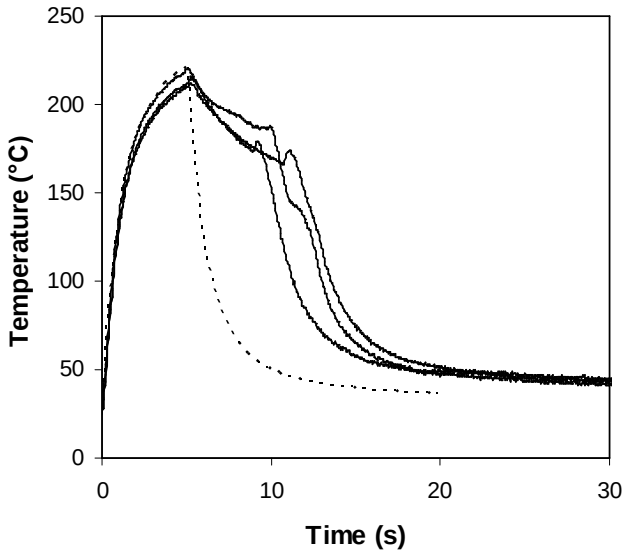

Figure 63: Experimental heating response of a 1.4-mm-thick aluminum shell in contact with a stainless steel hot station at 250°C. Predicted heating response from numerical simulation with an interfacial thermal conductance of 3000 W/m^2-K is given for comparison purposes.

4.4 Rheological Studies on ABS

Dynamic mechanical analyzer (DMA) and parallel plate rheometry were used to measure the rheological properties of ABS. ABS sheets were cut into discs with a diameter of 25.4 mm and a thickness of 0.9 mm for parallel plate rheometry and square films of 2.5×2.5×0.6 mm for DMA. The parallel plate rheometry was used for rheological measurements between 140°C to 200°C. The linear viscoelastic spectra in this temperature range were determined through small-strain oscillatory shear experiments from 10^{-2} to 10^{2} s^{-1}. The gap thickness on the parallel plate rheometer was maintained at 0.9 mm. A strain of 0.25% corresponding to the linear viscoelastic region was selected for these dynamic tests. The Viscosity of ABS at lower temperature near Tg (105°C) was measured using DMA in shear mode. A strain amplitude of 5 μm corresponding to the LVE was maintained during the test. The same frequency range as in parallel plate rheometry was used in DMA.

The complex viscosity η* obtained from DMA and parallel plate rheometer is a function of frequency ω. Using the Cox-Metz rule, which states that the shear rate dependence of the steady state viscosity η is equal to the frequency dependence of linear viscoelastic viscosity η*; the steady state viscosity is written as ,

$$\eta(\dot{\gamma}) = \eta'(\omega)\left[1+\left(\frac{\eta''}{\eta'}\right)^{2}\right]^{0.5}\Bigg|_{\omega=\dot{\gamma}} \tag{16}$$

where $\eta(\dot{\gamma})$ represents the steady-state viscosity, and $\dot{\gamma}$, ω, η' and η'' denote the shear rate, frequency , the dynamic viscosity and the elastic component of the complex viscosity, respectively. Fig. 64 shows the steady-state viscosity as a function of shear rate.

The temperature dependent viscosity was defined using Williams-Landel Ferry (WLF) equation,

$$\log a_T = \frac{-C_1(T - T_{ref})}{C_2 + (T - T_{ref})} \tag{17}$$

$$\frac{1}{\log a_T} = \frac{C_2 + (T - T_{ref})}{-C_1(T - T_{ref})} \tag{18}$$

$$\frac{1}{\log a_T} = \frac{C_2}{-C_1(T - T_{ref})} + \frac{1}{-C_1} \tag{19}$$

where C_1 and C_2 are model parameters, and T_{ref} is reference temperature. 105 ° C was set as the reference temperature. The value of the model parameters C_1 = 11.46 and C_2 = 85.14 were obtained by plotting 1/log a_T versus 1/(T-T_{ref}), as shown in Fig.65. The shift factor from the WLF equation is plotted against the experimental data for comparison. There is considerably a good fit between the both, as shown in Fig.66.

4.5 Modeling of Polymer Flow during Embossing

The basic elements in a polymer processing model include: 1) conservation equations, 2) constitutive equations, 3) discretized geometry, 4) boundary conditions and initial conditions, and 5) a numerical implementation procedure. These elements are equally applicable to two-station embossing simulation. The two-station embossing process is characterized by 3-D deformation under a highly non-isothermal environment. It is noted that commercially available codes for compression molding simulation (e.g. the injection-compression module in Moldflow® are typically based on a 2.5-D Hele-Shaw flow model [54-55], and thus cannot correctly describe the deformation process in two-station embossing.

The part geometry used in the simulation is the microlens array. Considering the periodicity of the lens array, only one lens is needed in the model. The axisymmetric interpretation of the geometry results in a planar model, as shown in Fig.67. Because large deformation occurs during the embossing stage (that is, velocity and stress dominate the process), the effect of the polymer compressibility on the momentum equation may be neglected.

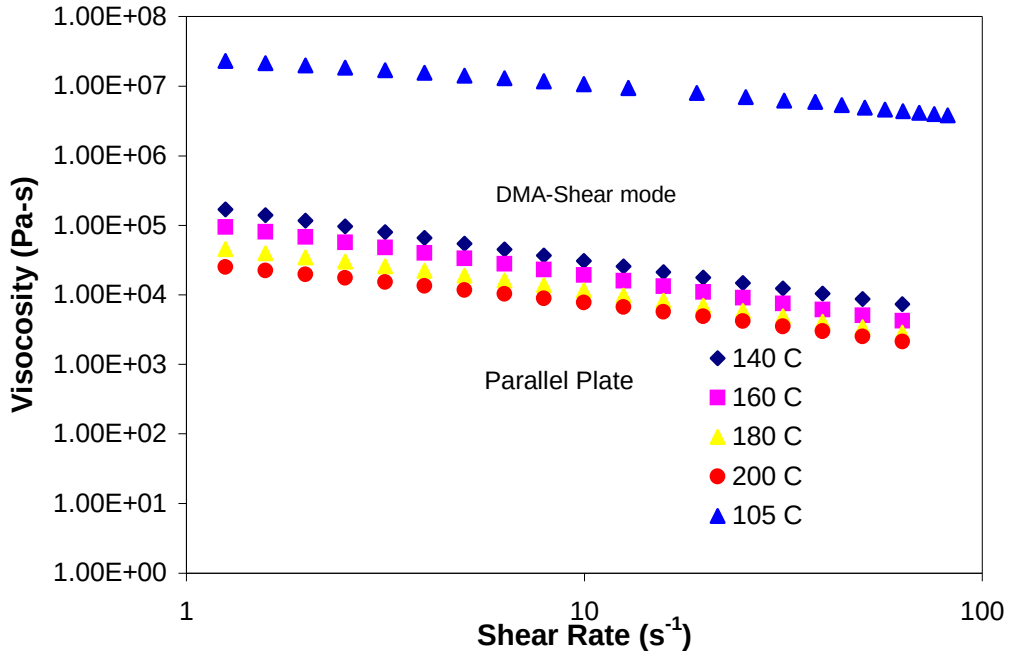

Figure 64: Viscosity data obtained from DMA and parallel plate rheometry.

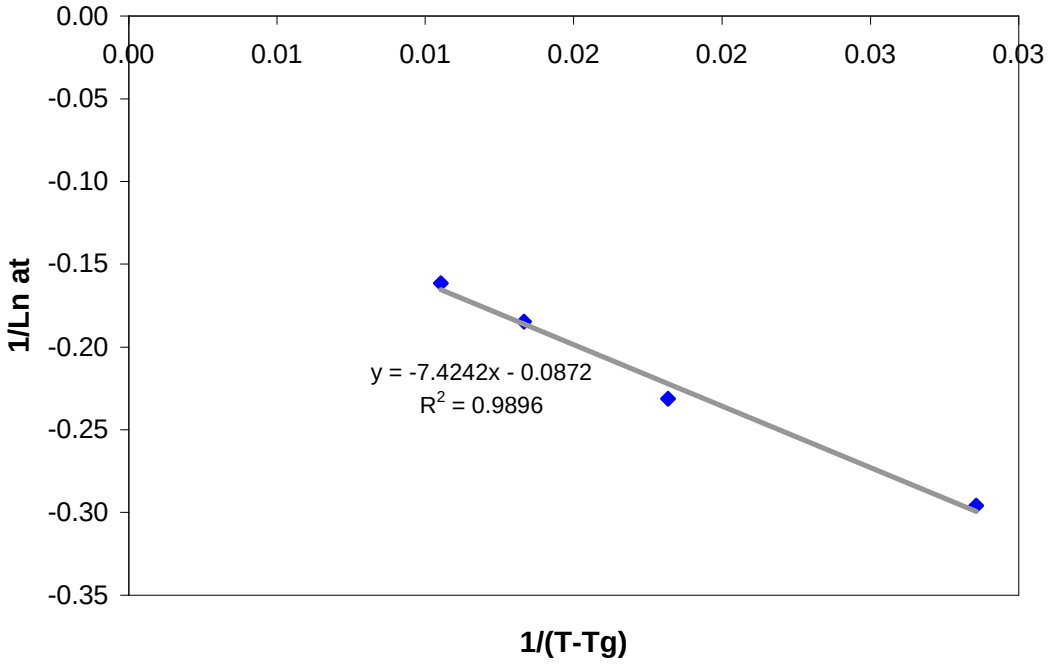

Figure 65: Calculation of WLF constants.

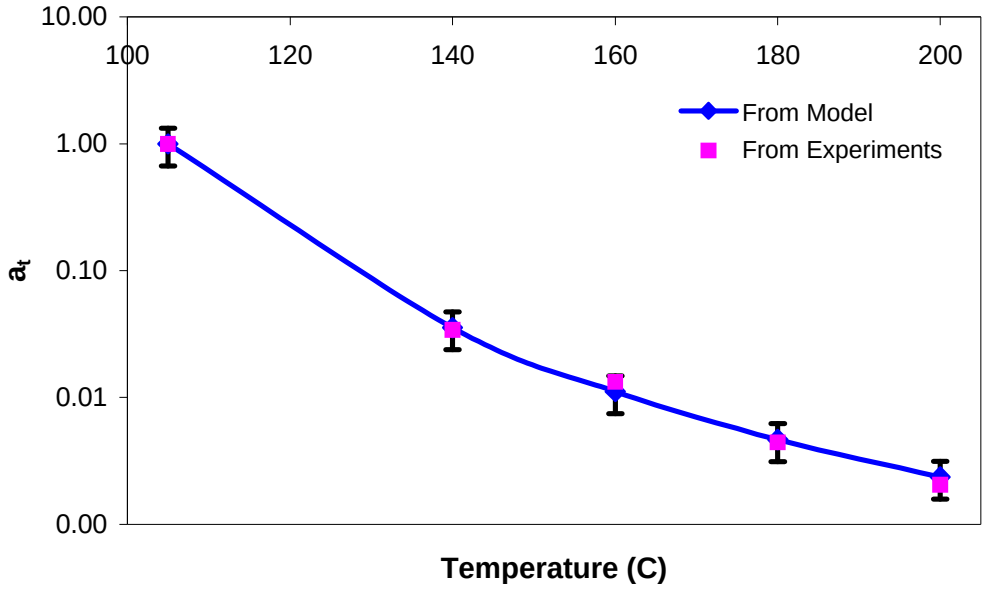

Figure 66: Predicted shift factor from model compared to experimental results.

As compared with the high viscosity of the polymer deformed in a small geometry, the gravitational force may be safely disregarded. The resulting simplified conservation equations in the axisymmetric case are:

mass conservation

$$0 = \frac{1}{r}\frac{\partial(rv_r)}{\partial r} + \frac{\partial(v_z)}{\partial z} \tag{20}$$

momentum conservation

$$\rho\begin{pmatrix} \frac{\partial v_r}{\partial t} + v_r\frac{\partial v_r}{\partial r} + v_z\frac{\partial v_r}{\partial z} \\ \frac{\partial v_z}{\partial t} + v_r\frac{\partial v_z}{\partial r} + v_z\frac{\partial v_z}{\partial z} \end{pmatrix} = -\begin{pmatrix} \frac{\partial P}{\partial r} \\ \frac{\partial P}{\partial z} \end{pmatrix} + \begin{pmatrix} \frac{1}{r}\frac{\partial}{\partial r}(r\tau_{rr}) + \frac{\partial \tau_{zr}}{\partial z} \\ \frac{1}{r}\frac{\partial}{\partial r}(r\tau_{rz}) + \frac{\partial \tau_{zz}}{\partial z} \end{pmatrix} \tag{21}$$

and energy conservation

$$\rho c_p\left(\frac{\partial T}{\partial t} + v_r\frac{\partial T}{\partial r} + v_z\frac{\partial T}{\partial z}\right) = \frac{1}{r}\frac{\partial}{\partial r}\left(rk\frac{\partial T}{\partial r}\right) + \frac{\partial}{\partial z}\left(k\frac{\partial T}{\partial z}\right) + \frac{\alpha}{2}\underline{\underline{\tau}} : \underline{\underline{\dot{\gamma}}}, \tag{22}$$

where r and z are the radial and axial coordinates, v is velocity, P is equivalent pressure, $\underline{\underline{\tau}}$ is deviatoric stress tensor, $\underline{\underline{\dot{\gamma}}}$ is strain tensor, and α denotes the faction of mechanical work converted into heat. For a purely viscous liquid, α is equal to 1.

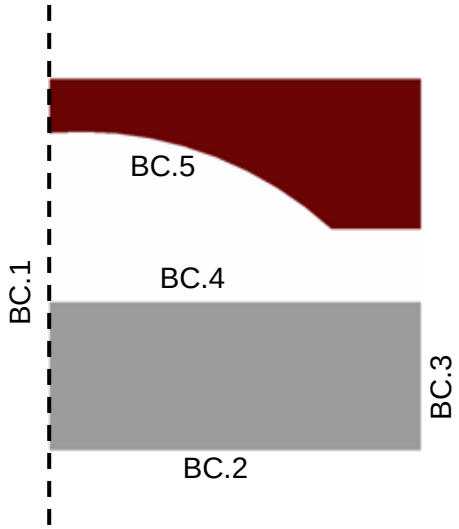

Figure 67: Geometry and boundary conditions used in microlens embossing simulation. The flow boundary conditions are: BC.1 (axisymmetry), BC.2 (fn = -p and fs = 0, where fn is normal stress, fs is tangential stress and p is the embossing pressure), BC.3 (periodic symmetry), BC.4 (free surface with contact detection), and BC.5 (mold surface to be contacted). The thermal boundary conditions are: BC.1, BC.2, and BC.3 (zero heat flux), BC.4 (zero heat flux before contact but convective after contact is detected), and BC.5 (time-dependent mold temperature). After contact is detected on BC.4, the convective heat transfer coefficient is equal to the thermal contact conductance between the polymer and the metal mold.

The polymer (ABS) is considered viscous above its glass temperature (Tg). Below T_g an infinitely high viscosity is applied and hence deformation is suppressed. Because of the compression molding nature of the embossing process, the strain rate is typically much lower than that in injection molding, and thus the strain rate dependence on the viscosity may be neglected. As a result, the constitutive equation for the stress tensor can be written as:

$$\underline{\underline{\tau}} = \eta(T) \cdot \underline{\underline{\dot{\gamma}}}, \tag{23}$$

where

$$\eta(T) = \eta(T_g) \cdot \exp\left[-\frac{C_1(T - T_g)}{C_2 + T - T_g} \right]. \quad (24)$$

The representative material parameters for ABS were chosen for the embossing simulation, as listed in Table 2.

Table 2: Representative material properties for ABS.

ρ, Kg/m^3	c_p, J/Kg-K	k, W/m-K	T_g, ºC	$\eta(T_g)$, Pa-s	C_1	C_2
1260	2000	0.5	105	4.68×10^7	11.46	85.14

The boundary conditions are shown in Fig.67. The flow boundary conditions are: BC.1 (axisymmetry), BC.2 (fn = -p and fs = 0, where fn is normal stress, fs is tangential stress and p is the embossing pressure), BC.3 (periodic symmetry), BC.4 (free surface with contact detection), and BC.5 (mold surface to be contacted).

The thermal boundary conditions are: BC.1, BC.2, and BC.3 (zero heat flux), BC.4 (zero heat flux before contact but convective after contact is detected), and BC.5 (time-dependent mold temperature). After contact is detected on BC.4, the convective heat transfer coefficient is equal to the thermal contact conductance between the polymer and the metal mold. The finite element method was used to solve the governing equations with the material properties and boundary conditions given above.

The values of the parameters in the boundary conditions and initial conditions were set up based on the experimental conditions. The embossing pressure was calculated to be 0.53 MPa based on the embossing force of 270 N and the stamp diameter of 25.4 mm. The initial temperature of the ABS sheet was 25ºC. The actual temperature response at the surface of the stamp (Fig.58) was used as the time dependent temperature on the boundary BC.5 (Fig.67). Simple scaling analysis [56-57] indicated that the heat diffusion

process dominates in the energy equation for cavity sizes in micrometers. In this case, the polymer temperature inside the small cavity tends to be spatially uniform. The actual heating rate of the polymer, however, is a strong function of the thermal contact conductance between the polymer and the cavity wall. Several studies [58-59] indicated that the typical thermal contact conductance at the polymer-mold interface is around 2500 W/m2-K. Therefore, this value of thermal contact conductance was applied on boundary BC.4.

Fig.68 shows the flow front movement during the embossing stage. There was a long induction time, more than 1.9 s, before any polymer started to move into the cavity. After the filling was triggered, it only took about 0.43 s for the polymer to completely fill the cavity. This filling behavior agrees very well with the experimental finding. In the experiments, it was found that the cavity was completely filled with a contact heating time of 3 s, but barely any protrusion was formed when a heating time of 2 s or below was used. During the entire embossing stage, the pressure acting on the boundary BC.2 was constant at 0.53 MPa. Therefore, the unique filling behavior, i.e., with a long induction time but a short filling time, is considered to be related to the thermal history of the polymer and the small size of the cavity. Previous studies [59-62] with micro injection molding and thin-wall molding showed that the mold temperature plays a significant role in influencing the filling process into micro geometries. In particular, Yao and Kim [62] showed that a mold temperature very close to the polymer softening temperature is needed in order for the micro filling process to occur. Once the filling process is initiated, it typically takes a very short period (i.e. a small faction of a second) for complete filling due to the small size of the microcavity. For the two-station embossing process investigated in this study, the polymer was not preheated, and therefore the mold temperature had to reach above the polymer softening temperature in order to initiate the cavity filling process. From Fig. 58, it is seen that it took less than 1 s for the stamp to reach above the T_g of ABS. However, because of the thermal contact

resistance at the polymer-stamp interface, the polymer is expected to be heated to a lower temperature. Further, the necessary temperature for the polymer to gain good fluidity for filling is expected to be significantly above the Tg. It is therefore useful to study the evolution of the thermal history for the polymer during the entire embossing stage.

Fig.69 shows as examples the temperature distributions in the polymer substrate at four different time instants. The temperatures of the polymer near the cavity for the four time instants, namely, 1.62 s, 1.9 s, 2.15 s, and 2.33 s, were 114, 129, 144, and 158ºC. Because of the effect of the thermal contact resistance at the polymer-stamp interface, the polymer temperature was considerably lower than that of the stamp for a given time instant. The respective temperatures of the stamp at the four time instants were 156, 166, 172, and 182ºC. When the filling process was initiated at 1.9 s, the polymer has already been heated to about 24°C above the T_g. The corresponding viscosity at this temperature is around 3,470,000 Pa-s.

Fig.70 shows the distributions of deformation related quantities including pressure, strain rate and velocity vector during the cavity filling stage (at 2.09 s). It can be seen that cavity filling occurred at relatively low pressure and strain rate. The pressure was lower than 1.86 MPa and the equivalent strain rate was smaller than 0.58 s^{-1}. These values are orders of magnitudes lower than those in injection molding. The pressure and strain-rate dependency on the viscosity can thus be safely dropped in the simulation. This justifies the use of a pressure and strain rate independent viscosity in the two-station embossing simulation in this study. The velocity vector distribution in Fig 70 illustrates how the polymer flowed during cavity filling. In this case, the polymer undergoes squeeze flow phenomenon as explained in earlier studies. [56]. For cavities with a size below a hundred micrometers, a uniform temperature field near the cavity is expected to be reached easily as shown in Fig.68 and the previous study. Thus uniform and controllable flow pattern can be achieved in two-station embossing of microcavities even using a polymer without preheating. However, the non-isothermal nature with a non-

preheated polymer substrate will certainly increase the residual stress development and consequently the risky of poor dimensional stability and poor optical properties, which are among the critical concerns for precision optical elements such as diffractive optics. In these cases, possible remedies could include the employment of a thinner polymer substrate or preheating the sample before the embossing.

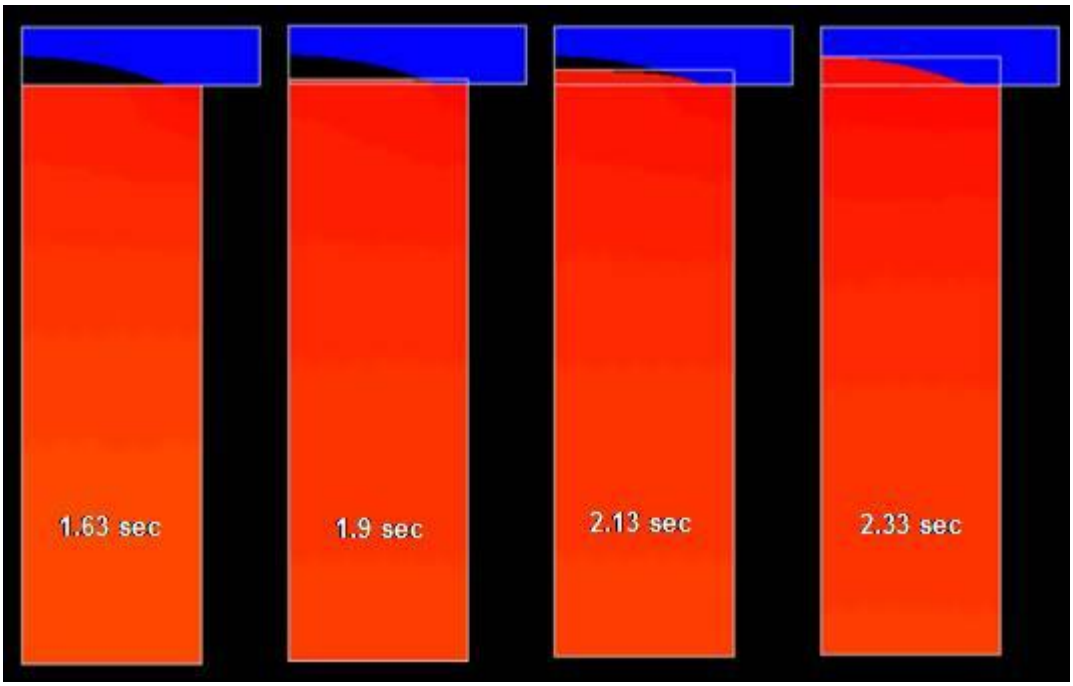

Figure 68: Filling pattern of ABS in the microlens cavity. Before 1.9 s, there was barely any polymer filled into the cavity. After the filling was triggered at 1.9 s, it only took 0.43 s for the polymer to completely fill the cavity.

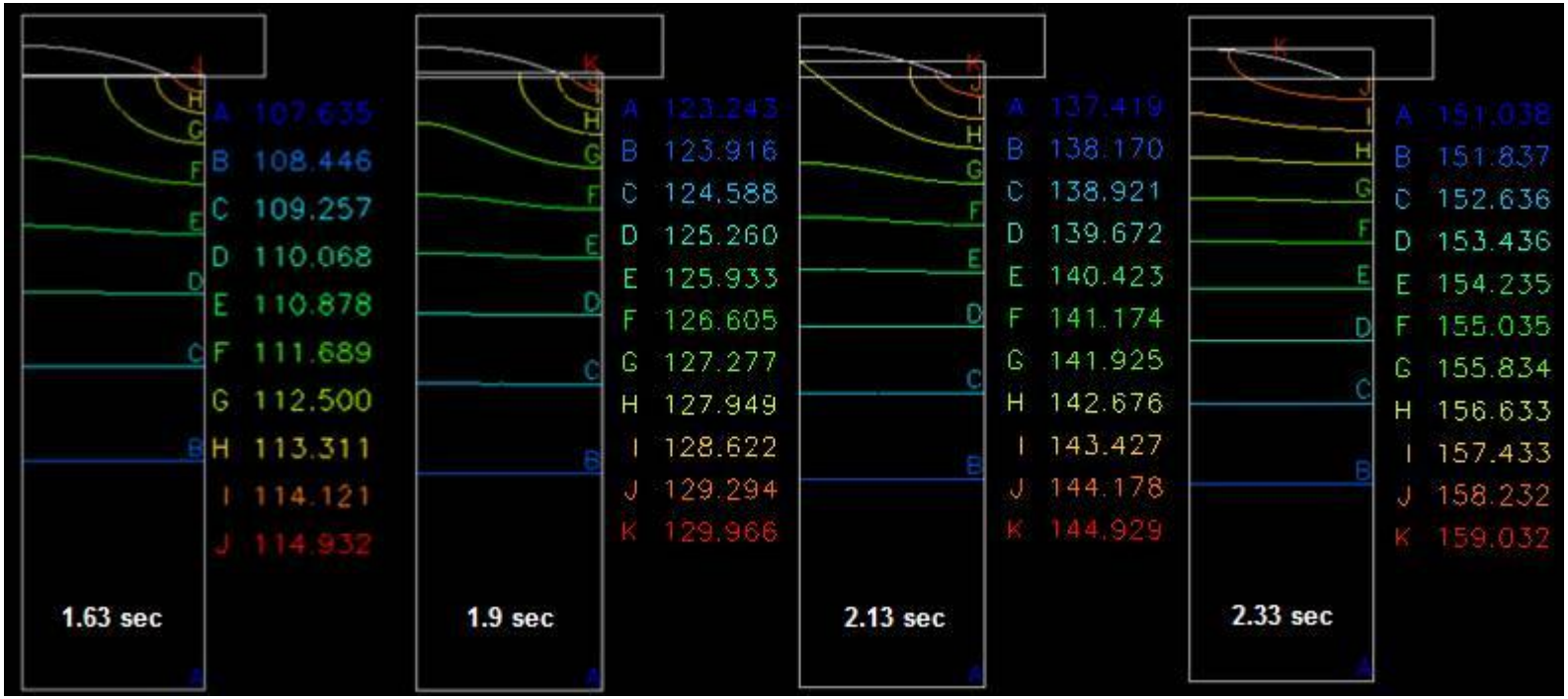

Figure 69: Temperature distribution at different time instants. The unit of temperature is degrees Celsius

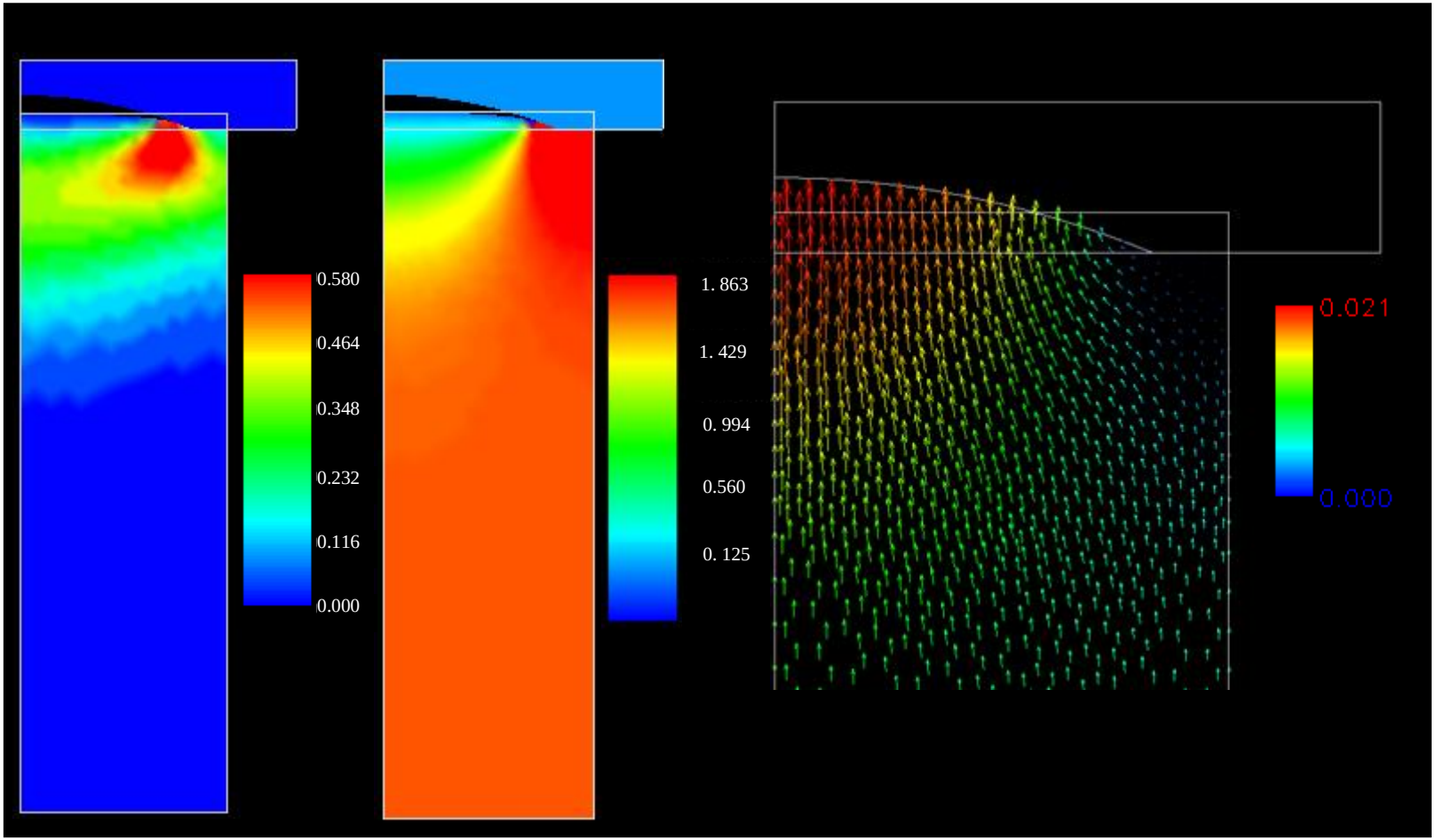

Figure 70: Distributions of strain rate (a), pressure (b), and velocity vector (c) at the end of 2.09 s

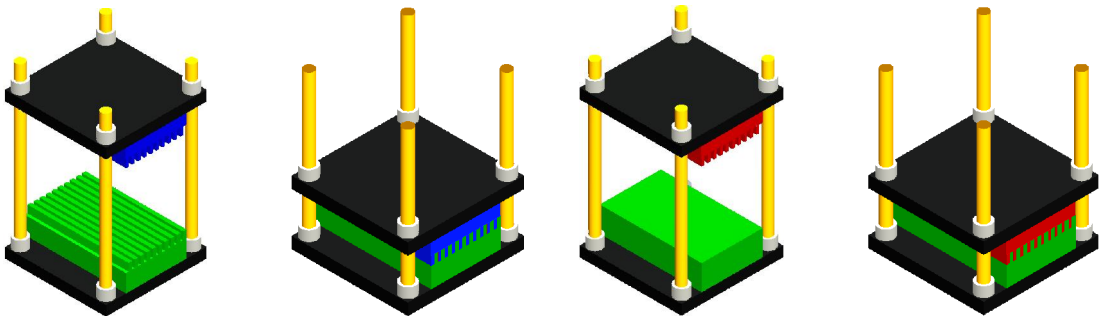

a) b) c) d)

Figure 71: Hot Embossing process involving several sequential stages: a) mold preheating, b) embossing c) cooling, and d) mold opening.

4.6 Model Validation

The polymer flow during the two station embossing process was modeled as a viscous creep flow as discussed in section 4.5. The validity of this model in embossing based processes was further examined using an experimentally simple flow case under an isothermal embossing condition. The geometry in this simple flow involved a circular disc with a center post. The predicted filling patterns were compared with those observed in the experiments.

4.6.1 Isothermal Embossing

A pneumatic press was modified and used as an embossing apparatus. The embossing process consists of a series of sequential operations, i.e., mold preheating, embossing, cooling, mold opening, and finally part ejection from the mold, as illustrated in Fig.71. Fig.72 shows the circular mold with a center post cavity of Ø 250 × 3.87 μm. Two-stainless steel plates of 76.2 × 76.2 × 25.4 mm acted as hot platens. The platens were heated by two 250 W cartridge heaters (Ø 6.35 mm in diameter) and cooled by circulating water through two Ø 6.34 mm channels machined along its length. Circular ABS sheets of Ø 12.7 × 1.6 mm were used as embossing substrates. The pneumatic press provided a constant embossing force of 1601 N.

The mold and the ABS discs were preheated in an oven at 180°C for 30 and 15 min, respectively, before embossing between the heated platens. The embossing was carried out using displacement control. Two precision machined shims of 0.65 mm and 0.75 mm were used to control polymer flow inside the mold cavity. At the end of the embossing stage, water was circulated through the platens and the part was ejected from the mold at room temperature.

Fig.73 shows the embossed posts. The average length of the post recorded over six trials for displacements of 0.15 mm and 0.25 mm were measured to be around 0.156 mm and 2.9 mm.

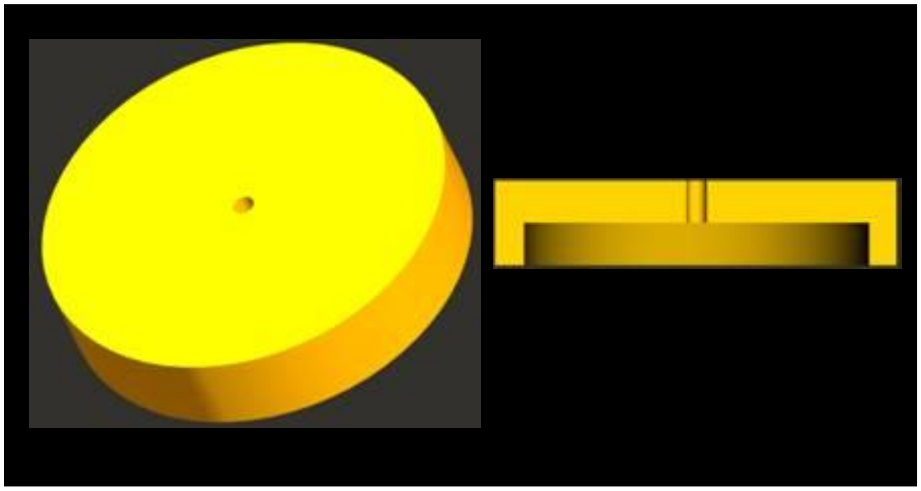

Figure 72: Circular mold with a center hole.

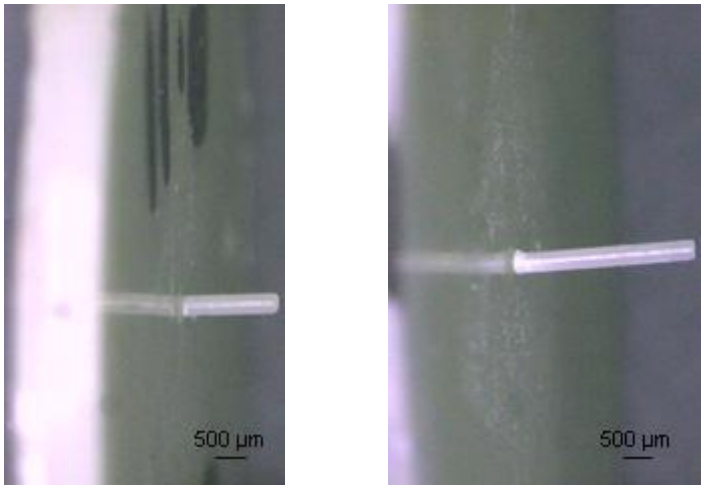

a) b)

Figure 73: Embossed posts: a) filled length for 0.15 mm displacement and b) filled length for 0.25 mm displacement.

4.6.2 Modeling of Isothermal Embossing

During isothermal embossing, the polymer is purely viscous. The inertia effect could be included but the gravitation effect is neglected. The embossed feature is a circular post and hence considering it as an axisymmetric geometry, the resulting conservation equations for isothermal embossing in 2-D can be written as**:**

$$0 = \frac{1}{r}\frac{\partial(rv_r)}{\partial r} + \frac{\partial(v_z)}{\partial z}, \tag{25}$$

$$\rho\begin{pmatrix} \frac{\partial v_r}{\partial t} + v_r\frac{\partial v_r}{\partial r} + v_z\frac{\partial v_r}{\partial z} \\ \frac{\partial v_z}{\partial t} + v_r\frac{\partial v_z}{\partial r} + v_z\frac{\partial v_z}{\partial z} \end{pmatrix} = -\begin{pmatrix} \frac{\partial P}{\partial r} \\ \frac{\partial P}{\partial z} \end{pmatrix} + \begin{pmatrix} \frac{1}{r}\frac{\partial}{\partial r}(r\tau_{rr}) + \frac{\partial \tau_{zr}}{\partial z} \\ \frac{1}{r}\frac{\partial}{\partial r}(r\tau_{rz}) + \frac{\partial \tau_{zz}}{\partial z} \end{pmatrix}. \tag{26}$$

The ABS viscosity measured at 180°C using a parallel plate rheometer shows shear thinning at low rates of 5 s^{-1}. Hence the stress tensor can be written as

$\underline{\underline{\tau}} = \eta(\underline{\underline{\dot{\gamma}}}) \cdot \underline{\underline{\dot{\gamma}}}$, where $\eta(\underline{\underline{\dot{\gamma}}})$ is the strain rate dependent viscosity.

The power-law constitutive equation is the most commonly used for accommodating shear thinning behavior in polymers. The power-law model is written as $\eta = m\dot{\gamma}^{n-1}$, where n-1 is the slope of $\log \eta$ vs $\log \dot{\gamma}$ and m is the consistency index. The viscosity of ABS at 180°C fitted using power law for n = 0.37 and m = 56208 is shown in Fig.74. Although the model perfectly predicts the shear rate dependency on the viscosity in the testing range of shear rate, the obvious disadvantage is that it fails to describe lower shear rate. Since n is usually less than one, η goes to infinity at lower shear rates, rather than a constant η_0. In order to predict the Newtonian region at lower shear rates, we fit the viscosity data using the Cross law, as shown in Fig.74. The Cross model is described by the following equation:

$$\eta = \frac{\eta_0}{1 + (\lambda \dot{\gamma})^s}, \tag{27}$$

where λ is the time for the onset of shear thinning, η_0 is the zero shear viscosity and $\dot{\gamma}$ is the shear rate. A best fit of the cross law for the ABS at 180 ° C was obtained with λ = 3.4, s = 0.85, and η_0 = 208000 Pa-s. The stress tensor can be written as

$$\underline{\underline{\tau}} = \frac{\eta_0}{1 + (\lambda \dot{\gamma})^s} \cdot \underline{\underline{\dot{\gamma}}}. \tag{28}$$

The boundary conditions are shown in Fig.75.The flow boundary conditions are: BC.1 (mold surface to be contacted), BC.2 (free surface with contact detection), BC.3 (free surface with contact detection), BC.4 (v_n=-v and f_s=0, where v_n is the normal velocity and f_s is the shear force), and BC.5 (axisymmetry symmetry). The finite element method was used to solve the governing equations with material properties and governing equation given above.

The values of parameters in the boundary condition were set based on experimental conditions. The normal velocity along the boundary BC4 was calculated to be 0.85 mm/s for a constant force of 1601 N along the same boundary. Fig.76 shows the flow front movement for corresponding displacements of 0.15 and 0.25 mm. The deformed polymer shows squeeze flow along the BC. 4 similar to that of the experiments. Comparison of the filling length of the mold cavity shows a considerably good match, as shown in Fig.77.

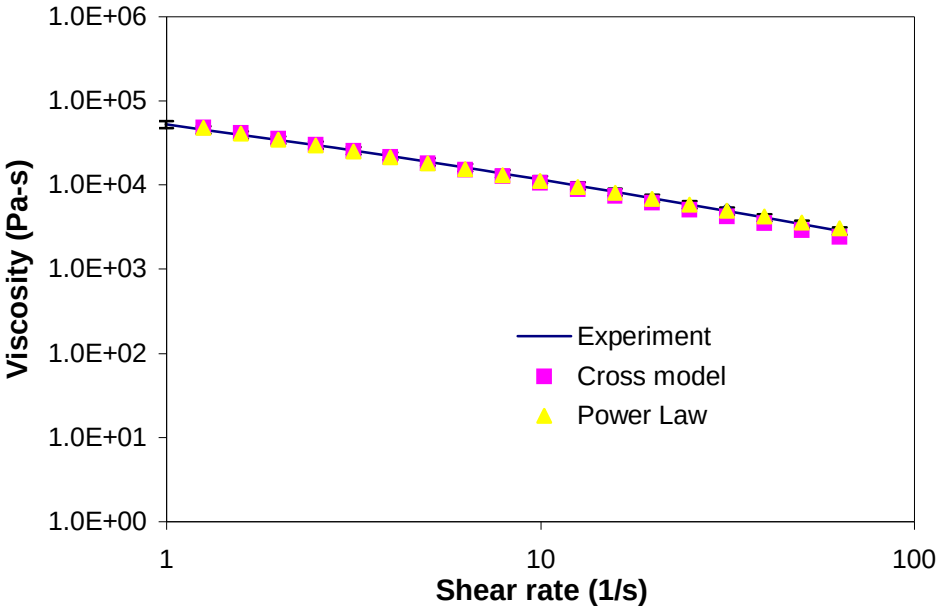

Figure 74: Comparison of viscosity and shear rate for power law model, Cross law model and experiments.

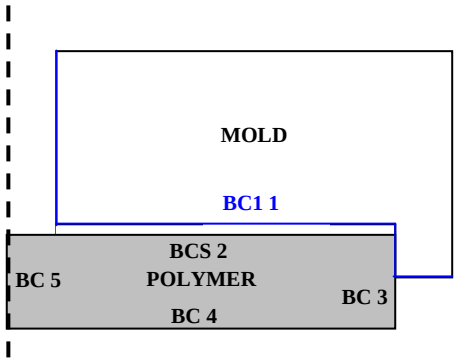

Figure 75: The flow boundary conditions are: BC.1 (mold surface to be contacted), BC.2 (free surface with contact detection), BC.3 (free surface with contact detection), BC.4 (v_n=-v and f_s=0, where v_n is the normal velocity and f_s is the shear force), and BC.5 (axisymmetry).

a)

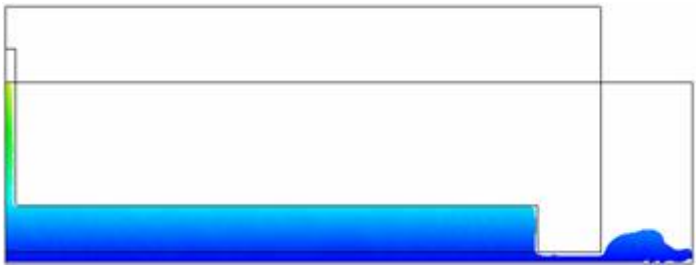

b)

Figure 76: Simulation results showing the flow front displacement: a) 0.15 mm displacement and b) 0.25mm displacement

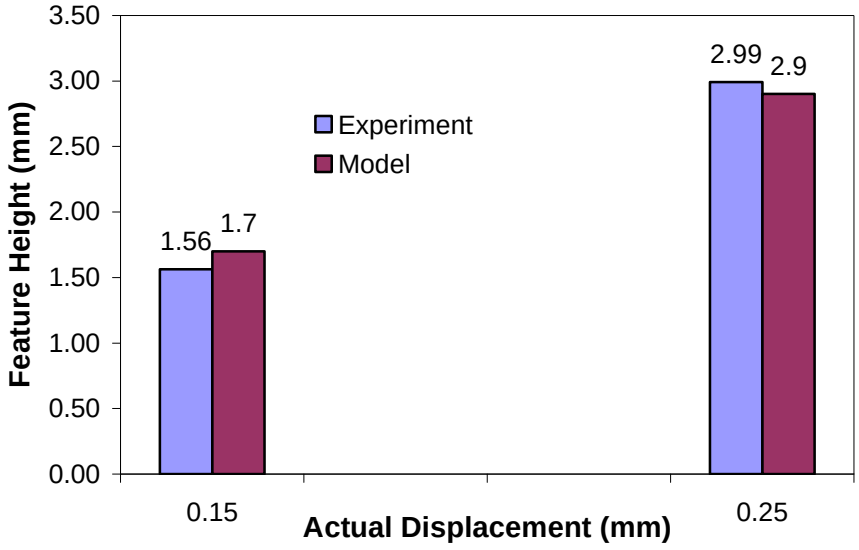

Figure 77: Comparison of experimental and simulation results

CHAPTER 5

THROUGH-THICKNESS EMBOSSING

5.1 Introduction

Hot embossing is essentially an open-die compression molding process. This open-die scheme allows fast and simple design and setup of the embossing tool and process. However, due to the open-die configuration, high embossing pressure is difficult to build up, particularly on thick polymer substrates, limiting the capability in embossing high aspect ratio features. For the same reason, 3-D discrete features/parts are difficult to emboss. At present, these discrete features/parts are mainly produced by microinjection molding. The molding results, however, are often compromised, because of the complex tool setup and the high amount of stresses introduced to the part during injection molding. As seen from the literature review in Chapter 2, only limited work has been conducted on the use of embossing-based approaches for patterning discrete features.

In this chapter, we report a hybrid punching and embossing process for fabrication of 3-D parts. The embossing tool includes a punching head and to-be-replicated features in the socket behind the punching head. The built-in punching head allows for a through-thickness action and provided a close-die environment for embossing pressure buildup. The method was used to successfully emboss 3-D multichannel waveguides (with geometry shown in Fig.78), which require uniform edges and accurate dimensions.

5.2 Embossing Mold Design and Fabrication

The hot-embossing mold for the waveguide was designed as an assembly of three mating pieces: a punching cutter, a shaper, and a disc spacer, as shown in Fig.79. A three-piece mold design was adopted to achieve 1) complete fill of the mold cavity during the

embossing process, 2) a mold with sharp edges and tight dimensional tolerances, 3) easy cleaning of residual polymers after embossing, and 4) evacuation of trapped air during the embossing process.

The critical component in the mold insert assembly is the shaper, which was designed as the negative pattern of the geometry to be embossed. Slots cut at the end of the 4 arms assist in the mating of the shaper with the holder. Close dimensional tolerances were employed during machining of the shaper, the shaper holder, and the disc spacer to prevent leakage of the polymeric material during the embossing process. The contour of the shaper was produced using micro electrical discharge machining with a 50 μm diameter wire. The shaper holder is necessary for aligning the shaper and providing open channels on the embossed part. The shaper holder and the punching cutter are a combined single component in the present design. The polymer blank is cut along the circumference of the circular cutter as the punching head move down during the embossing process. Full mating of the shaper and the shaper holder creates a cavity of 2-mm thickness below the shaper and is used to form the base of the waveguide during the embossing process. The disc spacer prevents the polymer leaking from the shaper holder during embossing. Standard hot embossing often uses vacuum to assist in complete fill of cavities. This, however, could result in more complicated mold designs. The use of vacuum during waveguide embossing was eliminated by employment of a small clearance on the order of 5 microns between the spacer and the shaper. This small clearance creates a path for the trapped air to escape. The assembled mold insert was fastened to a hot plate with heating and cooling elements embedded, as shown in Fig.80. A precision platen set was used to mount the two hot and cold plates, as shown in Fig.81. The hot plate was mounted to the top platen, the moving platen, and the cold plate to the bottom platen, the fixed platen. Thermal insulation composites were inserted between the plates and the platens.

5.3 Embossing Setup

A pneumatic press was modified and used as an embossing apparatus. The stationary platen of the platen set was fastened to the base of the pneumatic press by means of a lock screw. The moving platen was connected to the piston of the pneumatic press by means of a threaded stainless steel stud. The daylight opening between the mold and the base plate was set to 12.5 mm by adjusting the threaded stud connecting the platen and the piston. This was done to ensure that there was no contact between the mold and the polymer substrate prior to the embossing process. The stroke length of the piston was adjusted to achieve complete fill of the mold cavity and control of the cutter position during the embossing process. The stroke length of the piston can be adjusted by varying the position of the piston lock screws at the top of the cylinders. The optimum stroke length for the embossing process was calculated by trial and error.

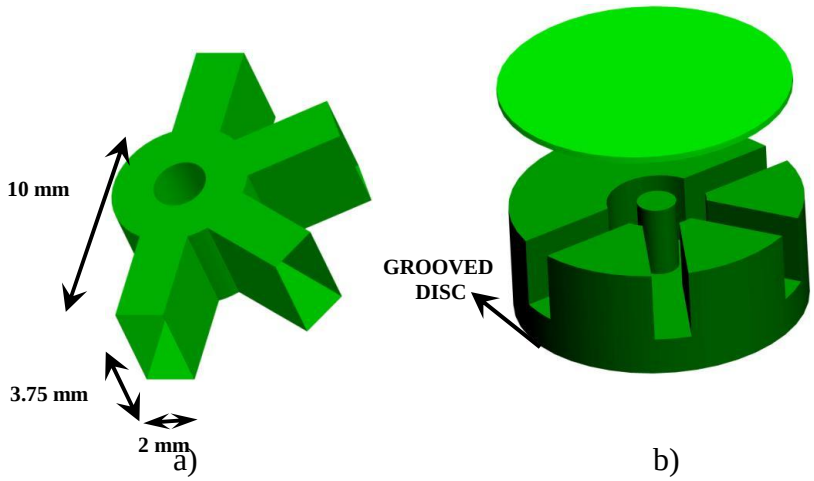

Figure 78: Multichannel millimeter waveguide design: a) original design and b) modified design for hot embossing.

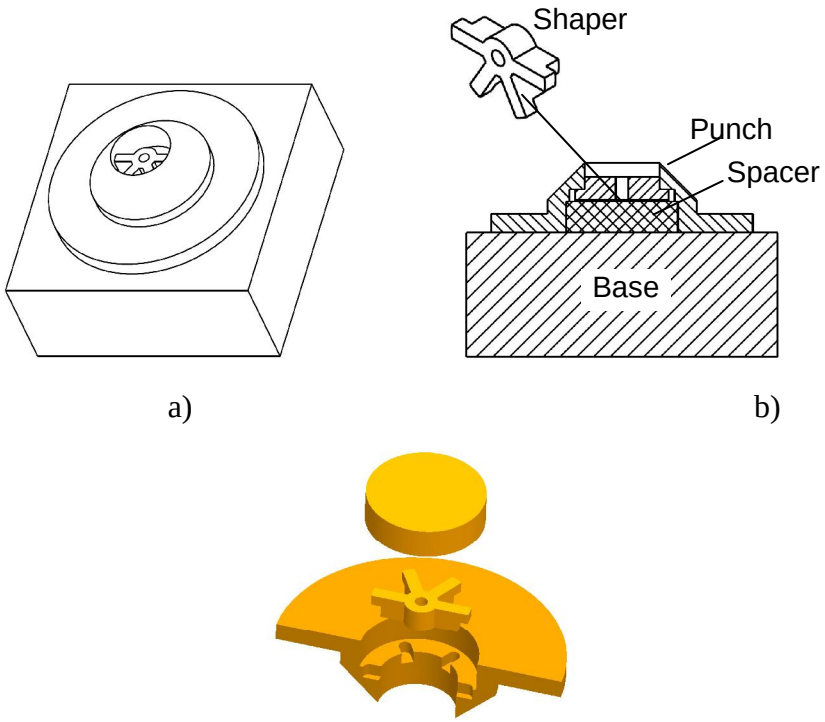

Figure 79: Design of the embossing tool for waveguide fabrication: a) assembled view, b) cross-sectional view, and c) exploded view.

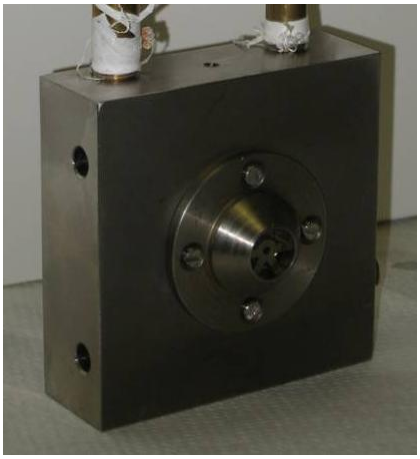

Figure 80: Mold insert assembly fastened to a hot plate.

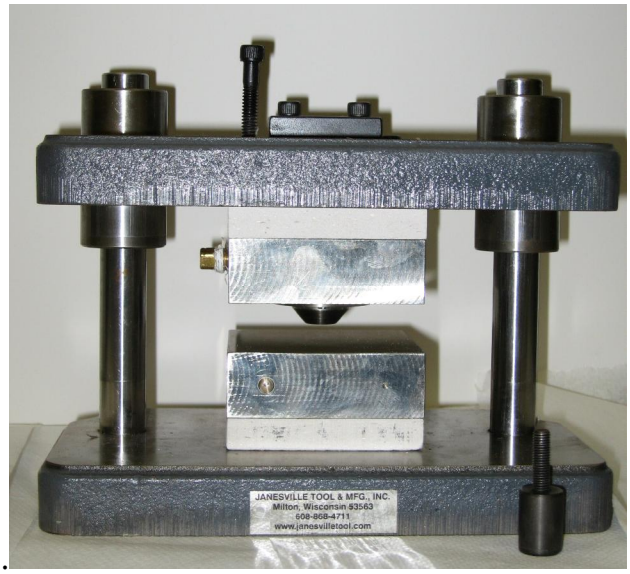

Figure 81: Assembled embossing tool comprising a hot plate (upper) and a cold plate (lower), fastened to a platen set.

The fabrication process consists of a series of sequential operations, i.e., mold preheating, embossing, cooling, mold opening, and finally part ejection from the mold, as illustrated in Fig.82. Before embossing, a machined polymer piece, 75 × 37.5 × 6.4 mm, was placed on the lower plate, and at the same time the top plate was heated to reach the designated embossing temperature. The embossing stage was commenced by activation of the optical switch and movement of the ram on the pneumatic press, resulting in contact of the cutter with the polymer substrate. It should be noted that the heated cutter causes the polymer to soften, thus assisting in the cutting action. Further movement of the punching cutter results in heating, softening and then squeezing of the polymer billet inside the mold cavity. The embossing stage was constant force controlled. After a designated embossing period elapsed, the heated top plate was cooled by circulating with tap water. At the end of the cooling cycle, the embossing force was released. The embossed waveguide is attached to the polymer substrate at the circumference with a ring in a thickness of 0.5 mm, similar to a ring gate in injection molding. The waveguide was manually ejected from the mold by cyclic loading on both sides of the polymer blank.

Care was taken to ensure that the vibrations were within the elastic range of the material to prevent any damage to the embossed part. The ring connector was mechanically trimmed off to disconnect the embossed waveguide from the polymer sheet. In production, the cutter could cut all the way throughout the entire blank thickness, thus eliminating the trimming step. This, however, requires a more sophisticated ejection mechanism and redesign of the mold, and was therefore not investigated in this study.

5.4 Embossing Results and Discussion

ABS was chosen as the polymer for through-thickness embossing of the multichannel waveguide. The polymer has a glass transition temperature (Tg) at 105°C. Design of experiments was carried out to optimize the major process parameters, including tool temperature and embossing force, so as to obtain complete replication of the waveguide. The optimum embossing condition was found to be 140°C (embossing temperature) and 4,000 N (embossing force). The waveguides fabricated under these conditions demonstrated complete mold fill, as well as sharp edges and smooth surface along the channels, as shown in Fig.83. The entire embossing stage, starting from the contact between the cutter and the polymer and ending at the beginning of the cooling stage, lasted for 3 min. The constant force control scheme, rather than constant speed control, is considered advantageous in the present application. In the constant force case, the softening process and the deformation process are automatically synchronized in a creeping mode; that is, deformation carries on as the polymer at the contact softens. This helps protect the cutter's blade, on one hand, and create a stable process, on the other hand. The small contact area between the cutter blade and the polymer, as opposed to the large contact area in the standard embossing process, helps maintain a small deformation zone on the polymer substrate. The non-isothermal embossing setup, rather than an isothermal setup in the standard embossing process, is also considered beneficial. This is understandable since the material away from the cutter is maintained below the glass

transition temperature, thus reducing the amount of squeezing flow toward the surrounding area. At the end of the embossing stage, tap water was circulated inside the heated plate, while the same embossing force was applied on the tool to produce a holding pressure. The force was removed when the heated plate was cooled to about 70°C. The total cycle time was 7 min. The embossing force and temperature were found to have a profound influence on the quality of the embossed waveguide. To study such effects, the embossing process was carried out at varied embossing temperature and force. At a lower embossing temperature, e.g., 120°C, complete fill of the mold cavity did not occur even with the application of a higher embossing force, e.g., twice higher, as shown in Fig.84a. At a higher embossing temperature, e.g., 160°C, incomplete fill also resulted, as shown in Fig.84b. The former case is easy to understand considering the increased resistance, i.e., increased viscosity, of the polymer to deformation at a lower temperature. The latter may be attributed to the increased lateral flow to the adjacent area, thus lowering the pressure in the cavity. This increased outflow was actually observed in the experiment.

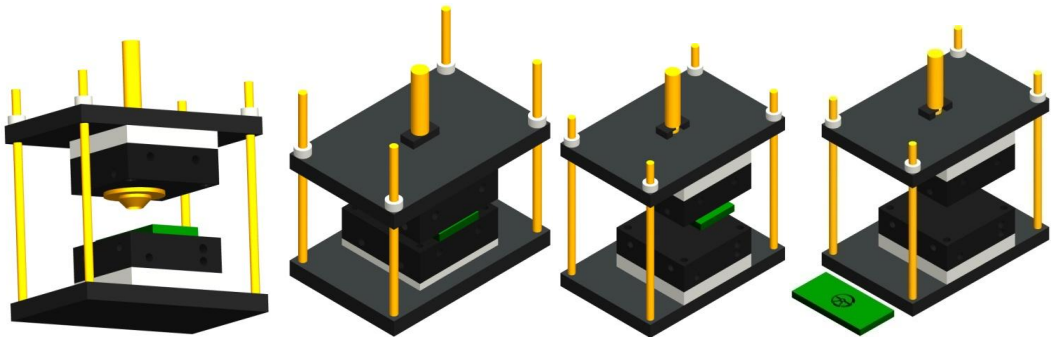

a) b) c) d)

Figure 82: Stages involved in through thickness embossing: a) mold preheating, b) embossing and cooling, c) mold opening, and d) part ejection.

The effect of the embossing force was also investigated. The embossing temperature was kept at 140°C while the embossing force was varied. Lower embossing

forces, e.g., 3,000 N, resulted in surface irregularities and incomplete fill of the post on the waveguide, as shown in Fig.85. The surface irregularities suggest incomplete packing of the polymer into the mold cavity.

Similar parametric studies were conducted for PMMA. For PMMA, complete cavity fill was achieved at a mold temperature of 180°C and an embossing force of 4,000 N. Similar to the ABS case, considerably lower or higher embossing temperature than the optimum temperature resulted in incomplete cavity fill. The PMMA waveguide was found to be more difficult to eject and often fractured during ejection. The increased ejection difficulty can be accredited to the relatively brittle nature of PMMA as compared to ABS, a toughed copolymer.

5.5 Modeling of Through-Thickness Embossing

The through-thickness embossing process that involves a punching mechanism as described above is highly non-isothermal. The process starts from a line contact between the tool and the polymer. The polymer that contacts with the punching cutter is instantaneously heated, creating a sharp temperature gradient near the cutter edge. This, in turn, creates a large gradient in viscosity, as polymer's viscosity is extremely sensitive to thermal changes. The large gradient in viscosity results in a localized deformation zone surrounding the cutter edge. From previous investigations in non-isothermal embossing processes, such localized deformation greatly influences the cavity filling process. Since a hot mold is employed in hot embossing, it is difficult to experimentally produce frozen partial fills. This is different from injection molding. In injection molding, partial cavity fills can be readily created, because the polymer in contact with a cold mold instantaneously freezes when flow is stopped. In order to study the thermomechanical changes during the through-thickness embossing process and generalize the findings for other process conditions, a thermal flow model for the process is needed.

Hot embossing involves deformation of polymer near the glass transition temperature. Rheological behavior at such a meso-temperature range is quite complex. Considering the long embossing stage, three minutes long, in the waveguide embossing process as described above, one may adopt a creep flow model. As such, a viscous material model with a temperature shift factor can be used to approximate the more complex rheological properties. Further, the deformation rate during the prolonged embossing stage is estimated to be low, and thus one may drop the strain rate dependence in the viscosity model.

The thermal creep flow model used in the waveguide embossing simulation solves the simplified conservation equations, as follows:

$$\nabla \cdot \underline{v} = 0 \tag{29}$$

$$-\nabla p + \nabla \cdot [\eta(\nabla \underline{v} + \nabla \underline{v}^T)] = 0 \tag{30}$$

$$\rho c_p \left(\frac{\partial T}{\partial t} + \underline{v} \cdot \nabla T \right) = \nabla \cdot (k \nabla T) + 2\eta(\nabla \underline{v} + \nabla \underline{v}^T) : \nabla \underline{v} \tag{31}$$

where $\underline{v}$ is a velocity field. The inertia and body force effects are neglected in the momentum equation. This is justified by the high viscosity of the polymer near the glass transition temperature. The temperature dependency of viscosity is modeled using the following equation:

$$\eta(T) = \eta(T_g) \cdot \exp\left[-\frac{C_1(T - T_g)}{C_2 + T - T_g} \right], \tag{32}$$

where C_1 and C_2 are material constants in the temperature shift factor. Below Tg, an infinite viscosity was assigned to the polymer. The representative material parameters for ABS were chosen for the embossing simulation, as listed in Table 2.

Compared with the microlens embossing process, the through-thickness embossing process in this study involves much larger deformation, particularly in the vicinity of the punching cutter. Thus, special care was taken to ensure convergence of the

solution. Specifically, an adaptive meshing method was used to re-mesh the geometry in the vicinity of the contact at each time step. A small radius was also added to the sharp cutter edge to improve convergence of the solution.

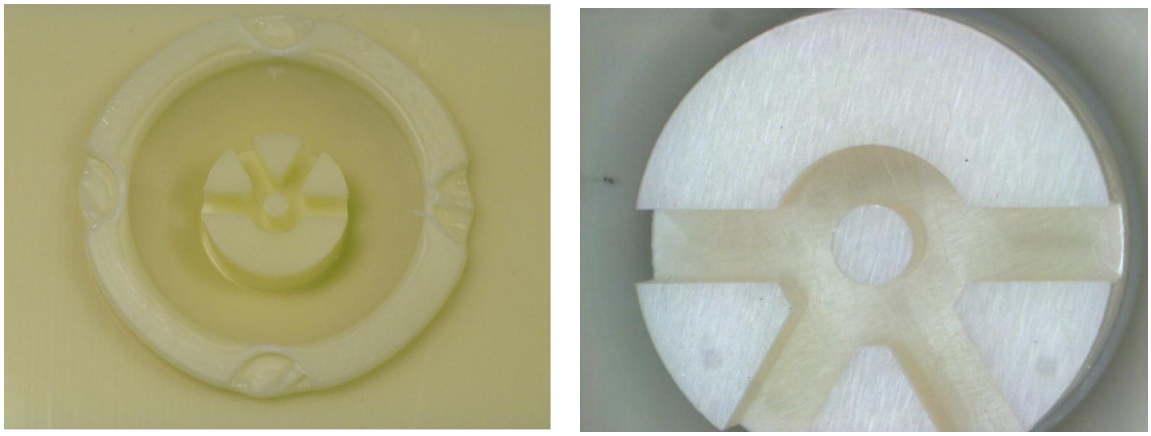

a) b)

Figure 83: Waveguide embossed at an embossing temperature of 140°C and an embossing force of 4,000 N: a) before trimming and b) after trimming.

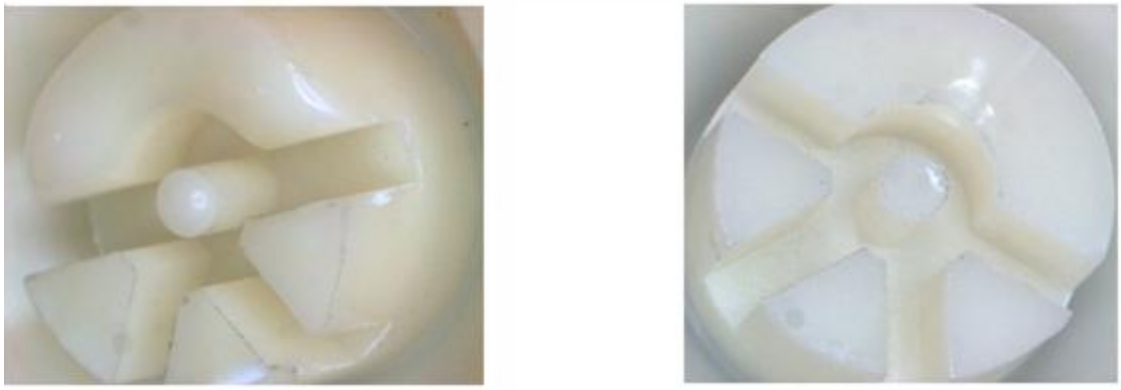

a) b)

Figure 84: Parts with incomplete mold fill (visible short shots), embossed at different temperatures: a) 120°C and b) 160°C.

a) b)

Figure 85: Effect of lower embossing force on the embossed waveguide: a) partially filled post and b) surface irregularities.

The geometry and boundary conditions are shown in Fig.86. An axisymmetric geometry was used to approximate the more 3-D geometry of the waveguide. The flow boundary conditions are: BC.1 (axisymmetry), BC.2 ($v_n = 0$ and $f_s = 0$, where v_n is normal velocity and f_s is tangential stress), BC.3 (periodic symmetry), BC.4 (free surface with contact detection), and BC.5 (mold surface to be contacted). The thermal boundary conditions are: BC.1, BC.2, and BC.3 (zero heat flux), BC.4 (zero heat flux before contact but convective after contact is detected), and BC.5 (constant mold temperature). After contact is detected on BC.4, the convective heat transfer coefficient is equal to the thermal contact conductance between the polymer and the mold. Three regions, R.1, R.2, R.3, are labeled in the figure to study the flow behavior in these different regions. The cutter edge is denoted as Point C.

The finite element method was used to solve the governing equations with the material properties and boundary conditions given above.

5.6 Simulation Results and Discussions

Isothermal through-thickness embossing was simulated first. In this case, both mold and polymer were set to a constant temperature at 140°C. The embossing time was set to 180 s. Fig. 87.a shows the simulated flow pattern. The normalized time in the figure is defined as $\tilde{t} = t / t_p$, where t is the actual time and t_p is the processing time. Complete fill of the waveguide geometry is not achieved in this isothermal case, even when the cutter cuts through the whole substrate thickness. This filling difficulty may be explained by the unique flow mechanism in isothermal through-thickness embossing. The squeeze flow results in gradual filling of R.1 and R.2, but also increases the thickness of the substrate, i.e., R.3. By the end of filling, the substrate has experienced a thickness increases above 15% in R.3. This significant outflow surrounding the waveguide cavity causes a difficulty in pressure buildup and consequently incomplete fill of the cavity.

One could study if changes in process conditions, e.g., changes in the isothermal temperature and embossing speed would help with the cavity filling process. However, these adjustments do not improve the percentage of cavity fill in the isothermal embossing case. This can be theoretically proved by rewriting the momentum equation in a process condition independent format:

$$-\nabla\tilde{p} + \nabla\cdot[(\nabla\underline{\tilde{v}} + \nabla\underline{\tilde{v}}^{T})] = 0 \qquad (33)$$

where $\underline{\tilde{v}}$ is defined as $\underline{\tilde{v}} = \frac{\partial \underline{x}}{\partial \tilde{t}} = t_p \underline{v}$, and $\tilde{p}$ is defined as $\tilde{p} = \frac{t_p p}{\eta(T)}$. From Equation (33), it can be seen that the material is at the same position, $\underline{x}$, at a given $\tilde{t}$. Therefore, the same degree of cavity fill is obtained at the end of embossing, i.e., at $\tilde{t} = 1$.

In the non-isothermal case, the degree of cavity fill is expected to be dependent on process conditions. In this case, the variation of the thermal field results in a gradient in the viscosity, and therefore Equation (33) is not valid. Two non-isothermal embossing cases were simulated. The interfacial conductance between the mold and polymer was

taken to be infinite. The simulation results were compared with those in the isothermal case. The comparisons are shown in Fig.87, Fig.88, and Fig.89.

Fig.87 compares the advancement of the flow front under different thermal conditions. The mold temperature was set to 140°C for all three cases, but the initial temperatures of the polymer were set differently at 140, 120, and 100°C. For the two nonisothermal cases, one has an initial temperature above Tg and the other below Tg. It can be seen that, as the polymer temperature is increased, the degree of fill at a given time instant is improved. At a polymer temperature of 120°C, the cavity can be completely filled at $\tilde{t} = 0.93$. As compared with the isothermal case, the squeeze flow is more confined at the tool-polymer contact. There still exists outflow surrounding the cavity, but the outflow is more confined in the vicinity of the cutter. The increase in substrate thickness is around 5% at the end of complete cavity fill. This substantially reduced outflow can be used to explain the increase in cavity fill in this nonisothermal case. As the polymer temperature is further reduced to 100°C, below Tg, the above difference becomes more drastic. The time for complete cavity fill further reduces to $\tilde{t} = 0.65$. The outflow in this case is more confined, and essentially becomes a wall-climbing flow. At the end of the cavity fill, no change in substrate thickness can be detected. It is also seen that a relatively large cushion layer of polymer is retained at the end of the cavity fill. This cushion layer is considered important, as it supplies additional polymer during the holding/cooling stage to compensate for the thermal shrinkage.

The vast change in flow pattern can be understood by examining the velocity field during the embossing stage, as shown in Fig.88. Under isothermal embossing, the velocity field is distributed quite evenly in the entire substrate, indicating a uniform squeezing flow across the entire substrate. At a polymer temperature of 100°C, the velocity field is confined near the contact, indicating a more localized squeezing flow.

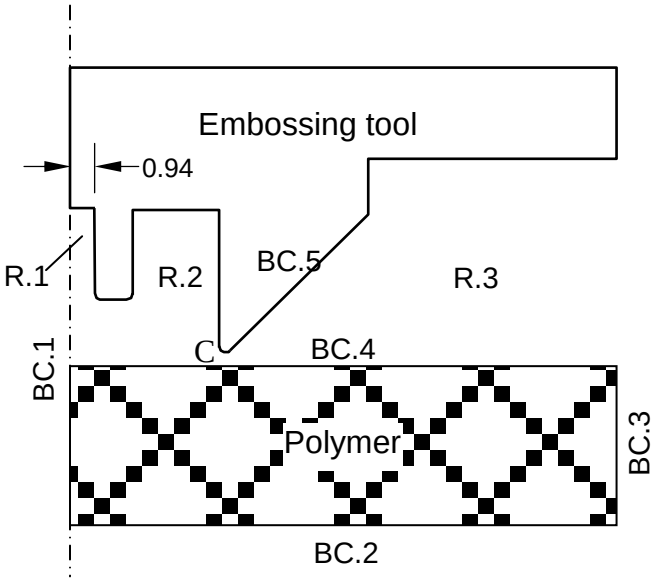

Figure 86: Geometry and boundary conditions used in waveguide embossing simulation. The flow boundary conditions are: BC.1 (axisymmetry), BC.2 ($v_n = 0$ and $f_s = 0$, where v_n is normal velocity and f_s is tangential stress), BC.3 (periodic symmetry), BC.4 (free surface with contact detection), and BC.5 (mold surface to be contacted). The thermal boundary conditions are: BC.1, BC.2, and BC.3 (zero heat flux), BC.4 (zero heat flux before contact but convective after contact is detected), and BC.5 (constant mold temperature). After contact is detected on BC.4, the convective heat transfer coefficient is equal to the thermal contact conductance between the polymer and the mold. Three regions, R.1, R.2, R.3, are labeled to study the flow behavior in these different regions. The cutter edge is denoted as Point C.

Fig.89 provides simulated temperature distributions in the nonisothermal embossing cases. For generality, the temperature was normalized, defined as $\tilde{T} = (T - T_i)/(T_m - T_i)$, where T_i is the initial temperature and T_m is the mold temperature. The evolution of the thermal field can be used to explain the unique flow pattern in the nonisothermal embossing case. At the initial embossing stage, $\tilde{t} = 0.25$, high temperature is localized at the contact point only, thus resulting in a localized flow surrounding the cutter edge. As time elapses, the high temperature zone enlarges, and the flow field inside the cavity becomes more uniform, particularly for the higher initial temperature case. Effort was made to simulate through-thickness embossing at lower initial polymer temperature, e.g., T = 25°C. However, convergence of the solution was not achieved, since an extremely fine mesh size was unaffordable for simulating the extremely high gradient of the field variables near the contact. Nevertheless, one may use the dimensionless temperature obtained in Fig.89 to estimate the temperature evolution in other cases with a lower polymer temperature. For example, given $T_i = 25°C$, one can use $\tilde{T} = 0.7$ to estimate the size of the zone near the contact that has reached the glass transition temperature. In Fig.89, this corresponds to a zone with a color of red and yellow. This method should offer a quick estimation as long as the process is speed controlled with the same embossing time. In general, the results in Fig.87 and 88 suggest that, as the polymer temperature reduces, the zone with temperature above Tg reduces, thus resulting in a more confined flow field near the polymer-cutter contact, i.e. Point C in Fig.86. The more confined flow field promotes the flow inside the cavity and consequently the complete fill of the cavity. It should also be mentioned that reduction in temperature, however, causes an increase in viscosity, and therefore a higher embossing pressure is needed.

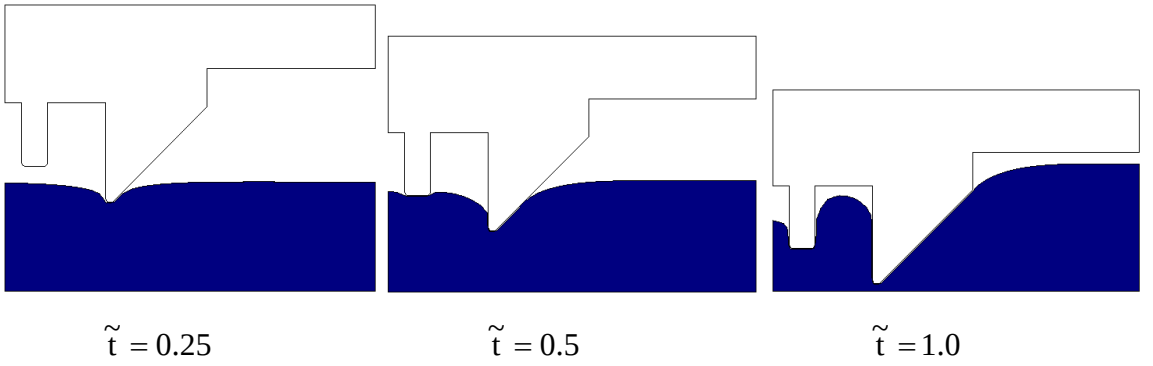

$\tilde{t} = 0.25$ $\tilde{t} = 0.5$ $\tilde{t} = 1.0$

a)

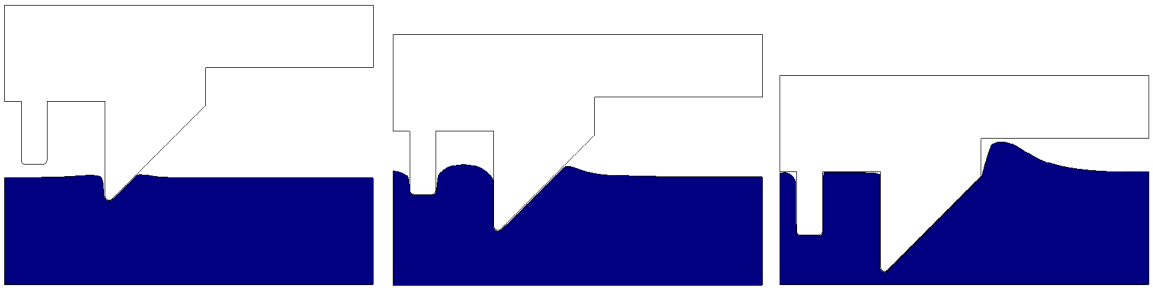

$\tilde{t} = 0.25$ $\tilde{t} = 0.5$ $\tilde{t} = 0.93$

b)

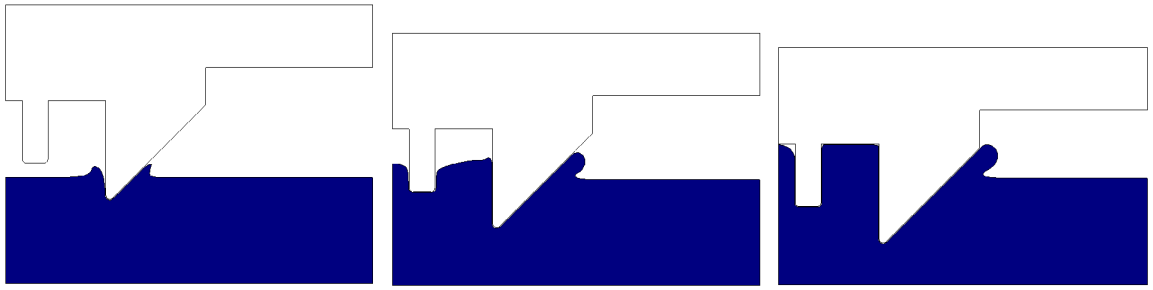

$\tilde{t} = 0.25$ $\tilde{t} = 0.5$ $\tilde{t} = 0.65$

c)

Figure 87: Simulated flow patterns using different tool temperatures: a) 140°C, b) 120°C, and c) 100°C. The dimensionless time, $\tilde{t}$, is defined as $\tilde{t} = t / t_p$, where t is the actual time and t_p is the processing time.

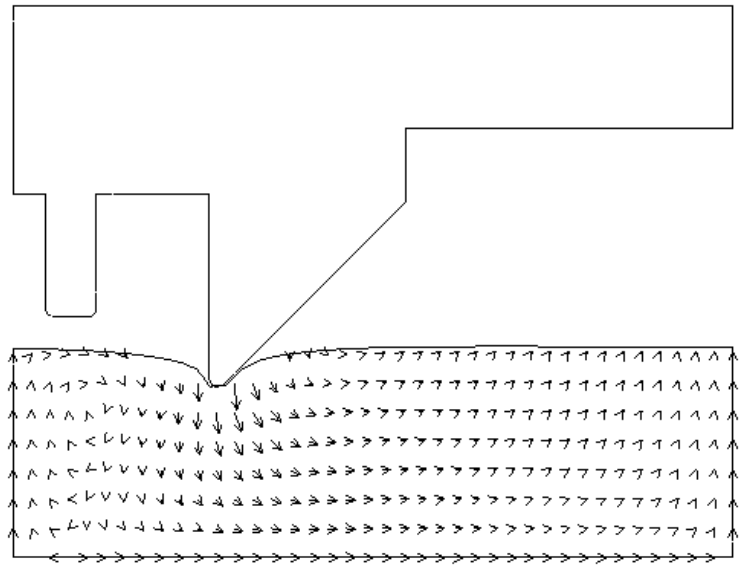

a)

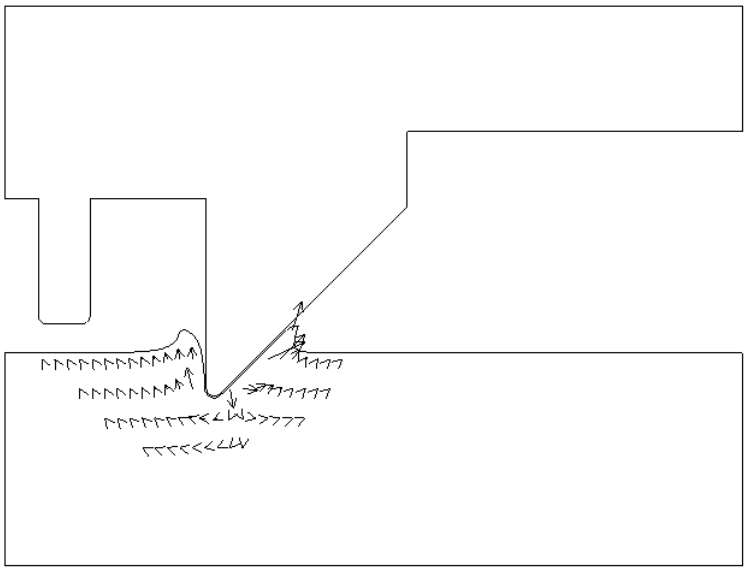

b)

Figure 88: Simulated velocity fields with different initial temperatures: a) 140°C and b) 100°C.

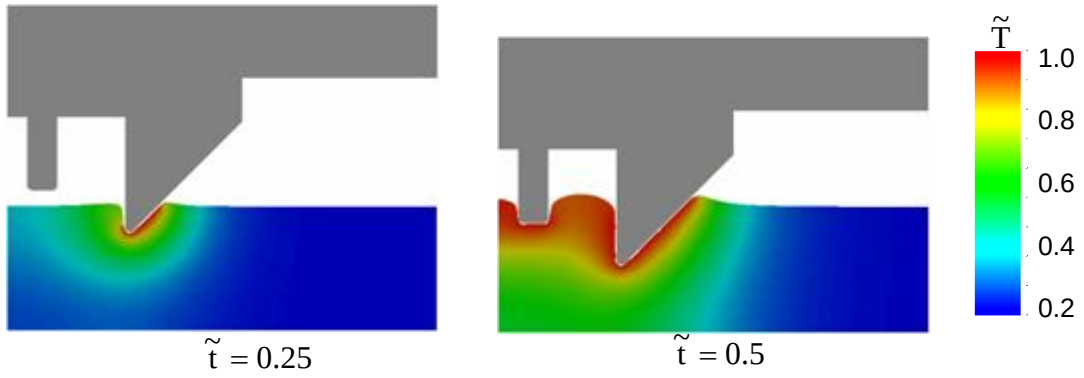

a)

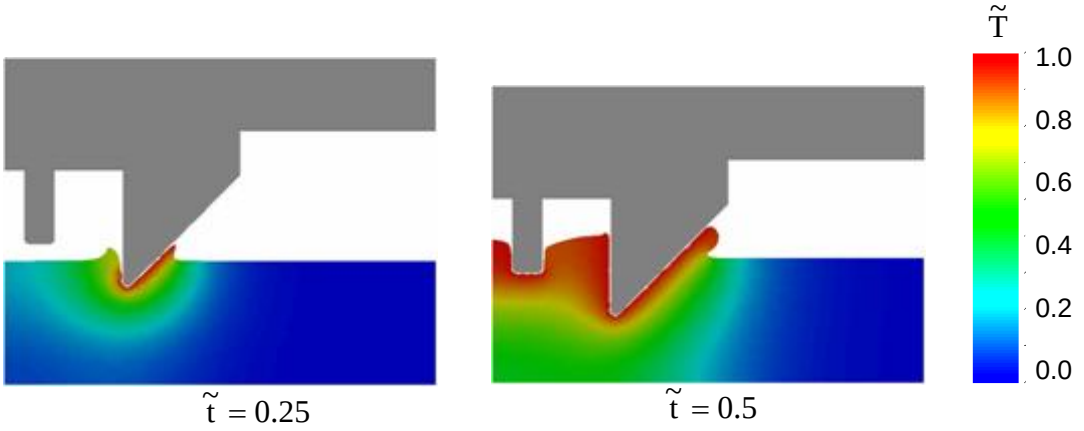

b)

Figure 89: Simulated temperature distributions with different initial temperatures: a) 120°C and b) 100°C. The dimensionless temperature, $\tilde{T}$, is defined as $\tilde{T} = (T - T_i)/(T_m - T_i)$, where T_i is the initial temperature and T_m is the mold temperature.

CHAPTER 6

PRINCIPLE OF RUBBER-ASSISTED EMBOSSING

6.1 Introduction

The current hot embossing techniques for fabricating shell geometries are limited by alignment and demolding issues. In this study, a rubber-assisted embossing process was developed to facilitate the fabrication of shell type geometries. In the sheet metal forming industry, a rubber-assisted forming process has been used for many years [38]. The advantages of using rubber as a counter tool include protection of sheet metal surface, flexibility of operation, and low tooling cost. Rubber, with much lower modulus than that of the sheet metal, deforms like a liquid to allow for conformal deformation and yet buildup of uniform forming pressure. This soft counter tool approach may be adapted to the hot embossing process. However, due to the vast difference in material properties between polymer and metal, the process characteristics of rubber-assisted polymer embossing may be considerably different from that of rubber-assisted sheet metal forming. Particularly, polymer films in a solid form are very elastic and thus difficult to form, while metal sheets typically have good plasticity even at room temperature. Thus, the polymer film needs to be heated above its softening temperature, that is, the glass temperature for an amorphous polymer and the melting temperature for a semicrystalline polymer, before forming.

Fig.90 shows different stages involved in the rubber-assisted embossing process. First, a polymer film placed between a metal die and a rubber pad is pressurized. At the same time, the metal die is heated to a temperature higher than the softening temperature of the polymer. Elevated mold temperature is required, in order to prevent premature

freezing of the polymer during embossing [33].When the polymer film is heated sufficiently, it starts to deform between the hard die and the rubber pad. The rubber pad also deforms under the load and acquires the profile of the die, acting as a negative counter tool to the positive metal die. The conformal deformation undergone by the rubber during the patterning stage helps to eliminate the difficulty in aligning, as encountered by a pair of matched dies [7]. At the end of the embossing stage, the assembly of the mold, the polymer and the rubber base is moved to the cooling stage and the pressure is reapplied. In the case of isothermal rubber-assisted embossing, both the polymer film and the mold are preheated above the softening temperature of the polymer, followed by embossing and cooling stages.

Unlike the roll embossing process, the use of sufficient holding time during rubber-assisted hot embossing may prevent relaxation of the patterned film and thereby maintains the fidelity to the original geometry. As the pressure is released at the end of the holding and cooling stages, the deformed rubber counter tool bounces back to its original shape, facilitating ease of ejection. The use of a rubber pad as a counter tool also prevents damage to the metal master during the embossing process.

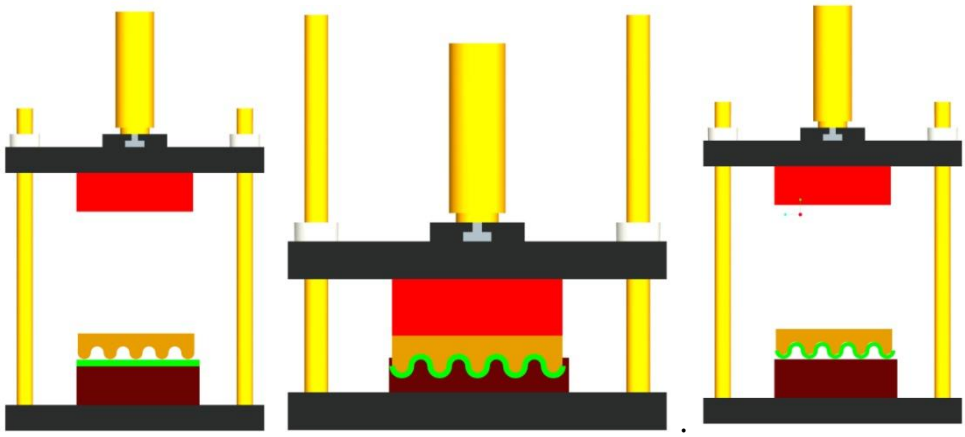

a) b) c)

Figure 90: Rubber-assisted embossing: a) mold Preheating stage, b) embossing and cooling, and c) mold opening stage.

Rubber as a material for the counter tool is considered to be more advantageous than a thermoplastic material, e.g., a polymer or a paraffin, as used in the literature [7,28]. There are some technical challenges in determining an appropriate thermoplastic cushion material. This thermoplastic cushion material needs to be softened together with the embossing film, and therefore the two materials should have similar softening temperature. Moreover, the cushion material should have appropriate deformability. If the cushion material should be too stiff, it would be difficult to achieve uniform thickness of the patterned film. On the other hand, should the cushion material be too soft, it could squeeze out easily during embossing, since hot embossing is an open-die process. Other challenges arise considering the demolding process. The cushion material and the embossing film should possess very different chemical or physical properties so that they may be separated from each other after embossing, using either a chemical or a physical process. These technical challenges can be overcome using a rubber as a cushion material. Different grades of rubber with designable stiffness are available commercially. Service temperature exceeding 200°C can also be achieved easily for these rubber materials. Furthermore, demolding is not an issue when rubber is used as a cushion material, because of the elastic recovery of the rubber.

6.2 Materials

Biaxially stretched PS films in a thickness of 25 μm obtained from Goodfellow Corporation were used as embossing films. The Tg of PS given by the material supplier is 100°C. Different grades of high-temperature silicone rubber sheets in a thickness of 6.4 mm were obtained from McMaster-Carr Supply Company. The Shore hardness of these rubber sheets varies from 30 to 80 A. They were cut into a size of 50×50 mm and directly used as soft counter-tools.

6.3 Embossing Stamp

A stainless-steel stamp (25×10×1.5 mm) with grooves running in the direction of the short side was used as an embossing die. To fabricate this die, the steel was first precision ground and then machined using a micro wire EDM process, with a wire diameter of 50 μm . The geometry and dimension of the groove are shown in Fig.91. The microgrooves are approximately 100 μm wide and deep. For this die geometry, the diameter of the EDM wire is small enough to machine the details on the die.

6.4 Embossing Setup

A pneumatic press was modified and used as a hot embossing unit. Fig.90 shows a schematic setup of the rubber-assisted embossing process. A 126.2×126.2×25.4 mm stainless steel block attached to the upper platen of the pneumatic press was used as a heated platen. This upper platen was heated by two 250-W cartridge heaters of 12.5 mm in diameter. The micro patterned stamp was mechanically fixed to the upper platen. At the startup, a PS film was placed between the stainless steel stamp and a rubber pad. The heated platen with the stamp then moves downward and pressurizes the polymer film and the rubber pad against the lower platen. Cooling was performed by circulating water through the cooling channels embedded in the upper platen. When the film is cooled significantly below the polymer softening temperature, the mold is opened.

6.5 Characterization

The viscoelastic properties of the PS film at temperatures close to its glass transition temperature was measured using DMA (Mettler Toledo, Model No. DMA861e). Embossed PS films were examined using stereo optical microscopy and SEM (Hitachi S-800 SEM).

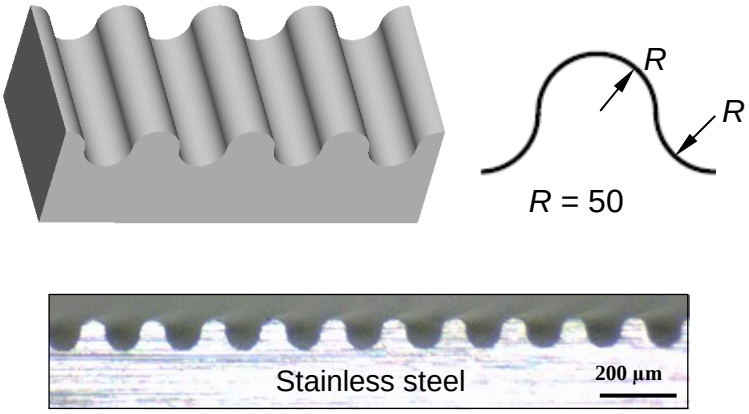

Figure 91: A stainless-steel embossing mold with protruded micro features

6.6 Results and Discussion

The major process parameters involved in rubber-assisted embossing includes embossing temperature, ejection temperature, embossing pressure, isothermal dwell time, cooling time, and rubber hardness. After the mold contacted with the polymer film, an isothermal dwell was applied until the cooling circuits filled with tap water were activated. An isothermal dwell time of 10 s was found to be sufficient to stabilize the process and was thus used in all experiments. The same embossing pressure as in the isothermal dwell stage was maintained throughout the cooling stage. Compensation of thermal shrinkage was thus made possible during cooling. The mold was opened when cooled below 50°C. This same ejection temperature was used in all experiments. For an embossing temperature of 140°C, a corresponding cooling time of 170 s was needed. With the present setup, the cooling time was not an adjustable process parameter. Rather that that, it depended on the hardware setup and the initial temperature, i.e., the embossing temperature. Thus, the independent process variables actually adjusted in the experiments were the embossing temperature, the embossing pressure and the rubber hardness.

Fig.92 shows a replicated film pattern embossed at an embossing temperature of 120°C, an embossing pressure of 2.5 MPa, and a rubber Shore hardness of 60 A. The full

depth of the circular groove was satisfactorily produced (Fig.92a). The surface of the replicated groove on the stamp side also exhibited a rough surface topography (Figure 92b). This rough surface appearance resulted from the replication of the rough surface finish of the stamp fabricated by the micro wire EDM technique.

The quality of the embossed film pattern was found to depend on the embossing temperature, the embossing pressure, and the rubber hardness. Particularly, the embossing temperature significantly affected the depth of the embossed pattern and the uniformity of the patterned thickness, as shown in Fig.93. In the figure, the upper side of the film was deformed against the rubber pad and the lower side against the stamp. This is also the case for all remaining micrographs presented next. The pattern in Fig.92a was used as a control and reprinted in Fig. 93b. The same embossing pressure and rubber Shore hardness as in Fig.92a were used for all cases in Fig. 93. Although the PS film embossed at 105°C showed a uniform film thickness, it demonstrated poor replication in the patterned geometry. In contrast, embossing at 135°C resulted in full replication of the embossing depth but a large degree of film nonuniformity.

The deformation mode of shell patterning in rubber-assisted embossing is considered to be substantially different from that of surface patterning in standard hot embossing. During surface patterning, the polymer at the location of the microstructure is mainly subjected to bulk deformation, involving a large strain. In comparison, the polymer film during shell patterning undergoes deformation primarily caused by bending and stretching of the film. This deformation mode is similar to that in thermoforming and blow molding. For small-strain bending, springback is a major concern during processing. Due to springback, the deformed shape is partially recovered. The stretching of the film, on the other hand, could result in a non-uniform thickness, particularly when the stretching is against a rubber pad. The non-uniformity in film thickness is expected to be large if the rubber is a harder material than the softened polymer film.

a)

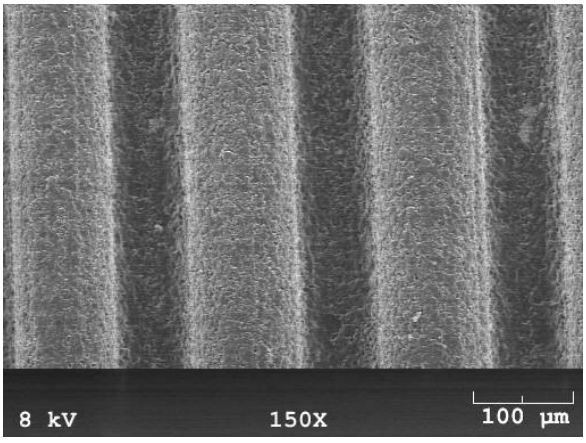

b)

Figure 92: Replicated film patterns embossed at an embossing temperature of 120°C, an embossing pressure of 2.5 MPa, and a rubber Shore hardness of 60 A: a) side view and b) front view.

a)

b)

c)

Figure 93: Micro formed polystyrene films at an embossing pressure of 2.5 MPa, a rubber Shore hardness of 60, and varied embossing temperatures: a) 105° C, b) 120° C, and c) 135° C.

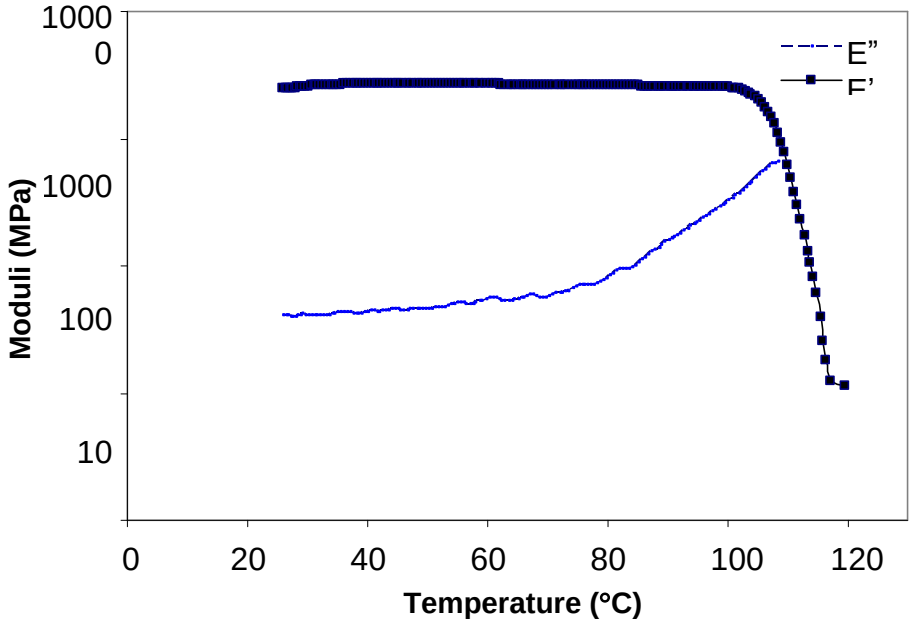

Figure 94: DMA data of the polystyrene film at a frequency of 1 Hz.

With the above understanding on shell patterning, the effect of temperature on the patterning quality can be explained. To achieve uniform stretching, a low embossing temperature is desired. At a temperature not far from Tg, the polymer film has a higher stiffness than the rubber pad. At this low temperature, the film also has a high strength for uniform stretching. However, a low embossing temperature could result in a large amount of springback caused by the elasticity of the film. DMA was performed to study the deformation behavior of the PS film at different temperatures. The storage and loss moduli at a constant frequency of 1 Hz but varying temperature are shown in Fig.94. It can be seen that the polymer experiences a vast drop in the storage modulus over a temperature window from about 105 to 115°C. When the film was embossed at 105°C, high elasticity was involved in the deformation, resulting in significant springback and poor replication of the microgroove. At this temperature, further increase of the embossing pressure, e.g., with a pressure of 5 MPa, was found to help little in improving the replicability. At an embossing temperature of 135°C, the polymer behaved quite differently; it was a viscous liquid with a vanished storage modulus. As a liquid, the film is highly plastic. However, as a softer material, its deformation was greatly influenced by the rubber pad, a harder material, thus resulting in a non-uniform thickness. The embossing temperature of 120°C turned out to be a good choice for the current process. At this temperature, the requirements for low springback and good formability were both satisfied.

The replicability at lower rubber hardness was also investigated, as shown in Fig. 95. The embossing temperature and embossing pressure were set to 120°C and 2.5 MPa, respectively. It is seen that with the reduction in rubber hardness from 60A, the replication in the microgroove depth decreased. During the experiment, it was observed that for softer rubber pads, a significant amount of rubber material was squeezed out in the lateral direction. This lateral flow results from the open-die configuration in the hot embossing process. Therefore, sufficiently high rubber hardness is needed in order to

reduce lateral flow and build up embossing pressure. Otherwise, a higher embossing pressure is needed. For a rubber Shore hardness of 40 A, complete replication was obtained at an embossing pressure of 5 MPa.

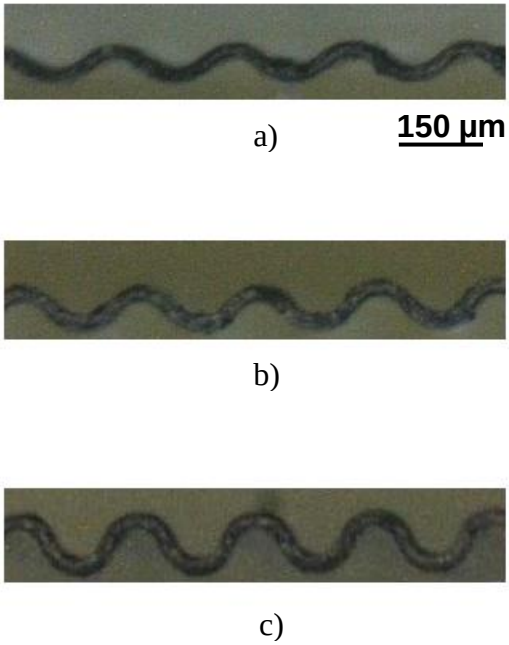

a)

b)

c)

Figure 95: Microformed polystyrene films at a embossing temperature of 120° C, an embossing pressure of 2.5 MPa, and varied rubber Shore hardness: a) 40 A, b) 50 A, and c) 60 A or above.

As expected, the embossing pressure significantly affected the patterning quality. Given a fixed embossing temperature of 120°C and a fixed rubber Shore hardness of 60 A, complete replication of the film pattern with a uniform thickness was achieved at a higher embossing pressure, e.g., 5 MPa, but short shot occurred at a lower pressure, e.g., 1 MPa. Fig.96 shows partially replicated grooves at 1 MPa. The film thickness uniformity appeared to be also influenced by the embossing pressure. This increase in film thickness nonuniformity may be understood considering the partial contact condition between the polymer film and the stamp, which could cause non-uniform film stretching.

Figure 96: Micro formed polystyrene films at an embossing temperature of 120°C, a rubber Shore hardness of 60 A, and an embossing pressure of 1 MPa.

CHAPTER 7

PARAMETRIC STUDY ON RUBBER-ASSISTED EMBOSSING

7.1 Introduction

In the preliminary work reported in Chapter 6, we identified that the pattern quality during rubber-assisted embossing is significantly affected by the embossing temperature and the hardness of the rubber pads. In order to understand the underlying mechanism and establish a fundamental relationship between the pattern quality and the embossing conditions, a more focused study is required. In Chapter 7, we report a detailed work on the rubber-assisted embossing process, involving parametric studies of the major process parameters. The polymer film was preheated to the embossing temperature in order to reduce spatial discrepancy resulting from temperature variations during nonisothermal embossing.

7.2 Materials

ABS film of 125 μm thickness, obtained from McMaster-Carr Supply Company, was used as the embossing film. The glass transition temperature of this grade of ABS was found to be 95°C. Different grades of high-temperature silicone rubber sheets with a thickness of 6.35 mm were also obtained from McMaster-Carr Supply Company. The Shore hardness of these rubber sheets varies from 30 to 60 A. These rubber sheets were cut into a size of 50×50 mm and directly used as soft counter tools. The effect of the hardness on the patterning quality was experimentally studied.

7.3 Embossing Stamp

A stainless-steel stamp of 25×12.7×2 mm with grooves running in the direction of the short side was used as the embossing die. To fabricate this die, the steel was first

precision ground and then machined using a micro wire EDM process, with a wire diameter of 100 μm. The geometry and dimension of the groove are shown in Fig.97. The microgrooves used for embossing, were about 500 μm, wide and deep, respectively. For this die geometry, the diameter of the EDM wire is small enough to machine the detail on the die.

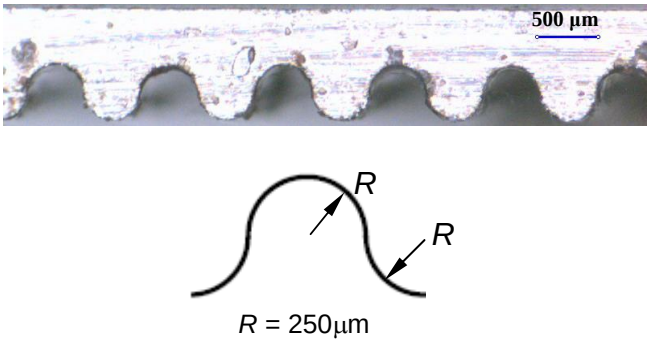

Figure 97: Stainless-steel embossing mold with protruded micro-grooves of 500 μm.

7.4 Embossing set up

Fig.98 shows the embossing setup. A 126.2×126.2×25.4 mm stainless steel block attached to the upper portion of the pneumatic press was used as a hot platen during isothermal embossing. The hot platen was heated by two 250 W cartridge heaters of 12.5 mm diameter. Before embossing, the ABS film was preheated between the heated upper platen and a hot plate inserted on the bottom. After the film was heated to a preset embossing temperature, the lower hot plate was removed. Embossing of the film was then performed between the heated upper platen and a rubber pad. After an isothermal dwell time elapsed, the heated platen was cooled by cold water circulated through the cooling channels machined along the length and width. The patternability of the ABS film was studied at different embossing temperatures of 95°C, 105°C and 115°C, rubber hardness of 40, 50 and 60A, and embossing load of 200 N and 400 N.

7.5 Material Characterization

DMA was performed to study the deformation behavior of ABS at a constant frequency of 1 Hz and a constant strain of 1%, but at varying temperatures from 35 to 110°C. The testing results are shown in Fig.99. Tensile tests with a heated chamber were carried out on ABS films at a constant strain rate of 2 s^{-1} and varying temperatures of 95, 105, 110 and 115°C. The tensile data for the ABS films are plotted in Fig.100. Tensile tests were also carried out on 30 A and 60 A silicone rubber pads at a strain rate of 3 s^{-1}. Their tensile data are given in Fig.101. The strain rates used in the tensile tests were determined based on the characteristic strain rates obtain in the simulation, as described in the next chapter.

7.6 Embossing Results and Discussion

The rubber-assisted embossing experiments were performed using a similar operation sequence as described in the previous chapter. The only difference was that the polymer film was heated to a preset embossing temperature before embossing, while in the previous experiments the film was not heated. A dwell time of 240 s was applied during the holding stage. At the end of the holding stage, cold water was circulated through the stainless steel platens. The mold was cooled to about 30°C at mold opening.

7.6.1 Effect of Embossing Temperature

SEM micrographs of replicated microgrooves on the structured ABS films prepared at different embossing temperatures , namely, 95, 105 and 115°C, but at constant load of 400 N and constant rubber shore hardness of 60A, are shown in Fig.102. In the figure, the index “R” represents the film surface deformed against the rubber pad. Under the given process conditions, the replicated pattern depth was found to be almost independent of the embossing temperature. However the uniformity in film thickness was found to deteriorate with increase in embossing temperature, as shown in Fig.103. Best uniformity in film thickness was obtained at 95° C. The film thickness was found to

decrease from the center towards the periphery for all embossing temperatures, with the maximum variation occurring at 115 °C. Fig.104 shows the normalized sheet thickness $\tilde{H}$, $\tilde{H} = \frac{\Delta H}{\Delta L^2}$, where ΔH and ΔL represents the changes in film thickness and length , respectively. For example, if a film with an initial thickness values of 0.127 mm is embossed to 0.080 mm in a microgroove of radius 0.25mm, then $\tilde{H} = 0.145$.

It is noted that there exist significant differences in deformation modes between surface patterning and shell patterning. During embossing of surface microstructures, the polymer at the location of the microstructure is mainly subjected to bulk deformation. This deformation mode is similar to that encountered in bulk forming processes, e.g. forging and compression molding of a workpiece with a relatively small surface area to volume ratio. In comparison, the polymer film during shell patterning undergoes deformation primarily caused by stretching and bending of the film. This deformation mode is similar to that in traditional sheet forming processes, e.g., sheet metal stamping, thermoforming, blow molding, etc. The major mechanism influencing shell forming quality has been taught by the abundant literature in polymer forming processes, such as thermoforming and blow molding. During these forming processes, nonuniform stretching of the shell results in nonuniform thickness of the formed sheet. To facilitate uniform stretching and a stable process, a semisolid material with a good strength is desired. This requires the employment of a lower processing temperature in forming processes than in molding and extrusion processes. On the other hand, the plasticity of the polymer is poorer at lower temperatures, resulting in a larger amount of elastic recovery and consequently poorer replicability. Likewise, for achieving a uniformly embossed and well-replicated film pattern in rubber-assisted embossing, appropriate setup of the processing temperature to achieve the desirable rheological properties is critical.

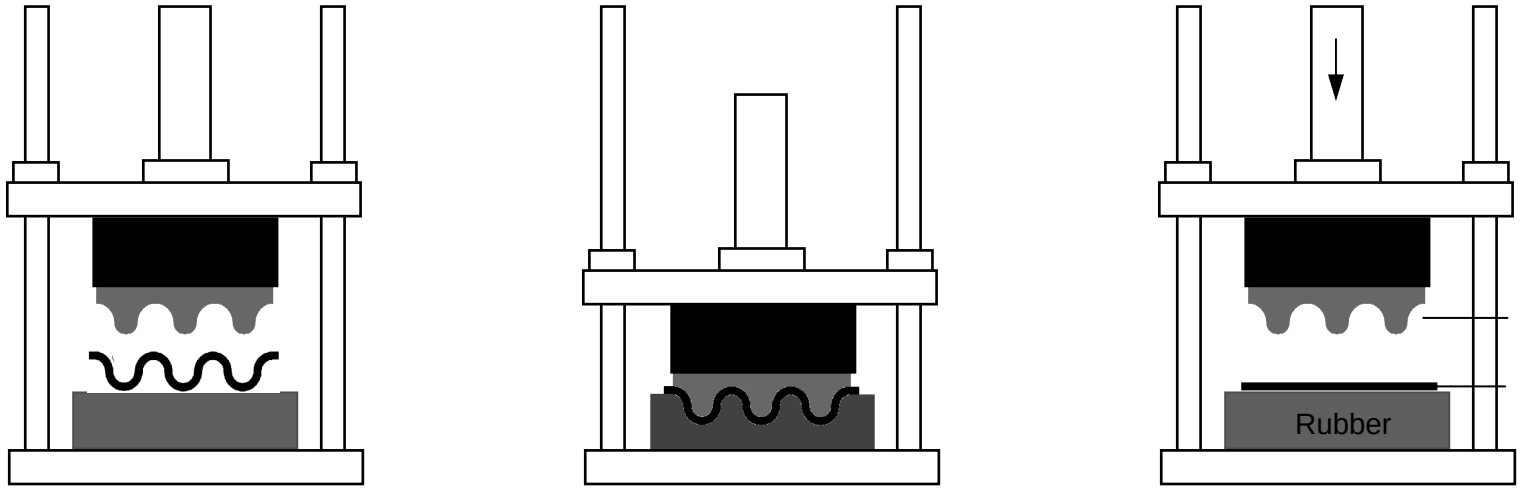

a) b) c)

Figure 98: Rubber-assisted embossing process involving several sequential stages: a) startup, b) embossing, holding and cooling, and c) mold opening.

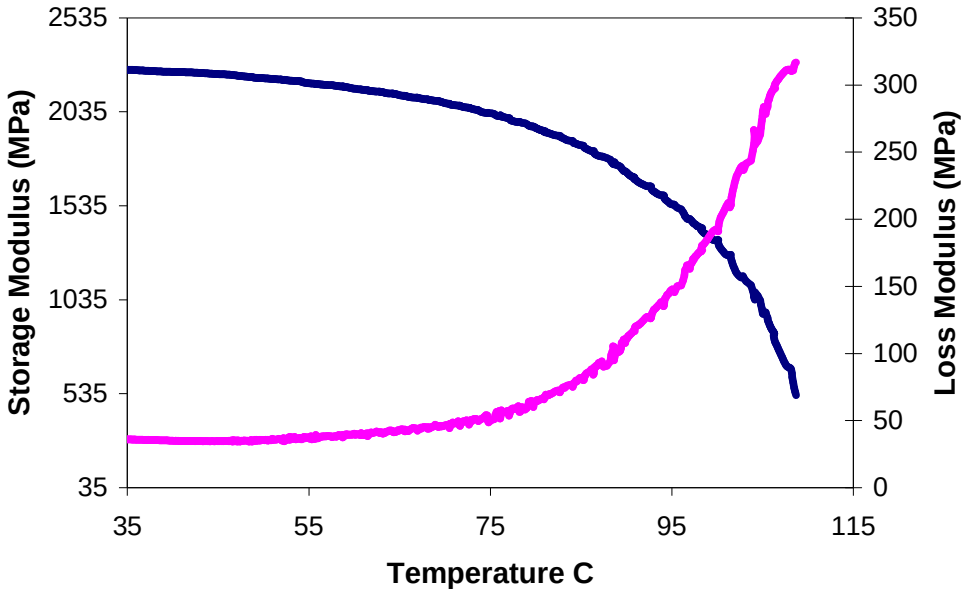

Figure 99: DMA measurement of ABS at 1 Hz and 1% strain.

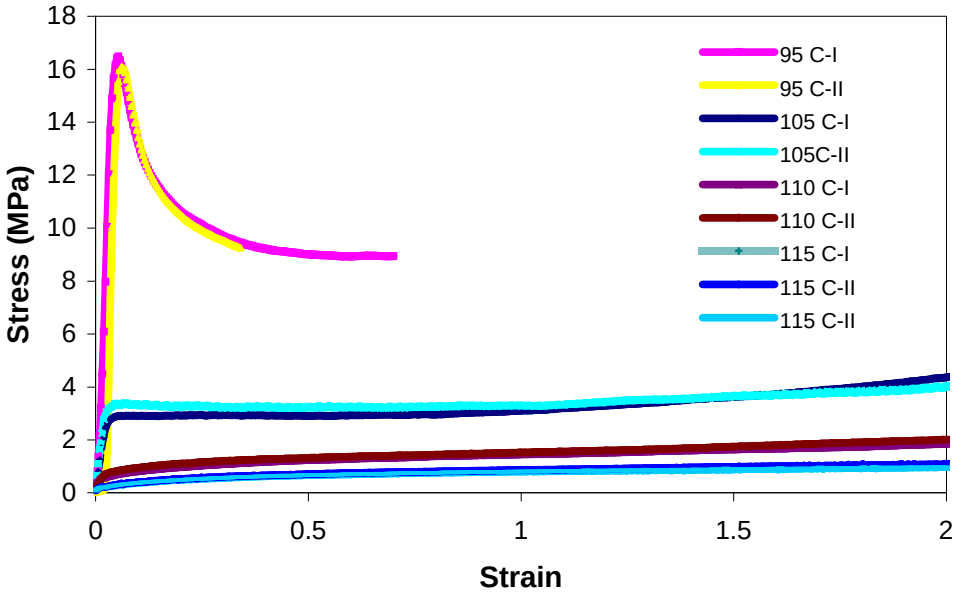

Figure 100: Tensile test data of ABS at a constant strain rate of 2 s^{-1} but varying temperatures.

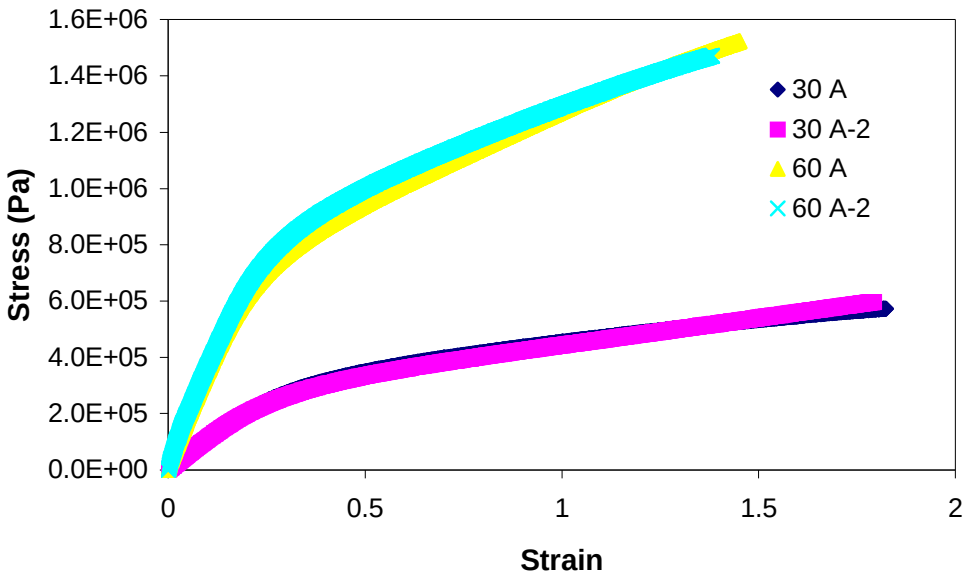

Figure 101: Tensile test data of rubber pads at a constant strain rate of $3s^{-1}$ but varying temperatures.

With the above understanding on the shell deformation mode, the effect of temperature on the quality of patterned film during the isothermal embossing may be explained. During rubber-assisted embossing, the embossing pressure is transferred from the rubber counter tool onto the polymer film, against the mold surface. The major factors affecting the quality of the replicated patterns (particularly pattern replication and pattern uniformity) include the plasticity of the polymer film, the stiffness of the polymer film, and the stiffness of the rubber pads. At lower embossing temperatures close to Tg, the embossed film possesses poor plasticity, resulting in poor pattern replication. However, it can be seen from Fig 99 that the ABS film experiences a vast drop in the storage modulus over a temperature window from about 75°C to 105°C. The first-order transition of ABS at 75 °C indicates its ability to undergo plastic deformation at a much lower temperature. This justifies ABS's excellent pattern replicability at 95°C.

Fig.105 shows the stress-strain curves of ABS and 60 A rubber pads at various temperatures. It can be seen that for an equivalent strain, the stress developed in the

polymer film at 115°C is less than that of the rubber pad at the same temperature. Thus, a nonuniform film thickness would result if the rubber should be a stiffer material as compared with the polymer film during embossing. In contrast, at 95°C, the ABS film is stiffer than the rubber pad (Fig.106), resulting in a uniform film thickness.

7.6.2 Effect of Hardness of Rubber

Fig.107 shows the patterned ABS film embossed using rubber pads with varied Shore hardness of 30 and 60A. The embossing temperature was 95°C, and the embossing load was 400 N. It is seen that the reduction in rubber hardness results in a decrease in the replication depth of the microgrooves, as shown in Fig.108. The pattern replication and uniformity in film thickness was found to improve with increasing rubber hardness. The thickness distribution was plotted against the length of the film, as shown in Fig.109. The normalized film thickness is shown in Fig.110.

It was observed that with an increase in the shore hardness the coefficient of variation of film thickness across the length of the film reduces from 19% to 8%. Better thickness uniformity was obtained with the 60 A rubber pad. The replicated depth improved from 0.478 mm to 0.497 mm with the use of the harder rubber counter tool. During embossing, the load is transferred from the stamp to the rubber pad through the contact areas, donated by AB and CD, while at BC, there is a void, as shown in Fig.108. The ratio of the representative stresses required for deforming the ABS film and the rubber pad at 95°C are 9 and 24, respectively for 60A and 30A rubber pads. Increase in the embossing load was found to be of little help in improving the pattern replication when the softer rubber pad is used. With the softer rubber pad, significant squeeze flow may occur, thus thickening the film portion in the void space. During the experiment, it was actually observed that, for the softer rubber pads, a significant amount of rubber material was squeezed out in the directions perpendicular to the direction where the embossing force was applied. This lateral flow results from the open-die configuration in

the hot embossing process. In the standard hot embossing process, the embossing film is typically thin, in a thickness less than a millimeter. In the present method, the added rubber pad resulted in a relatively thick material in deformation, thus causing lateral squeezing flow at low rubber hardness. Therefore, sufficient rubber hardness is needed in order to reduce lateral flow and build up embossing pressure.

7.6.3 Effect of Embossing Load

Fig.111 shows patterned ABS film under isothermal conditions at a constant embossing temperature of 95°C and constant rubber Shore hardness of 60A, but varied embossing loads of 200 and 400 N. Good pattern replication was observed at 200 N and 400 N. The thickness distribution across the film length was plotted against distance from the center, as shown in Fig.112. No considerable improvement in film uniformity was observed with increase in embossing load. Further increase in the embossing load had little effect on the thickness improvement.

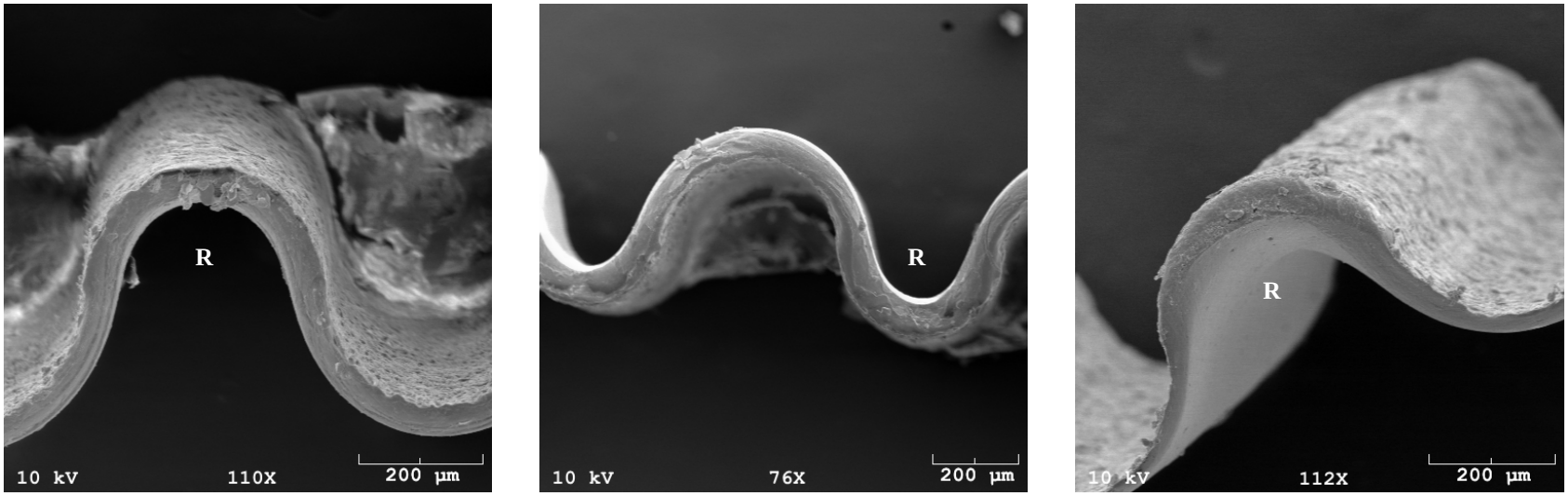

a) b) c)

Figure 102: Rubber embossed ABS films using 60A rubber, 400 N embossing force and varying embossing temperatures: a) 95°C, b) 105°C, and c) 115°C.

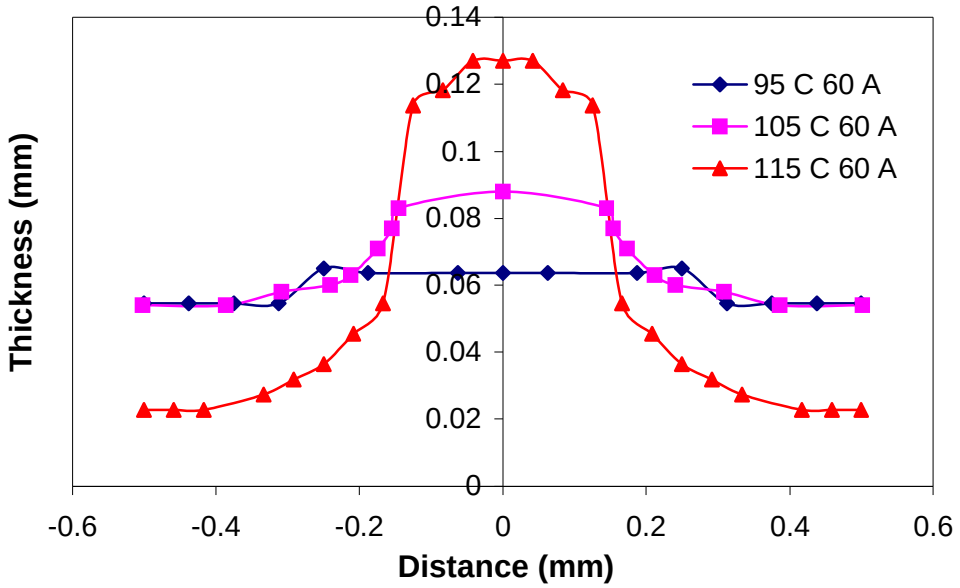

Figure 103: Thickness distribution across the length of rubber embossed ABS film at constant embossing force 400 N and constant rubber Shore hardness 60A but varying embossing temperatures.

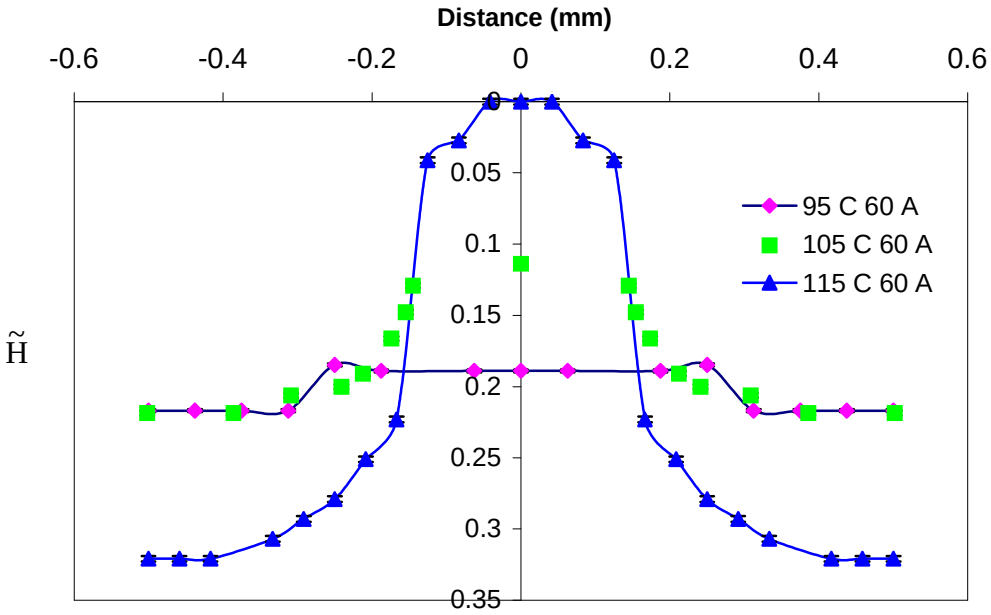

Figure 104: Normalized thickness distribution across the length of rubber-embossed ABS film at constant embossing force 400 N and constant rubber Shore hardness 60A but varying embossing temperatures.

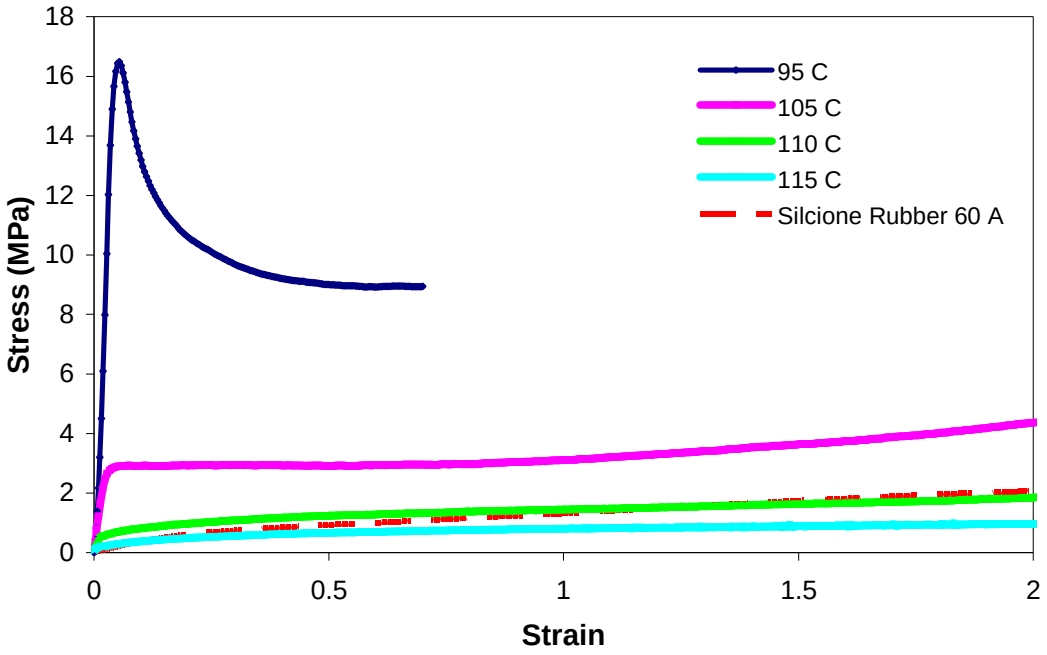

Figure 105: Different stress-strain curves of ABS film and 60 A Shore hardness silicone rubber at strain rates of 2 s^{-1} and 3 s^{-1}.

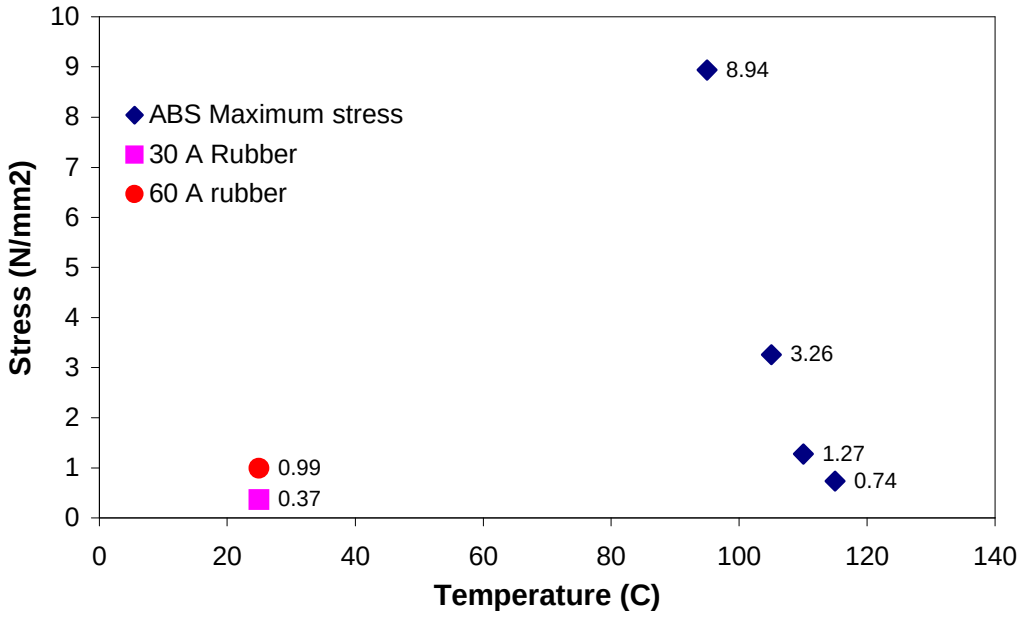

Figure 106: Comparison of maximum stress developed in the ABS film and rubber pads at 57% strain.

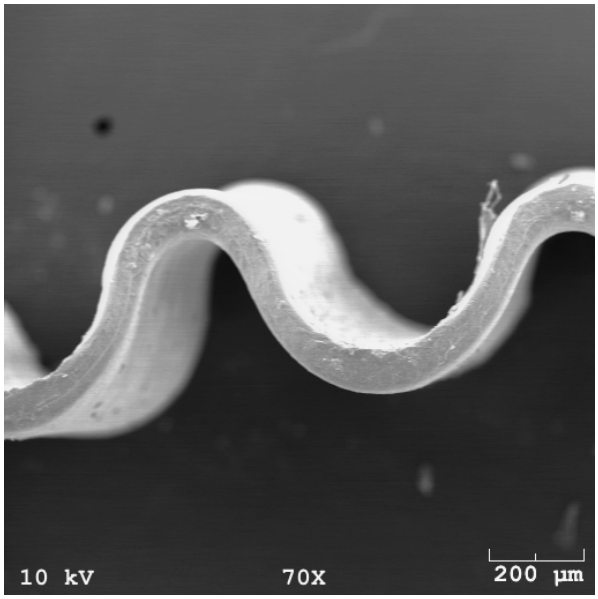

a)

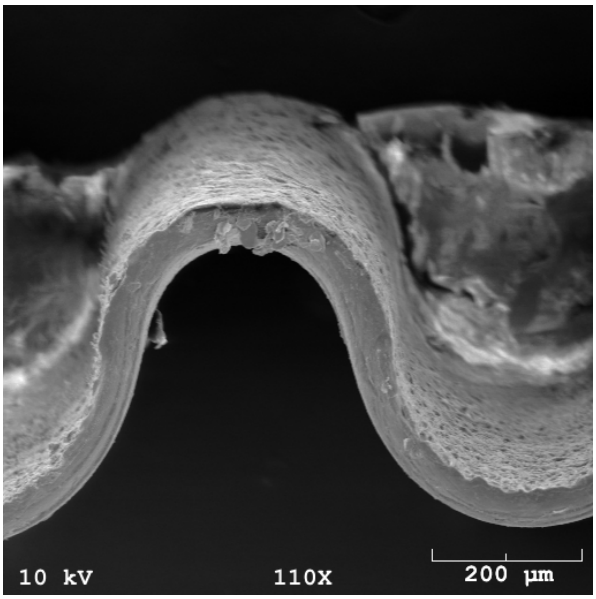

b)

Figure 107: Micro formed ABS films using rubber-assisted embossing at embossing temperature 95° C, embossing force 400 N, and varied rubber Shore hardness: a) 30 A, and c) 60 A.

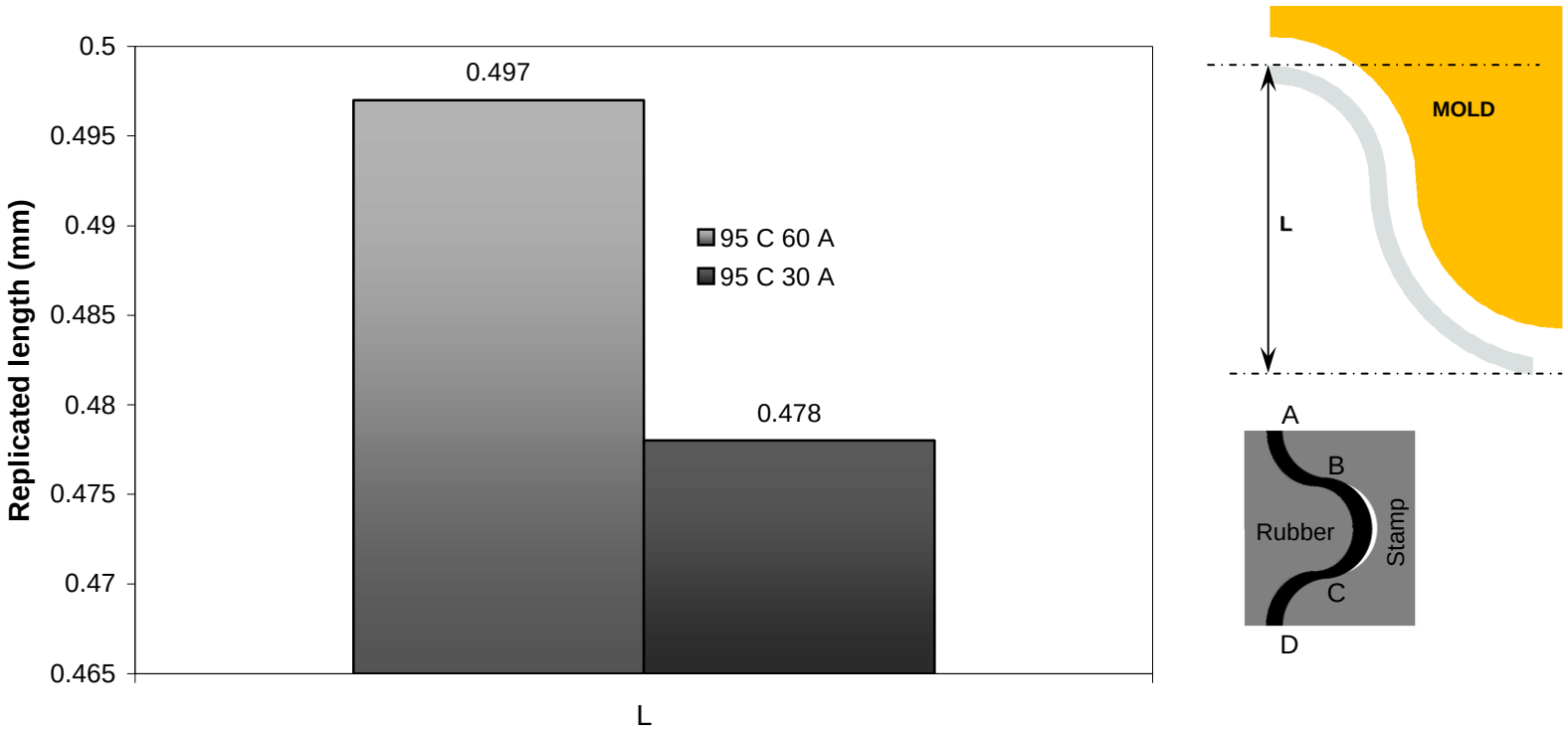

Figure 108: Replicated pattern depth for films embossed at 95°C , 400N and varying Shore hardness of 60A and 30A.

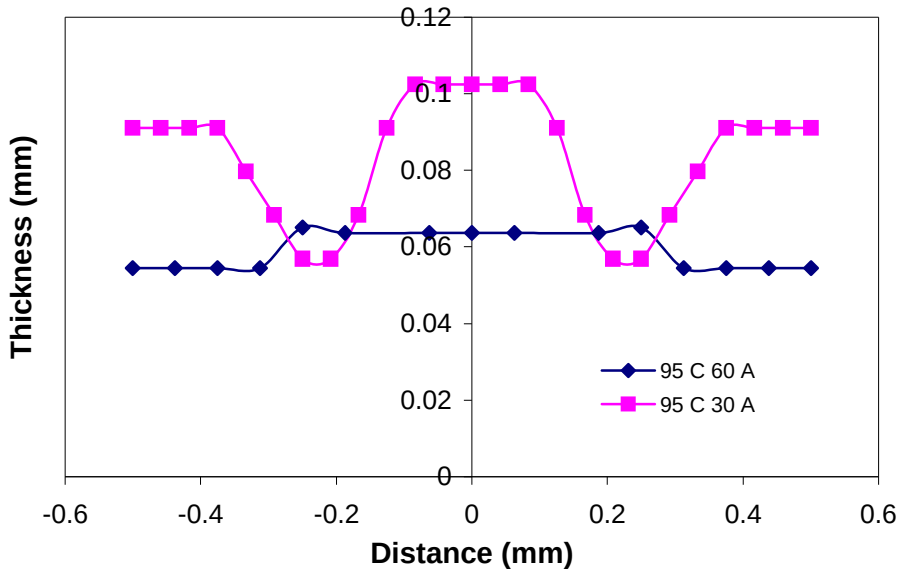

Figure 109: Thickness distribution of ABS patterns embossed at embossing temperature 95° C, embossing force 400 N, and varied rubber shore hardness 30 A and 60 A.

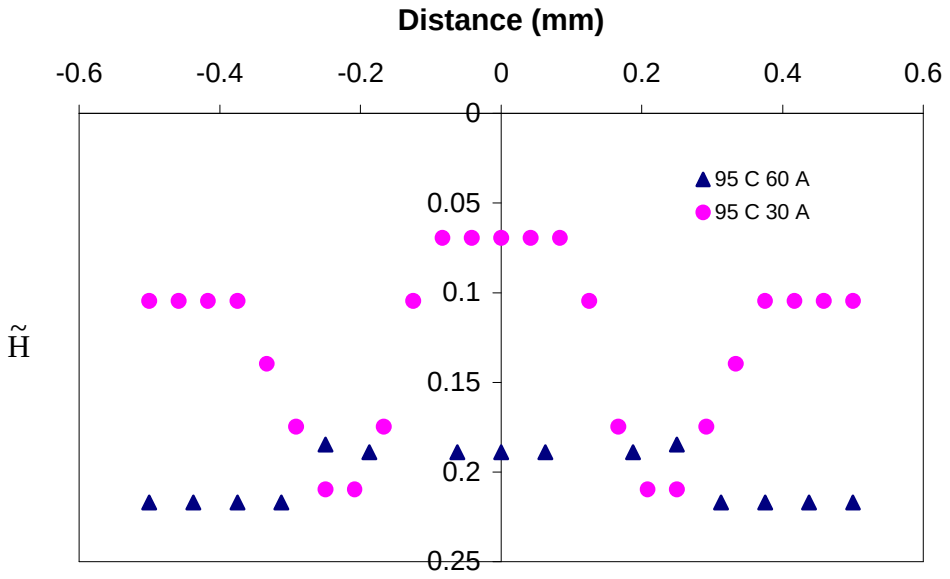

Figure 110: Normalized thickness distribution of ABS patterns embossed at embossing temperature 95° C, embossing force 400 N, and varied rubber shore hardness 30 A and 60 A.

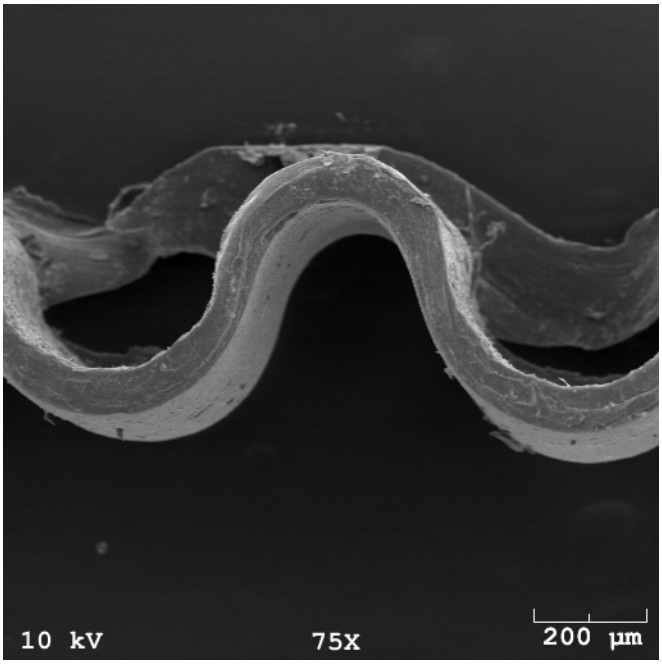

a)

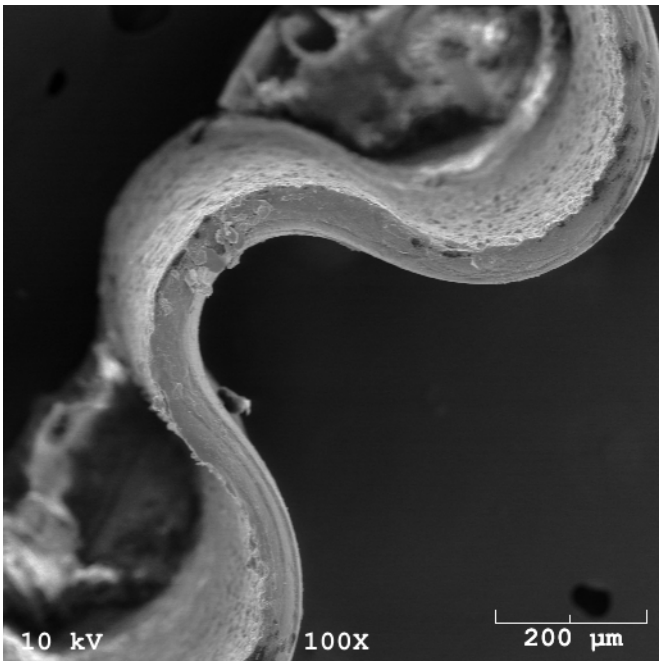

b)

Figure 111: Isothermally embossed ABS film at 95°C, 60A rubber shore hardness and with varied embossing force: a) 200 N and b) 400 N.

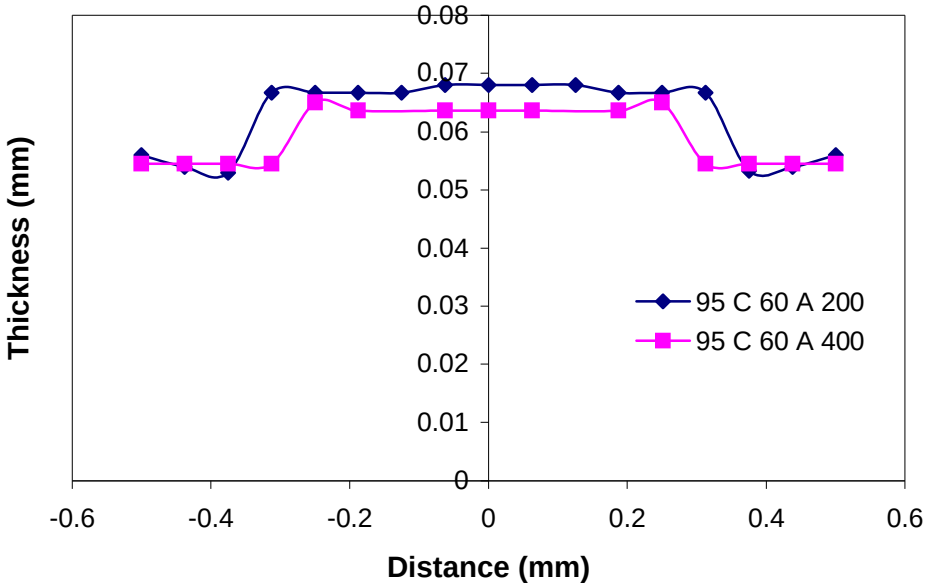

Figure 112: Thickness distribution of isothermally embossed ABS film at 95°C, 60A rubber shore hardness and varying embossing loads.

CHAPTER 8

MODELING OF RUBBER-ASSISTED EMBOSSING

8.1 Introduction

In thermoplastic forming the quality of the final product is greatly dependent on the material flow and the resulting thickness distribution. The traditional "trial and error" methods for optimizing these manufacturing processes, as widely used today, are quite time consuming and expensive. Hence, the interest in the use of numerical simulations as a powerful tool for process optimization has been rapidly growing in the polymer processing industry.

The polymer film during rubber-assisted embossing undergoes initial bending followed by stretching along the length of the micro-grooves. The deformation behavior is quite similar to that in thermoforming. In thermoforming modeling and simulation, it is common to use viscoelastic and hyperelastic rheological models. In particular, hyperelastic models have demonstrated their suitability for modeling materials which are isotropic, incompressible and capable of undergoing large stretch ratios under the conditions of relatively high strain rate and large deformations [64]. The ABS film during rubber-assisted embossing of the microgrooves, as described in Chapter 7, was subjected to stretch ratios of almost 2 and a total strain of 57% at a respentive strain rate of 2 s^{-1}. This suggests that the hyperelastic material model may be appropriate to describe the film deformation in rubber-assisted embossing. Considerable amount of research, mostly based on the strain energy function [65-71], has been carried out to apply both numerical and analytical techniques for simulating thermoforming processes. The predicted material response from hyperelastic models agreed with the actual material behavior in thermoforming characterized by high nonlinearity associated with large strains and large

deformation rates, and these models were able to predict the thickness distribution in thermoforming [64].

In this study, the polymer deformation during rubber-assisted embossing was modeled using Mooney-Rivlin hyperelastic model. The finite element method was used to solve the related equations. Accurate characterization of the deformation properties of the polymer film is particularly important for the embossing simulation. The necessary material parameters in the Mooneyh-Rivlin model were determined by data fitting of the actual tensile testing data obtained at a testing temperature equal to the embossing temperature.

8.1 Material Characterization

Tensile tests were carried out on ABS samples of 50×11× 0.125 mm at a strain rate of 2 s^{-1} and different embossing temperatures of 95, 105, 110 and 115 °C. The stress-strain curves of ABS are shown in Fig113. Fig.114 shows the stress-strain curves for rubber pads with 30A and 60A shore hardness at a temperature of 25°C and an engineering strain rate of 3 s^{-1}. The stress-stretch ratio curves are given in Fig.115 and Fig.116.

8.2 Modeling of Rubber-Assisted Embossing

Hyperelastic models and their derivations have been extensively discussed in literature [65-73]. Hyperelastic models demonstrate the materials strain levels that exceed the simple Hookean spring condition where the stress is proportional to strain and the proportionality constant is the Young's modulus [67]. In these model, it is hypothesized that the work done by the stresses during a deformation process is dependent solely on the initial state at time t_0 and the final configuration at time t, and the behavior of the material is path independent. Materials obeying such a model are called hypoelastic materials. The deformation behavior of hyperelastic materials is defined by the existence

of a scalar functions, W(F), called strain energy function or strain energy potential, from which stresses can be derived at each strain point.

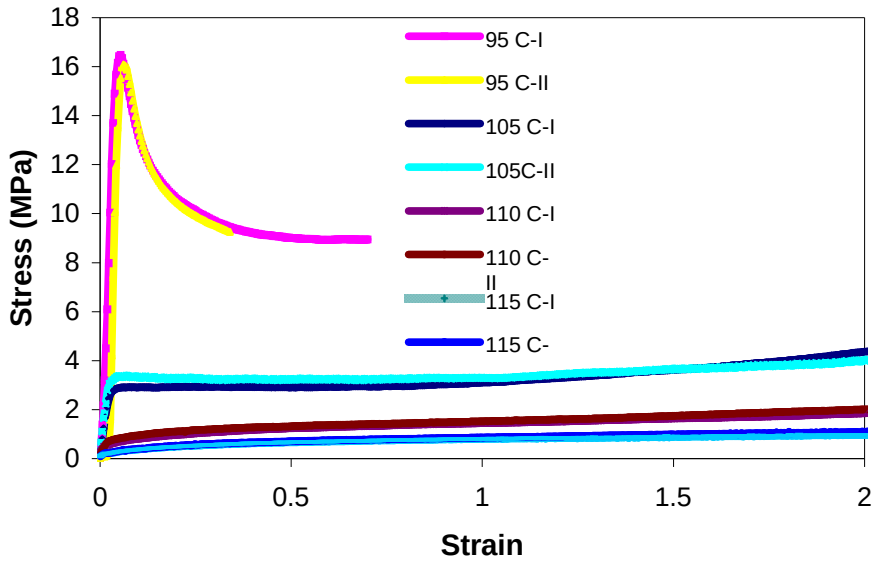

Figure 113: Tensile stress versus tensile strain curves of ABS at different temperatures.

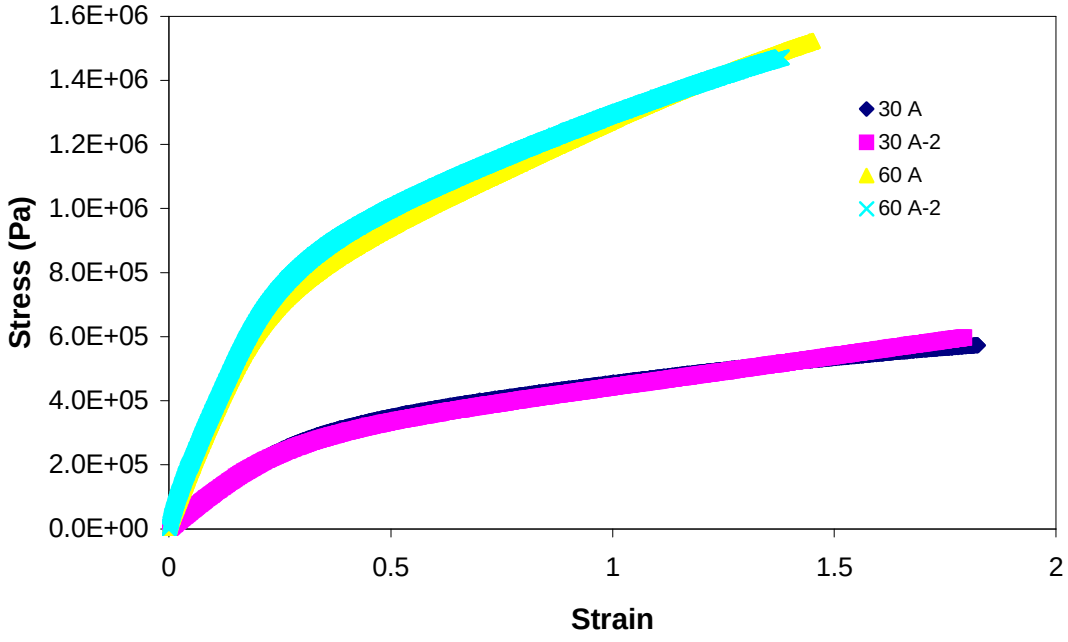

Figure 114: Tensile stress versus tensile strain curves of 30A and 60 A shore hardness

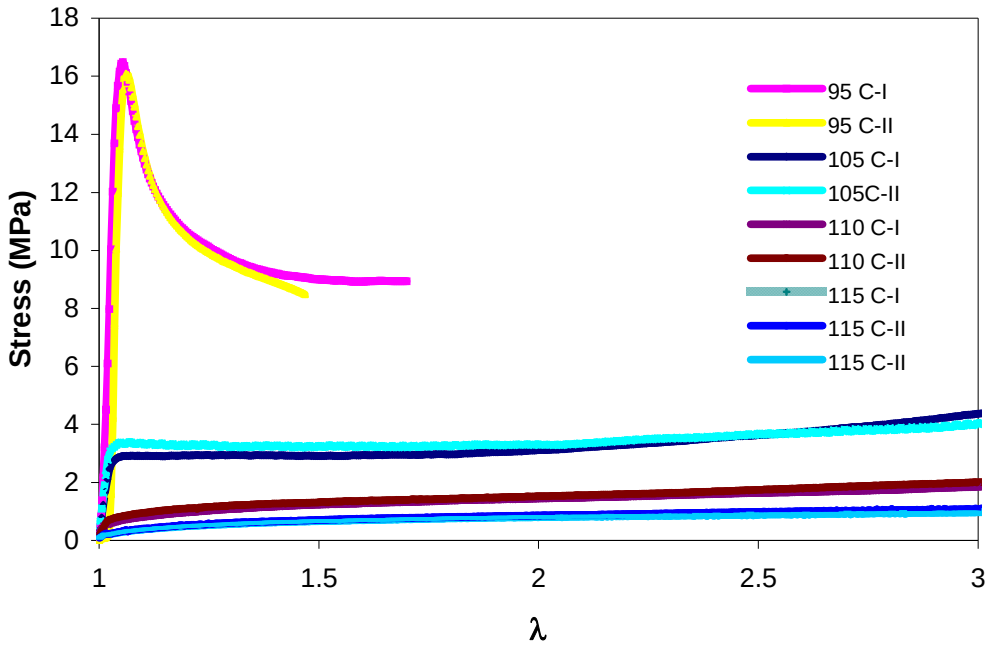

Figure 115: Tensile stress versus stretch ratio curves of ABS at different temperatures. rubber pads.

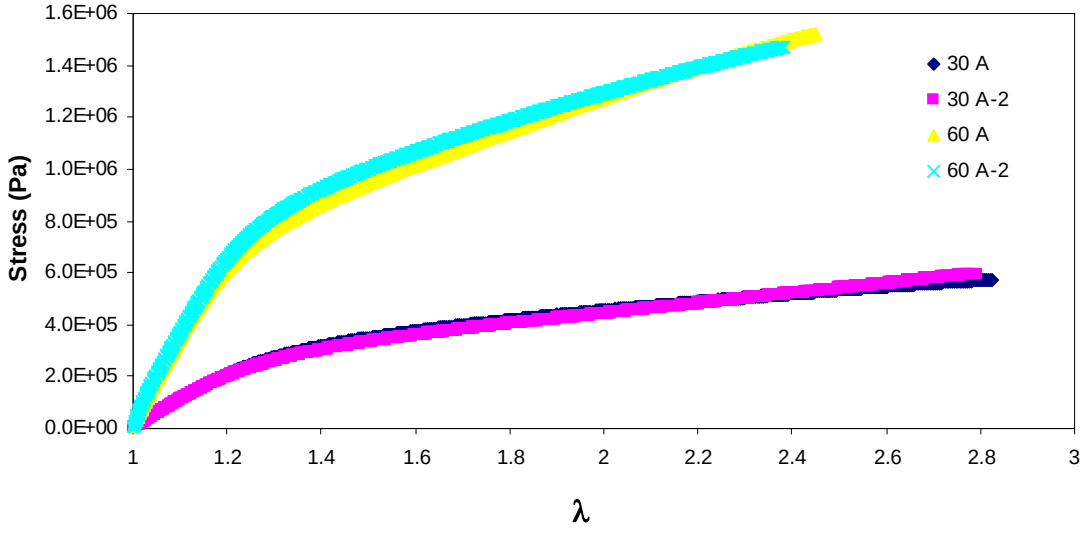

Figure 116: Tensile stress versus stretch ratio curves of rubber pads.

The strain energy function must be independent of frame of reference and hence written as a function of Cauchy-Green deformation tensor, C_{ij}. The stress tensor is given by

$$S_{ij} = \frac{\partial W}{\partial E_{ij}} = 2\frac{\partial W}{\partial C_{ij}} \tag{34}$$

where S_{ij} is the Piola-Kirchhoff stress tensor, W is the strain energy function per unit undeformed volume, E_{ij} is the Langrangian strain tensor and C_{ij} is the Cauchy-Green deformation tensor.

The Langrangian strain tensor may be expressed as

$$E_{ij} = \frac{1}{2}\left[(F_{ik} F_{kj}) - \delta_{ij} \right] \tag{35}$$

where F_{ij} and F_{kj} are the deformation gradients and δ_{ij} is the Kronecker delta. Considering a point A on the film shown in Fig.117, its position is denoted by P_i. After deformation, point B denotes the new position represented by $p_i = P_i + d_i$, where d_i is the displacement of the point in the i^{th} direction. The principal stretch ratios of C_{ij} are λ_1^2, λ_2^2, and λ_3^2, and exist only if

$$\det\left[C_{ij} - \lambda_p{}^2 \delta_{ij} \right] = 0 . \tag{36}$$

Solving Eq.3, we obtain,

$$\lambda_p{}^6 - I_1 \lambda_p{}^4 + I_2 \lambda_p{}^2 - I_3 = 0 \tag{37}$$

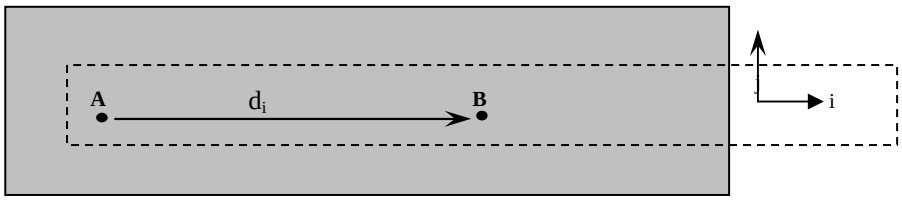

Figure 117: Film deformation

where I_1, I_2 and I_3 are Cauchy-Green strain invariants which can be expressed in terms of principal stretch ratios as follows:

$$I_1 = \lambda_1^{\,2} + \lambda_2^{\,2} + \lambda_3^{\,2}$$
$$I_2 = \lambda_1^{\,2}\lambda_2^{\,2} + \lambda_2^{\,2}\lambda_3^{\,2} + \lambda_1^{\,2}\lambda_3^{\,2} \quad (38)$$
$$I_3 = \lambda_1^{\,2}\lambda_2^{\,2}\lambda_3^{\,2} = [\det(F_{ij})]^2$$

where F_{ij} is the Piola-Kirchhoff stress tensor and $[\det(F_{ij})]^2 = J^2$. J is the ratio of the deformed elastic volume over the undeformed volume of the materials.

Rivlin and Saunders [74] constructed an empirical strain energy function given by

$$W = C_{10}(I_1 - 3) + f(I_2 - 3), \quad (39)$$

where $f(I_2\text{-}3)$ was determined from experiments. Here I_1 and I_2 are the strain invariants from Eq.5. If $f(I_2\text{-}3)$ could be assumed proportional to $(I_2\text{-}3)$, as indicated by experimental observations of direct proportionality of shear stress to the shear angle in simple shear [73], the Riviln and Saunders' strain energy function can be simplified as a Mooney function [74]

$$W = C_{10}(I_1 - 3) + C_{01}(I_2 - 3) \quad (40)$$

The equation is refererd to as the Mooney-Strain energy function or the Mooney Rivlin model. The two-parameter Mooney-Rivlin strain energy can be described as a function of the three Cauchy strain invariants as follows [74],

$$W = C_{10}(I_1 - 3) + C_{01}(I_2 - 3) + (1/d)(J - 1)^2. \quad (41)$$

Mooney-Rivlin strain energy potentials with three, five and nine parameters can be written as:

Three parameter Mooney-Rivlin equation,

$$W = C_{10}(I_1 - 3) + C_{01}(I_2 - 3) + C_{11}(I_1 - 3)(I_2 - 3) + (1/d)(J - 1)^2 \quad (42)$$

Five parameter Mooney-Rivlin equation,

$$W = C_{10}(I_1 - 3) + C_{01}(I_2 - 3) + C_{20}(I_1 - 3)^2 + C_{11}(I_1 - 3)(I_2 - 3) + C_{02}(I_1 - 3)^2 + (1/d)(J - 1)^2 \quad (43)$$

Nine parameter Mooney-Rivlin equation,

$$W = C_{10}(I_1 - 3) + C_{01}(I_2 - 3) + C_{20}(I_1 - 3)^2 + C_{11}(I_1 - 3)(I_2 - 3) + C_{02}(I_2 - 3)^2 + C_{30}(I_2 - 3)^3 + C_{21}(I_1 - 3)^2(I_2 - 3) + C_{12}(I_1 - 3)(I_2 - 3)^2 + C_{03}(I_2 - 3)^3 + (1/d)(J - 1)^2 \quad (44)$$

where C_{10},C_{01},C_{20},C_{11},C_{02},C_{30},C_{21},C_{12},C_{03}, and d are material constants calculated by curve fitting the uniaxial stress-strain data. The rubbers with shore hardness 60A and 30A were fitted using the three-parameter Mooney-Rivlin model (given by Eq.42) as shown in Fig.118 and Fig.119. ABS deformation at 105°C is plotted using the five-parameter model (given by Eq.43), as shown in Fig.120.

The the microgroove length is much larger than the microgroove width, and hence the deformation is considered to be two-dimensional. Considering the periodicity and symmetry of the geometry, only a half of a microgroove was used in the geometrical model, as shown in Fig.121. The boundary conditions are: BS1 (contact mold surface), BS2 (free surface with contact detection with no slip boundary condition), BS3 (d_x and f_s, where d_x is the x-displacement and f_s is the shear force.), BS4 ($d_x = 0$ and $d_y = -d$, where d_x and d_y are the displacements along X and Y directions), and BS5 (symmetry).The Mooney-Rivlin model was solved with these boundary conditions using finite element codes.

Fig.122 shows the simulation results for ABS film embossed using 60 A Shore hardness using a constant embossing force and at varying temperatures of 95°C, 105°C and 115°C. The film thickness was found to decrease from the center towards the periphery with increase in temperatures. The best film uniformity was obtained at 95°C. Similar phenomenon was observed during the experiment. At temperatures close to Tg the embossed film possesses stiffness larger than the deforming rubber pad and sufficient plasctcity, resulting in a uniform film thickness.

Fig.123 and 124 show comparisons of the thickness distribution between the predicted results and the experimental results .It can be seen that there is considerably a

good fit between the two set of data. The average coefficient of variation between the predicted results and the experimental ones were 7% and 15% for 105°C and 115°C, respectively. However, a higher coefficient of variation was observed between the experimental and simulation resluts for films embossed at 95°C. This may be attributed to the relatively large fitting error at this temperature due to the high order characteristics of the stress-strain curve at this temperature. The data fitting at 95°C was carried out by excluding the strain hardening effect in the stress-strain curve to obtain a converged solution.

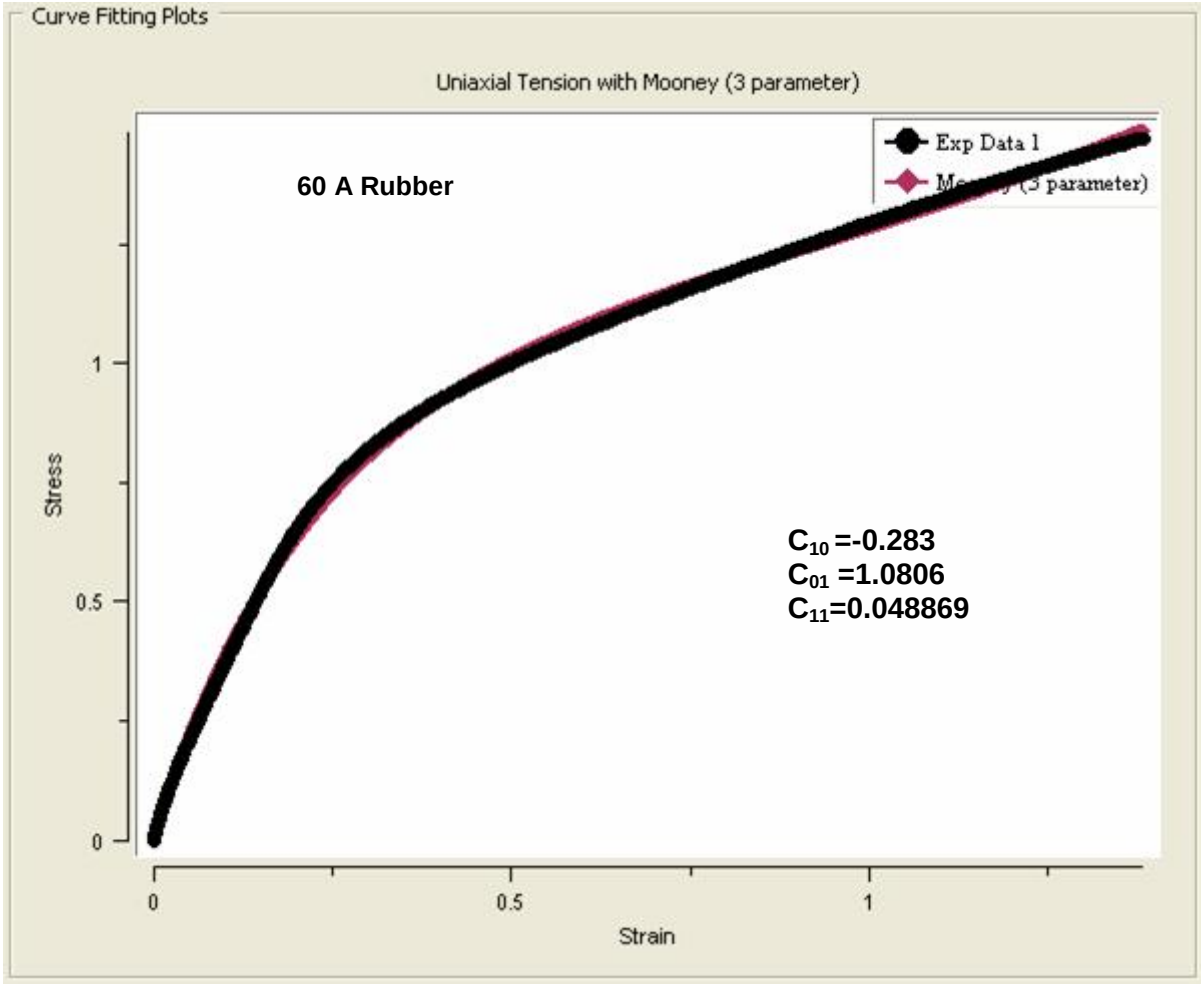

Figure 118: Curve fitting of the stress-strain data of 60 A rubber pads using the 3-parameter Mooney-Rivlin model.

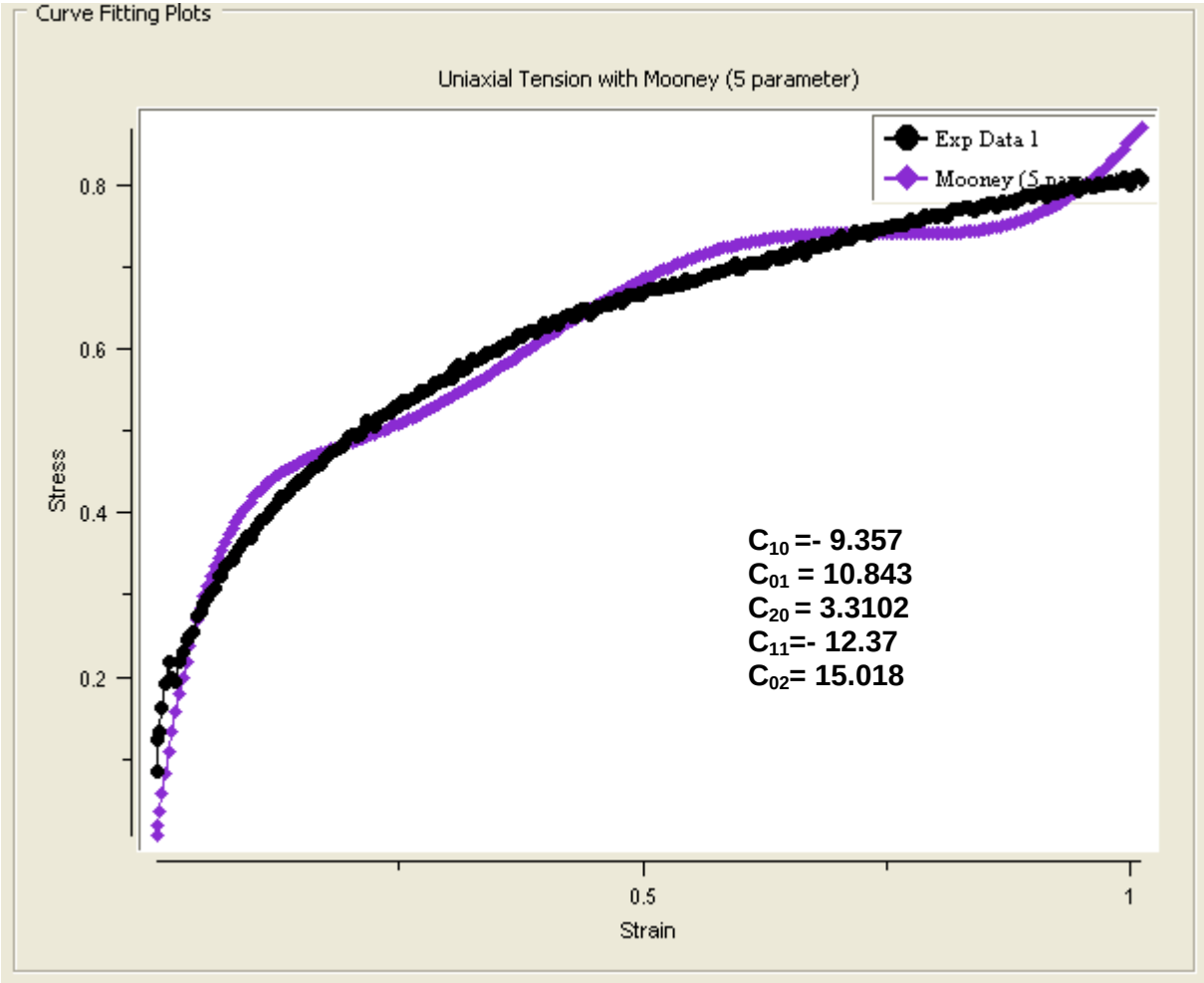

Figure 119: Curve fitting of the stress-strain data of ABS at 115°C using the 5-parameter Mooney-Rivlin model.

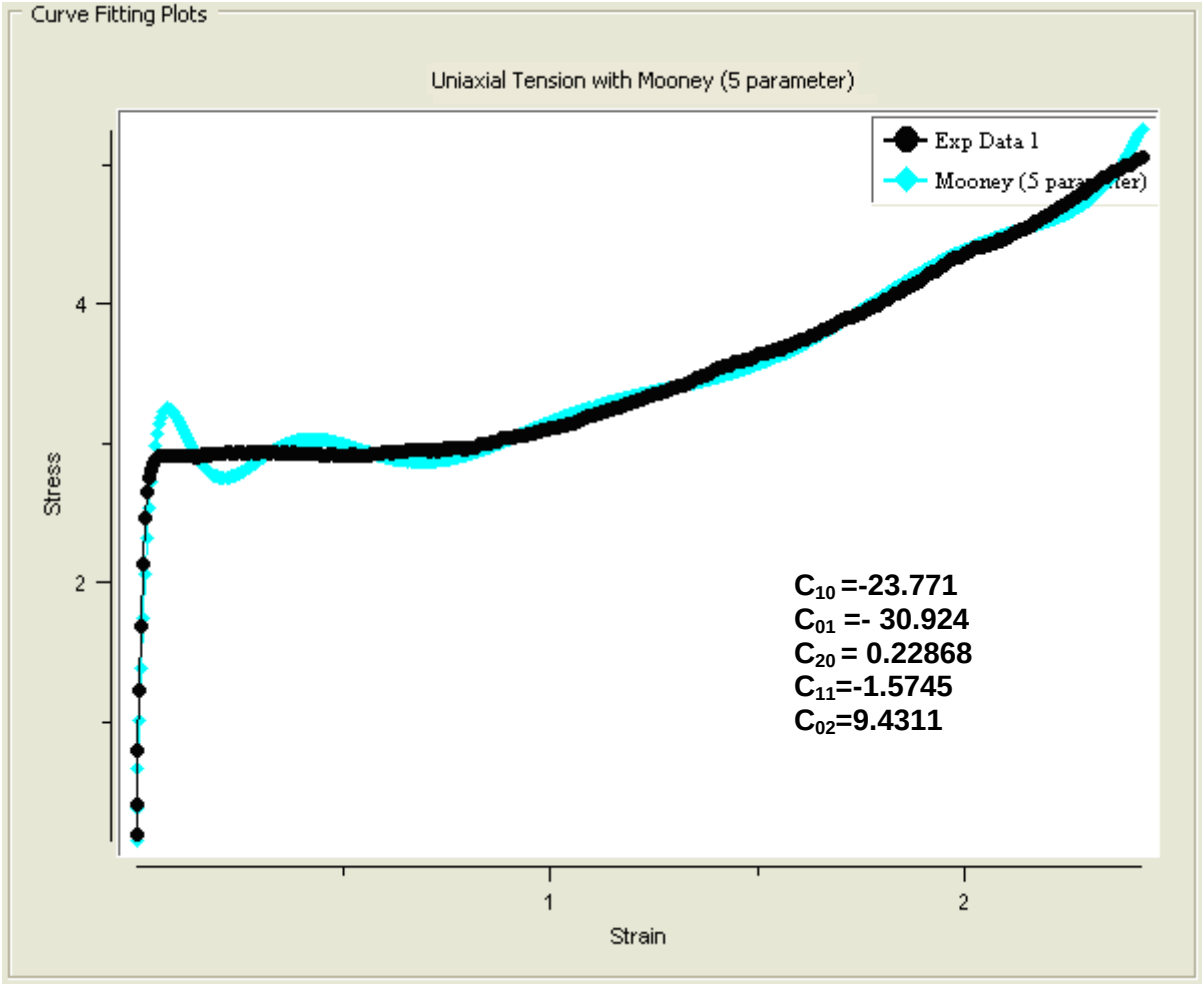

Figure 120: Curve fitting of the stress-strain data of ABS at 105°C using the 5-parameter Mooney-Rivlin model.

8.3 Modeling of Recovery of Embossed films

From the experimental results on rubber-assisted embossing, it can be seen that the deformed polymer must possess a higher stiffness and adequate plasticity to achieve uniform film thickness. In a typical embossing process the amorphous polymer is deformed at 40°C above its glass temperature. However, during rubber-assisted embossing the best pattern replication and uniformity in film thickness was obtained at 95°C. At such low temperatures, the elastic recovery of the film results in poor pattern replication in the absence of sufficient holding time.

The generalized Maxwell model with a combination of springs and a dash pots shown in Fig.125 was chosen as the constitutive model in predicting the instantaneous film recovery during embossing. This generalized linear viscoelastic model can be written as

$$\tau(t) = + \int_{-\alpha}^{t} M\,(t - t')\,\gamma\,(t, t')\,dt', \tag{45}$$

where τ is stress and M(t-t') is the memory function defined as $M(t-t') = \partial G(t-t')/\partial t'$ in which G(t-t') is the relaxation modulus. The memory function can be written using a discrete model,

$$M(t - t') = \sum_{k=1}^{\alpha} \frac{\eta_k}{\lambda^2{}_k} e^{-(t-t')/\lambda_k}, \tag{46}$$

where η_k, λ_k and γ are partial viscosity, relaxation time and strain, respectively. The memory function monotonically decreases to zero as (t-t') goes to infinity. The duration of the memory is governed by the longest relaxation time λ_{max}. DMA was used to measure relaxation times of ABS at 95°C for a constant strain of 1%. Fig. 126 shows the relaxation modulus decaying with time. The material data are listed in Table 3.In eq.45, t represents the holding time and t' represents the processing time. An analytical solution to Eq.45 was obtained for t = 5, 15 and 40 s, and $\gamma\,(t, t') = 0.57$.

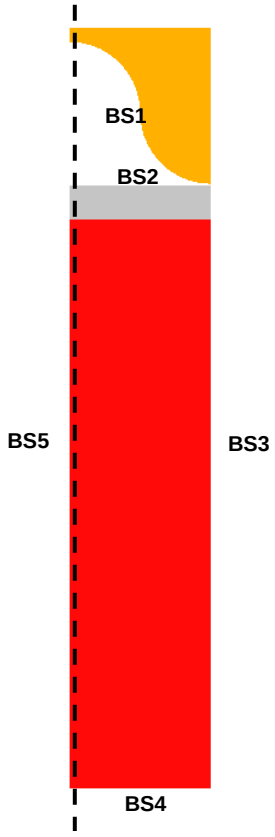

Figure 121: Geometry and boundary conditions used in the simulation model for rubber-assisted embossing. The boundary conditions are: BS1 (contact mold surface), BS2 (free surface with contact detection with no slip boundary condition), BS3 (d_x and f_s, where d_x is the x-displacement and f_s is the tangential force), BS4 ($d_x = 0$ and $d_y = -4.5$, where d_x and d_y are the displacements along X and Y directions), and BS5 (symmetry).

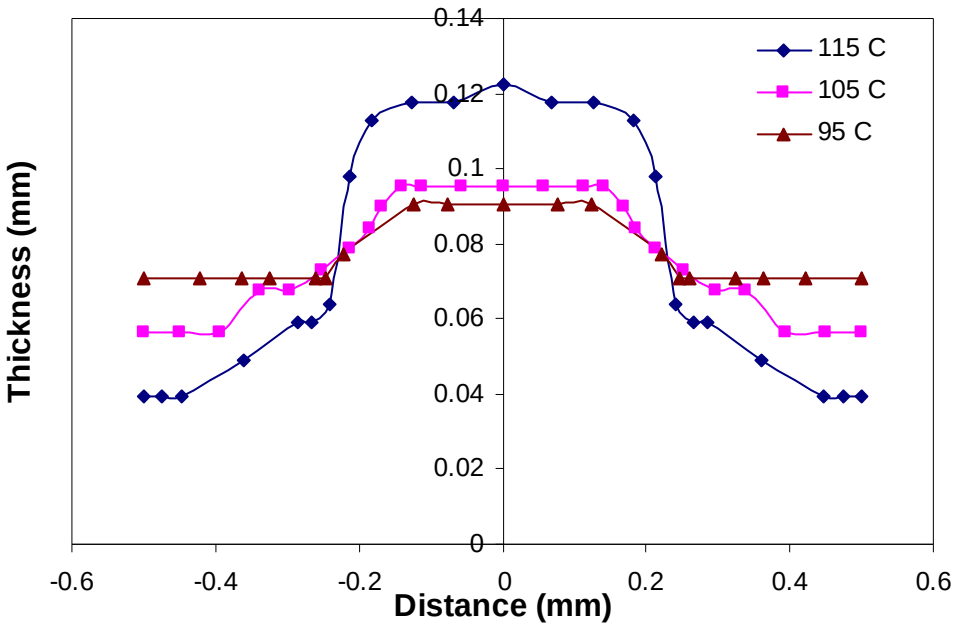

a)

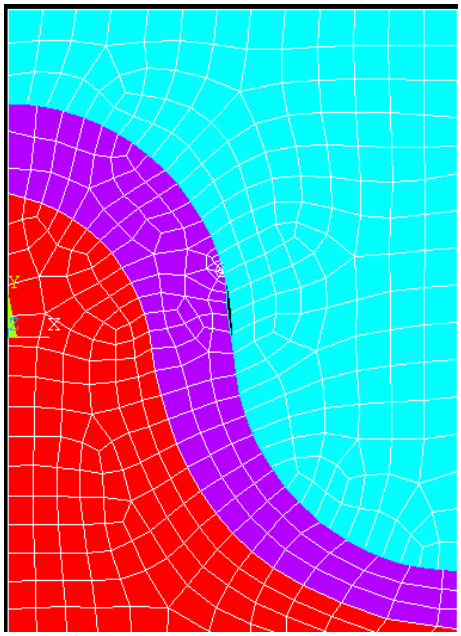

b)

Figure 122: a) Simulation results showing thickness distribution of rubber embossed films with 60A shore hardness at various temperatures and b) FEA result for 105°C.

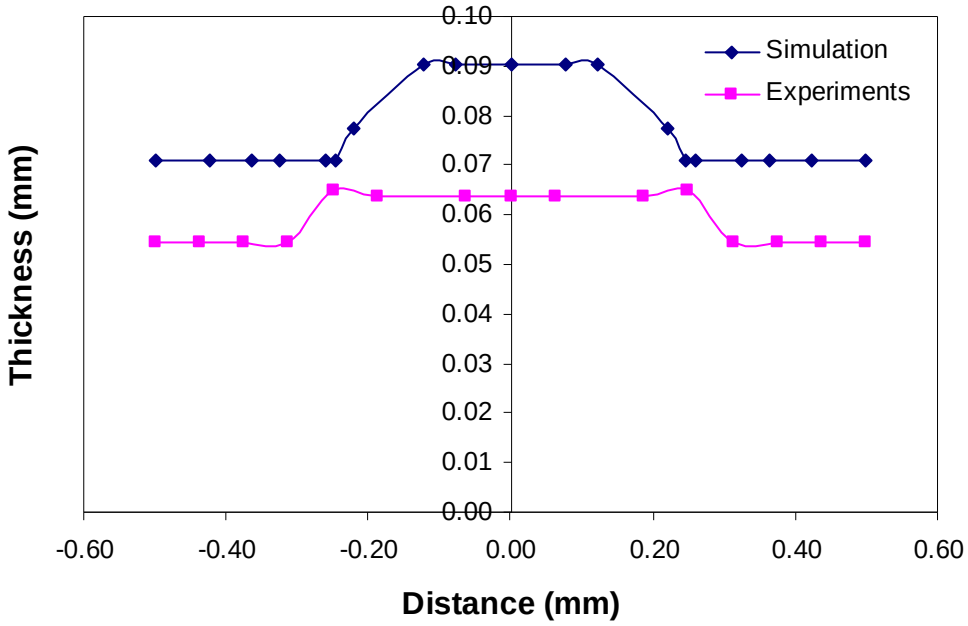

a)

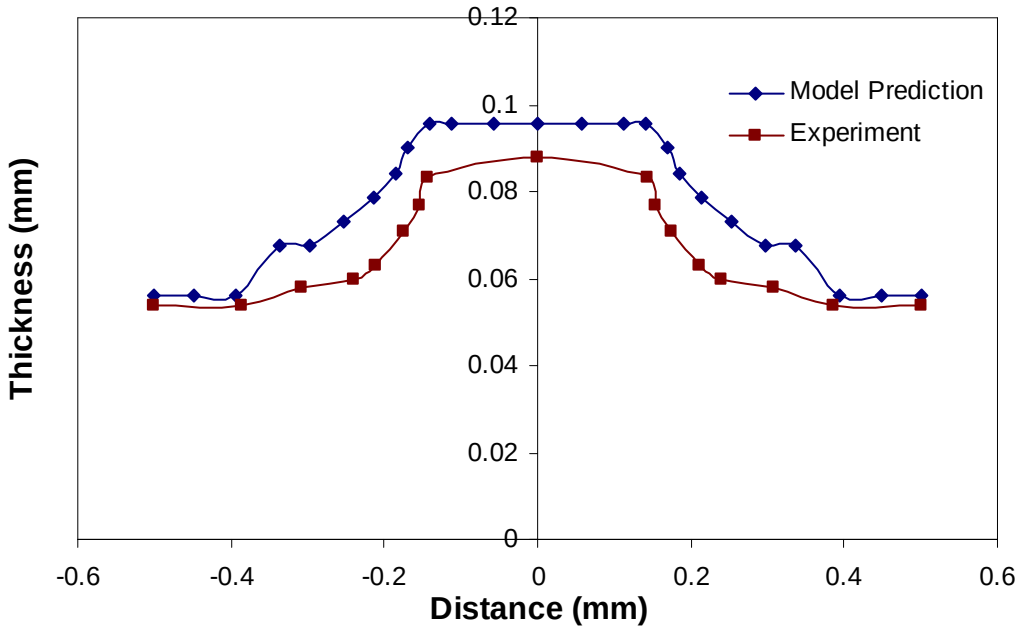

b)

Figure 123: Comparison of thickness distribution of rubber embossed films using 60 A shore hardness at a) 95°C and 105°C.

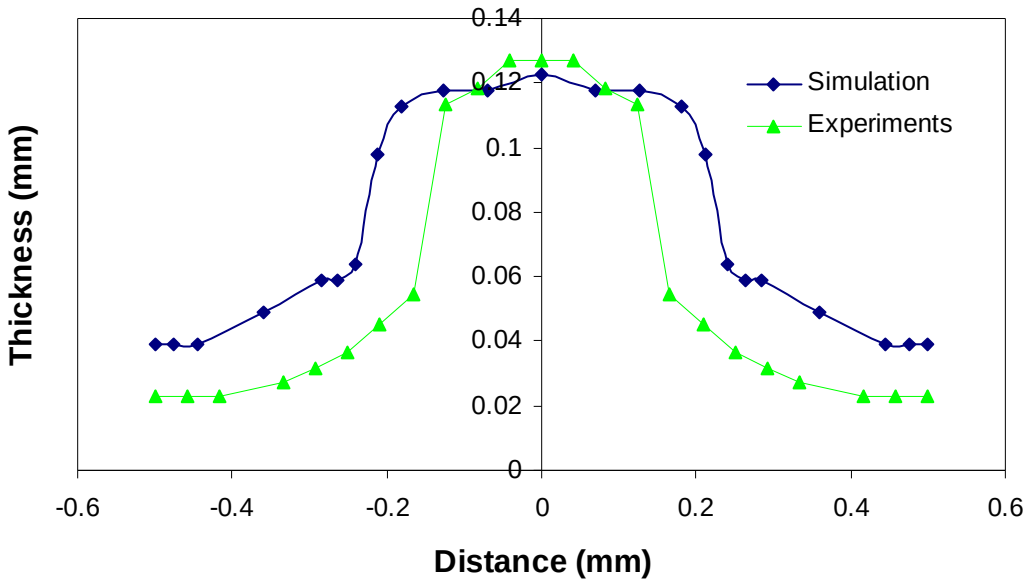

Figure 124: Comparison of thickness distribution of rubber embossed films using 60 A shore hardness at 115°C.

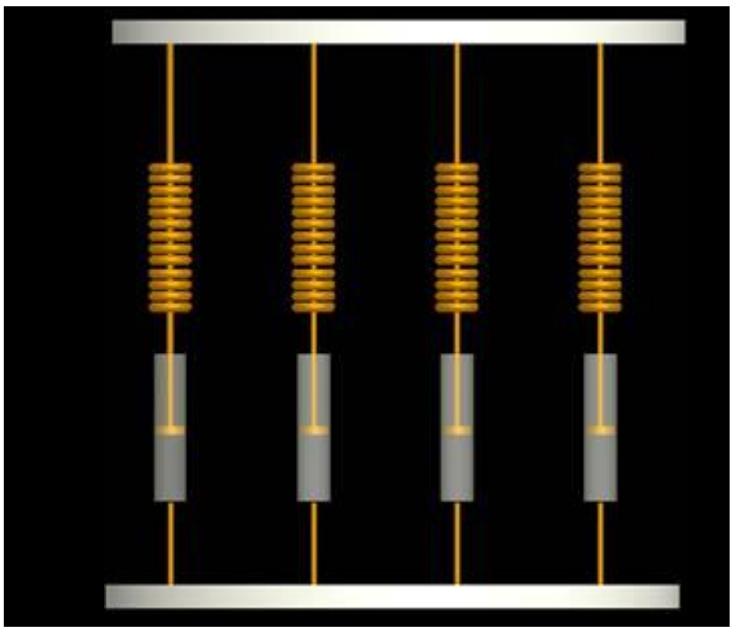

Figure 125: Generalized Maxwell model.

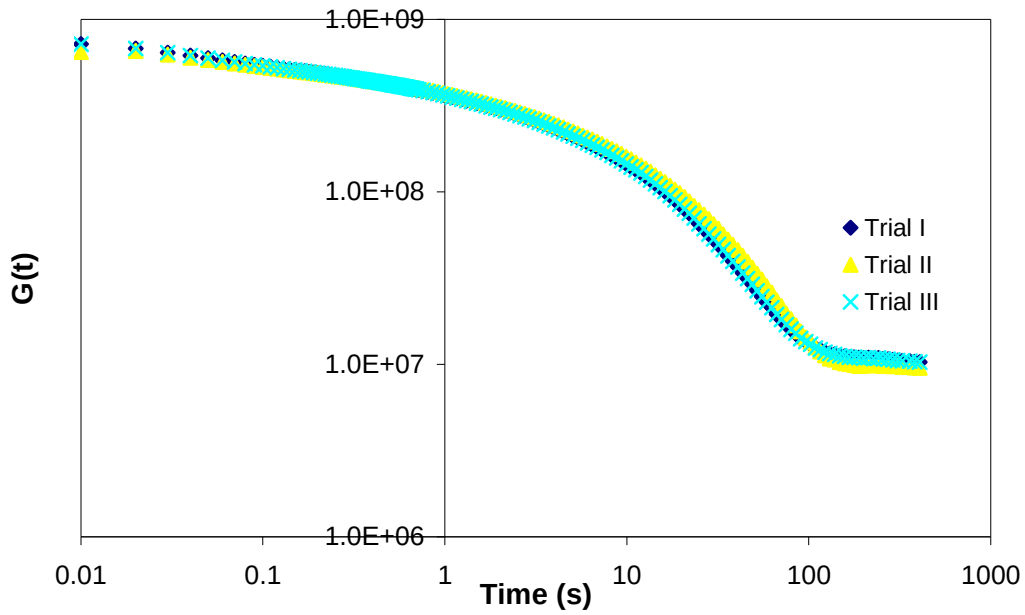

Figure 126: ABS stress relaxation test at 95°C.

The instantaneous strain at the end of the holding time is

$$\varepsilon(t) = \frac{\sigma(t)}{G'} \tag{47}$$

where σ(t) is the recovered stress and G' is the equivalent elastic modulus of the material which can be written as $G' = \sum_{i=1}^{k} G_k \frac{(\omega^2 \lambda^2_k)}{(1+\omega^2 \lambda^2_k)}$. G_k, λ_k and ω represent partial relation modulus, relaxation time, and frequency.

Table 3: Material data for modeling instantaneous film recovery.

K	**λ_K**	**G(t) N/mm^2**	**η_K**
1	0.01	7.33×10^1	7.33×10^{-1}
2	4.76	2.21×10^1	1.05×10^2
3	22	7.66	1.68×10^2
4	166	1.12	1.86×10^2

A series of recovery experiments were carried out to study the effect of holding time on the embossed film during the rubber-assisted embossing process. The ABS film and the mold were preheated to 95°C as discussed in Chapter 7. Various holding times of 5, 15 and 40 s were used during the embossing process. At the end of the holding stage the 400 N load was released and the embossed part was cooled by dropping it into water. Fig.127 shows the SEM images of the recovered films. Motic® Stereomicroscope was used to measure the curvature of the recovered film.

Comparison of results from analytical solutions and experiments are shown in Fig.128. Radius and coordinate shift models were used to plot the results from the analytical model. If R_1 and R_2 represent the radius of the embossed film, as shown in Fig.128, the geometry of the recovered film through the radius shift model was obtained as

$$\varepsilon = (R_1 - R'_1)/R_1 \text{ and } R'_1 = R_1 - \varepsilon R_1, \quad (48)$$

where R_1 and R'_1 are the radii of the perfectly replicated film and the recovered film, and ε represents the instantaneously recovered strain. The geometry of the recovered film using the coordinate shift method was graphed by shifting each point on the circumference of the perfectly replicated film by the equivalent recovered strain. The film recovery after embossing occurs along sections R_1 and R_2. It cane be seen from Fig.128 that the coordinate shift model predicts the recovery of the film better than the radius shift model, with a reasonable values of error of 3%. For holding times higher than 40 seconds no considerable recovery was found through experiment and simulation results. This agrees well with the results from the stress relaxation tests. It can be seen from Fig.126 that, it takes 22 s for 90% of the stress to relax at 1% strain. Thus, above 40 s the deformed polymer should almost be free from residual stresses.

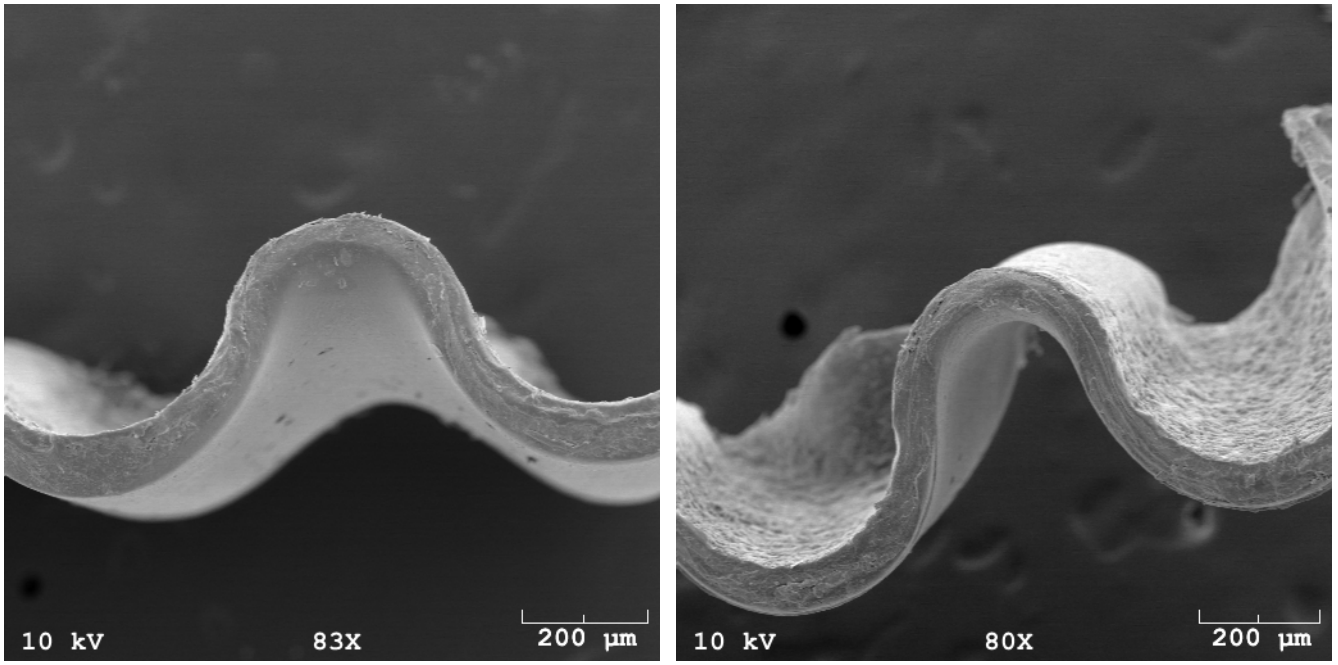

a) b)

Figure 127: SEM image of ABS film embossed with holding time: a) 5 s and b) 40 s.

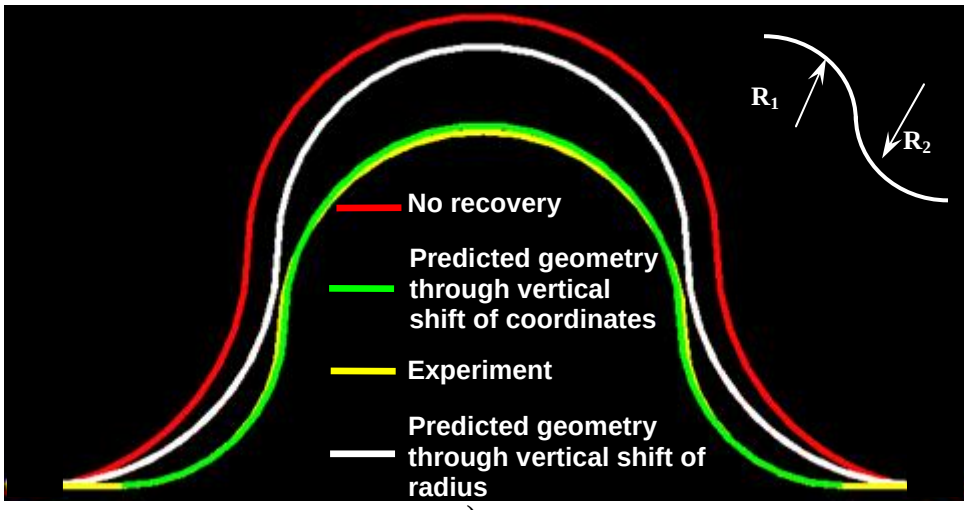

a)

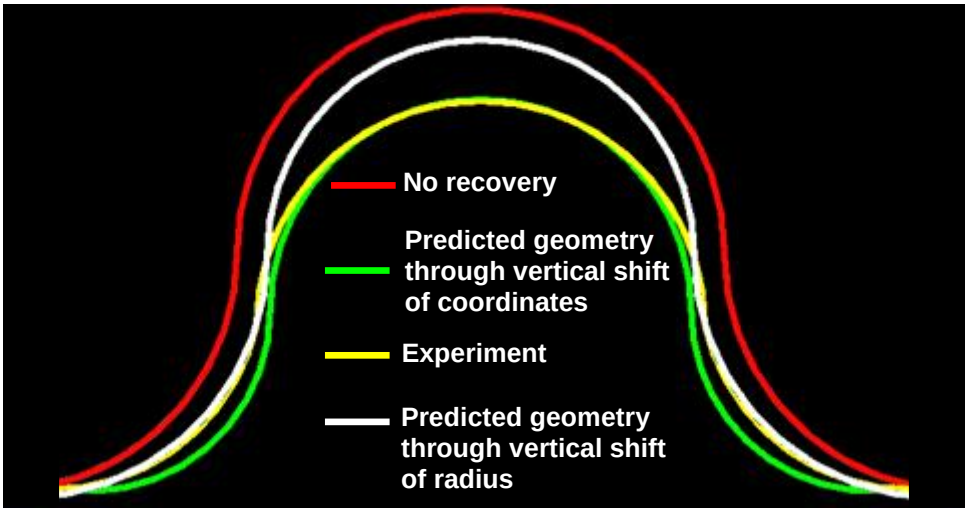

b)

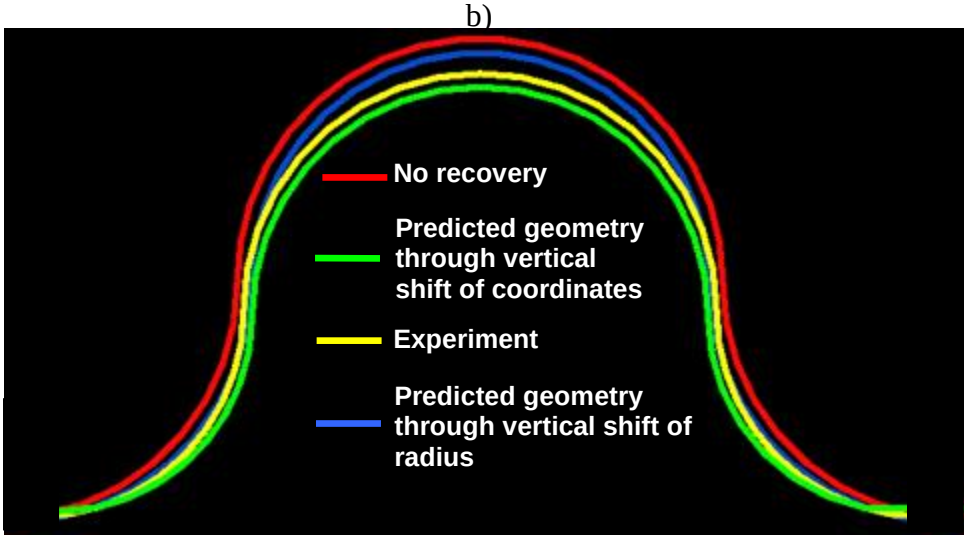

c)

Figure 128: Experimental and predicted shapes of ABS films embossed at 95°C with varying dwell time of a) 5 s, b) 15 s and c) 40 s.

CHAPTER 9

CONCLUSIONS AND RECOMMENDATIONS

This Ph.d. Dissertation research addressed three major limitations of the hot embossing process, namely, long cycle time, difficulty in producing shell patterns, and difficulty in building up a high embossing pressure on thick substrates. To overcome these limitations, three new technical approaches – two-station embossing, rubber-assisted embossing, and through thickness embossing – were developed and investigated.

9.1 Conclusions

a) Two-station embossing

- Microchannels and microlenses embossed on HDPE and ABS, respectively, with an embossing time of 3 s and a total cycle time as short as 10 s, displayed excellent replication fidelity including local replication of sharp edges and mold surface defects.
- Thin aluminum shells, 1.4 mm in thickness, was rapidly heated from room temperature to 200°C in about 3 s using a hot station at 250°C. The same shell was subsequently cooled to 50°C in 5 s.
- For a short embossing time of 3 s or less, uniform and controllable flow pattern was achieved in two-station embossing of microcavities with a characteristic feature size on the order of 100 μm, even with the polymer not preheated.

b) Through-thickness embossing

- A discrete four-channel polymer waveguide was fabricated using a single-step through-thickness embossing process.

- With ABS as an embossing polymer, waveguides with sharp edges were completely filled at an embossing temperature of 140°C and a total cycle time of 7 minutes. At embossing temperatures significantly lower or higher than 140°C, incomplete mold fill was observed.
- Under an isothermal embossing condition, significant outflow was observed, resulting in incomplete cavity fill. In contrast, complete cavity fill was achieved when a substantial temperature difference between the polymer and the mold was used.

c) Rubber-assisted embossing

- Microgroove patterns with characteristic dimensions on the order of 100 μm or above were successfully patterned onto thin polymer films.
- The major process parameters affecting the patterning quality in rubber-assisted embossing were found to be embossing temperature, embossing pressure, and rubber hardness.

9.2 Recommendations

a) Two-station embossing

- By employing a shell mold and two separate stations (one hot and one cold) for heating and cooling, mold rapid heating and cooling can be achieved while a very low thermal load is applied to the mold.

b) Through-thickness embossing

- Discrete 3-D parts can be fabricated in a single-step through-thickness embossing process.
- For complete pattern replication, a substantial temperature difference is required between the embossed polymer and the mold.

c) Rubber-assisted embossing

- A polymer film with a stiffness higher than that of the rubber counter tool and a long isothermal dwell time are desired in rubber-assisted embossing to improve the patterning quality (i.e., replicability and pattern uniformity). An appropriate process window to ensure a stiff polymer film and yet a reasonably short relaxation time is needed.

The studies conducted in this dissertation work were mainly focused on several specific types of microstructures or microparts; however, with the fundamental understanding obtained from the systematic experimental and theoretical investigations as described in the previous chapters, the above findings may be generalized to other applications in the emerging biomedical, microelectronics, and telecommunication industries. With reduced cycle time and enhanced replicability for shell patterns and discrete parts, the findings from this research would lead to an integrated, more capable polymer embossing module where difficult-to-emboss polymer microstructures and microparts can be fabricated in a cost-effective manner.

REFERENCES

1. Rotting, O., Ropke, W., Becker, H., and Gartner, C., Micro. Tech. 8, 32 (2002)

2. Gates, B.D., Xu, Q., Stewart, M., Ryan, D., Willson, C.G. and Whitesides, G.M., Chem. Rev., 105, 1171 (2005).

3. Becker, H., and Locascio, L.E., Talanta 56, 287 (2002).

4. Becker, H., and Gartner, C., Electrophoresis. 21, 12 (2000).

5. Heckele, M., and Schomburg, W.K., J. Micro. Micro. 14, 1 (2004).

6. Lee, H., Hong, S., Yang, K. and Choi, K., Microelec. Eng. 83, 323 (2006).

7. Dreuth, H., and Heiden, C., Sens. & Actua. 78, 198 (1999).

8. Louis P.R., U.S. Patent 4259286 (1979).

9. Koger, T.H., U.S. Patent 4552709 (1985).

10. Hanstein, F., and Muench, T.P. U.S. Patent 4038360 (1977).

11. Truckenmüller, R., IEE. Proce. 151, 163 (2004).

12. Chang, J.H., and Yang, S.Y., Micro. Tech., 10, 76 (2003).

13. Chang, J.H., and Yang, S.Y., Micro. Tech., 11, 396 (2005).

14. Chang J.H., and Yang, S.Y., ANTEC., 1, 942 (2004).

15. Lee, H.S., Lee, S.K., Kwon, T.H. , Lee , S.S., IEEE/LEOS. Intern. Confer. Opti. MEMS, 135 (2002).

16. Chen, S.C., Peng, H. S., Chang, J. A., and Jong, W. R., Com. Heat. Mass. Trans. 31, 971 (2003).

17. Chen, S.C., Peng, H. S.,Chang, J. A., and Jong, W. R., J. of. Micromech. Microeng. 16, 1783 (2006).

18. Chen, C.H., Liu, C-P, Lee, Y.C., Hsiao, F.B., Chiu, M.H., Chung and Chiang, M.-H., J. Micromech. Microeng. 16, 1463 (2006).

19. Seunarine , K., Gadegaard, N., Riehle, M.O., and Wilkinson, C.D.W., Microelec. Eng. 83, 859 (2006).

20. Yao, D., Kimerling, T. E., and Kim, B., Polym. Eng. Sci, 12,730 (2006).

21. Yao, D., and Kim, B., Poly. Eng. Sci. 42, 2471 (2002).

22. Yao, D., and Nagarajan, P., Poly. Eng. Sci. 44, 1998 (2004).

23. Chien, H., L., and Chen, R., J.of Microlith. Microfab. Microsys 5, 0011031 (2006).

24. Grewell, D., Mokhtarzadeh, A., Benatar, A., Lu, C., and Lee, L., ANTEC. 49, 1094 (2003).

25. Jarrett, J.D., Hong, Y.L., and Isabel, R., Nanotechnology 17, 1975 (2006).

26. Heckele, M., and Durand, A., Euspen's. Inter. Conference., 196 (2001).

27. Michael, W., Diploma Thesis, Technical University of Denmark (2005).

28. Heckele, M., and Schomburg, W.K., J. Micromech. Microeng. 14, 1 (2004).

29. Truckenmuller, R., Rummler, Z., Schaller, T., and Schomburg, W.K. J. Micromech. Microeng. 12, 375 (2002).

30. Juang, Y.J., Lee, L.J., and Koelling, K.W., Poly. Eng. Sci. 42, 551 (2002).

31. Young , W.B., Micro-electr. Eng. 77, 405 (2005).

32. Eriksson, T., and Ramussen, H.K., J. Non-Newt. Fluid. Mech. 125,191 (2005).

33. Yao, D., Virupaksha, V.L., and Kim, B., Poly. Eng. Sci., 652 (2005).

34. Lee, J., Virkler, L., T. and Scott, C.,E., Poly Eng Sci 41, 2 (2001)

35. Nied, H., F., and Lorenzi, H.,G. , Hanser Verlag, Munich (1991)

36. Nied, H., F., and Taylor, C., A., Poly. Eng. Sci. 30, 1314 (1990)

37. Lappin, J., F., Harkin-Jones, M.,A., and Martin, P.,J.,ANTEC 45, 826 (1991)

38. Erchiqui, F., Gakwaya, A., Rachik, M., Poly. Eng. Sci. 45 125 (2005)

39. McEvoy, J.P., Armstrong, C.G., Crawford, R., J.,Advan in Poly. Tech. 17, 339 (1998)

40. Nam G.J., Ahn, K.H., Lee, J.W, Poly. Eng. Sci. 40, 2232 (2000)

41. Marckmann, G., Verron, E., Peseux, B., Poly. Eng. Sci 41, 426 (2001)

42. Bourgin, P., Cormeau, I., Saint-Matin, J. Mat. Proc. Tech. 54, 1(1995)

43. Song, Y.H., Zhang, K.F., Wang, Z.R., Diao, F.X., J. Mat. Proc. Tech. 97, 35 (2000)

44. Schmidt, F.M., Agassant, J.F., Bellet, M., Desoutter, L, J. Non-Newt. Fluid. Mech. 64 , 19 (1996)

45. Wiesche, S, Appl. Ther. Eng. 24, 2391 (2004)

46. Gao, D.M., Nguyen, K.T., Hetu, J.F., Laroche D., Garcia-Rejon, A, Advan. Perfor. Mat. 5, 43 (1998).

47. Jansen, K. M. B., and Flaman, A. A. M., Polym. Eng. Sci. 34, 894 (1994)

48. Kim, B. H., and Suh, N. P., Polym. Plast. Technol. Eng. 25, .73 (1986).

49. Becker, H. and Locascio, L. E., Talanta 56, 267 (2002).

50. Yu, J.C., Chen, X.X., Hung, T.R., Thibault, F., J. Intell. Manuf. 15 625 (2004)

51. Jin, T., Sun, J., Chen, D., and Zhang, S., Soil Tillage Res. 80 (2005).

52. Carlslaw H. S., and Jaeger, J. C., 1988, Clarendon Press, Oxford.

53. Jansen, K. M. B, Int. J. Heat Mass Transfer. 38, 309 (1995).

54. Yao, D., and Kim, B., Polym. Eng. Sci. 42, 2471 (2002).

55. Mills, A. F., Richard D. Irwin, Inc., 67(1992).

56. Stelson, K. A., Proc. Instn. Mech. Engrs. 217, 709 (2003).

57. Yao, D., and Kim, B., ASME J. Manufacturing Science Engineering, 126, 733 (2004).

58. Bendada, A., Derdouri,A., Lamontagne, M., and Simard.,Y., Appl. Ther. Eng. 24, 2029 (2004).

59. Sridhar, L. and Narh, K.A., Simulation, 73, 144 (1999).

60. Yu, C.J., Sunderland, J.E. and Poli, C., Poly. Eng. Sci. 30, 1599 (1990).

61. Delaunay, D., Le Bot, P., Fulchiron, R., Luye, J.F., and Regnier, G., Poly. Eng. Sci. 40, 1682 (2000).

62. Yao, D. and Kim, B., J. Inj. Mold. Tech. 6, 11 (2002).

63. Dong, Y., Lin, R. and Bhattacharaya, D., J. Mat Sci 40, 399 (2005).

64. Delorenzi, H. and Nied, H., Hanser, 117 (1991).

65. Williams, J., J. Strain Anal 5, 49 (1970).

66. Vlachopoulos, J., and Mirza, F., Elsevier Science, 75 (1997).

67. Marckmann, G., Verron, E., and Peseux, B., Polym Eng Sci 41, 426 (2001).

68. Bourgin, P., Cormeau, I., and Saint-Martin, T., J. Mat Proc Tech 54, 1 (1995).

69. Schmid, L., and Carley, J., Polym. Eng. Sci 15, 51 (1975).

70. Idem, J., Eng Sci Int 13, 563 (1975).

71. Bonet, J., and Wood, R., Cambridge University press, 118 (1997).

72. Carlone, P., and Palazzo, G., S., 794 (2006).

73. Rivlin, R., S., and Saunders, D., W. 243, 251 (1951).

74. Mooney, M., 11, 582 (1940).